MICROSCALE MODELING OF DEFORMATION RESPONSE OF ADVANCED HIGH STRENGTH STEELS AND MECHANICAL BEHAVIOR OF ACTIVE BIOPOLYMER NETWORKS

BY

PENG CHEN

B.E., XI'AN JIAOTONG UNIVERSITY, 2004

M.E. IN SOLID MECHANICS, XI'AN JIAOTONG UNIVERSITY, 2007

M.S. IN APPLIED MATHEMATICS, BROWN UNIVERSITY, 2011

A DISSERTATION SUBMITTED IN PARTIAL FULFILLMENT OF THE REQUIREMENTS FOR THE DEGREE OF DOCTOR OF PHILOSOPHY IN THE SCHOOL OF ENGINEERING AT BROWN UNIVERSITY

PROVIDENCE, RHODE ISLAND

MAY 2014

This dissertation by Peng Chen is accepted in its present form

by the School of Engineering as satisfying the

dissertation requirement for the degree of Doctor of Philosophy.

Date_____ _____

Allan F. Bower, Advisor

Recommended to the Graduate Council

Date_____ _____

Kyung-Suk Kim, Reader

Date_____ _____

Sharvan Kumar, Reader

Date_____ _____

Louis G. Hector, Jr., Reader

Approved by the Graduate Council

Date_____ _____

Peter Weber, Dean of the Graduate School

Vita

Peng Chen was born in Gansu province of China on February 10, 1983. He received his B.E. and M.E. degrees of Solid Mechanics from Xi'an Jiaotong University in 2004 and 2007, and his M.S. degree of Applied Mathematics from Brown University in 2011. He entered the Solid Mechanics group at Brown University for pursuing the Ph.D. degree in September 2007. Peng defended his Ph.D. dissertation on June 18th, 2013.

Acknowledgements

First and foremost, I would like to thank my advisor, Prof. Allan Bower, for accepting me as his doctoral student and offering me the opportunity to work on some of the most interesting problems in microstructure-based finite element analysis. He has had the greatest professional influence on my development as a scientist. His courage to tackle new and difficult problems and his patience to withstand the many failures that accompany such risks is admirable. The work in this dissertation has come out of very pleasant collaborations with him. I thank him for the support, guidance and patience, which helped to make this learning experience the one I will always remember.

I am grateful to the members of the dissertation committee, Prof. Kim, Prof. Kumar and Dr. Hector from GM, for their insightful comments and valuable suggestions making significant improvements to my dissertation. I would like to thank Dr. H. Ghassemi-Armaki for providing the micropillar compression measurements. Without these excellent experiments, I cannot finish the dissertation. I also would like to thank Dr. Bhat and Dr. Sadagopan from ArcelorMittal for supporting my Phd study and valuable discussions and collaboration during my PhD study. I thank ArcelorMittal Global R&D, East Chicago for funding support for the AHSS modeling. I also thank Prof. Shenoy for supporting the biopolymer networks simulation work in the dissertation. I have benefited a lot from useful conversations and enjoyable collaborations with many post-docs and students during my stay at Brown. Also, I would like to thank the faculty of Brown Solid Mechanics for providing many high-quality courses that contributed to my education.

I want to express my deepest appreciation to my family. This dissertation could not have been completed without their constant encouragement and support.

Contents

❖ This dissertation is based on the following peer-reviewed publications:

- Chen P., Ghassemi-Armaki H., Kumar K.S., Bower A.F., Bhat S., Sadagopan S. (2013). Microscale-calibrated modeling of the deformation response of dual-phase steels. (In preparation)
- Ghassemi-Armaki H., Chen P., Bhat S., Sadagopan S., Kumar K.S., Bower A.F. (2013). Microscale-calibrated modeling of the deformation response of low-carbon martensite. *Acta Materialia*. 61:3640-3652.
- Chen P. and Shenoy V.B. (2011). Strain stiffening induced by molecular motors in active crosslinked biopolymer networks. *Soft Matter*. 7(2):355-358.

List of Tables

List of Figures

Chapter 1. Introduction

1.1. Overview of modeling of advanced high strength steels (AHSS)

Recently, the modeling of mechanical properties of advanced high strength steels (AHSS) has received particular focus, and the need for integrated models capable of predicting the mechanical properties of AHSS is increasing. Modeling the mechanical behavior of AHSS is a critical step towards understanding the microstructure-property relations of AHSS, optimizing mechanical behavior and controlling their mechanical properties more rapidly than before using experiments [1]. Of particular important for industry is the need to predict local strength variations in formed components with accurate constitutive models.

The increased interest in modeling of AHSS is primarily attributed to the widespread usage of such steels in automotive industry, where materials with high ductility as well as high strength are required for the construction of car bodies or especially crash absorbent elements. AHSS were developed to offer the combination of high strength and ductility, weight reduction (e.g. ~10% mass reduction compared to mild steels [2]), improved passive safety features, energy saving considerations and environmental protection. AHSS primarily include fully martensitic (MS) steels, dual-phase (DP) steels, press-hardened boron (PHS) steels, transformation induced plasticity (TRIP) steels, complex phase (CP) steels, and high manganese content austenitic steels with twinning induced plasticity (TWIP) [3-6]. The majority of autobody components in

vehicle safety cages are designed using AHSS, especially DP steels (see Fig. 1.1), according to the results of the ULSAB-AVC Program (Ultra Light Steel Auto Body-Advanced Vehicle Concepts). Compared to conventional steels, AHSS have better mechanical performance (see Fig. 1.2). Some types of AHSS (e.g. MS steels) have ultra-high yield and tensile strengths relative to conventional steels. Others (e.g. DP and TRIP steels) have a higher strain hardening capacity resulting in a good strength-ductility balance.

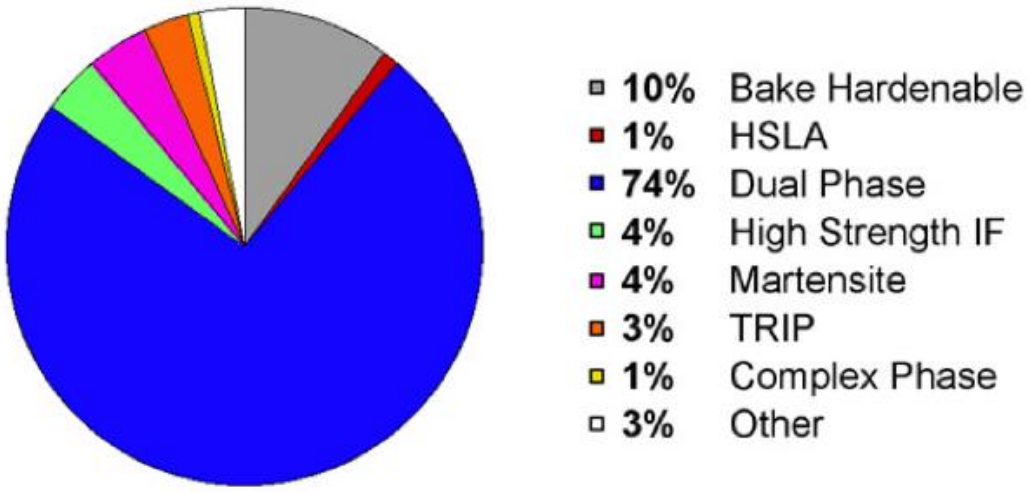

Fig. 1.1 ULSAB-AVC autobody structure steel type [7].

In Fig. 1.2, the MS, DP, TRIP, PHS, and CP steels are refered to as first generation AHSS [5]. The austenitic stainless steels (AUST.SS), TWIP steels and lightweight steels with induced plasticity (L-IP) are refered to as second generation AHSS [5]. Wide scale adoption of the second generation AHSS in the automotive industry has been hampered by high costs associated with heavily alloyed materials and by post-formed cracking [5, 6]. In this dissertation, we only focus on the first generation

AHSS, which are ferrite-based with multiple phases, including ferrite, martensite, austenite and/or retained austenite. MS steels are fully martensitic steels, DP steels consist of softer ferrite and harder martensite, and TRIP steels have the triple phase microstructure consisting of ferrite, bainite, and retained austenite. During the plastic deformation, the metastable austenite phase in TRIP steels is transformed into martensite. The martensite phase may be the most important phase of AHSS since it exists in all AHSS and posesses the highest tensile strength compared to other phases. The overall mechanical properties of AHSS depend on both the properties of the individual phases and also on the microstructural characteristics such as the grain size, volume fraction and morphology of individual phases [8, 9].

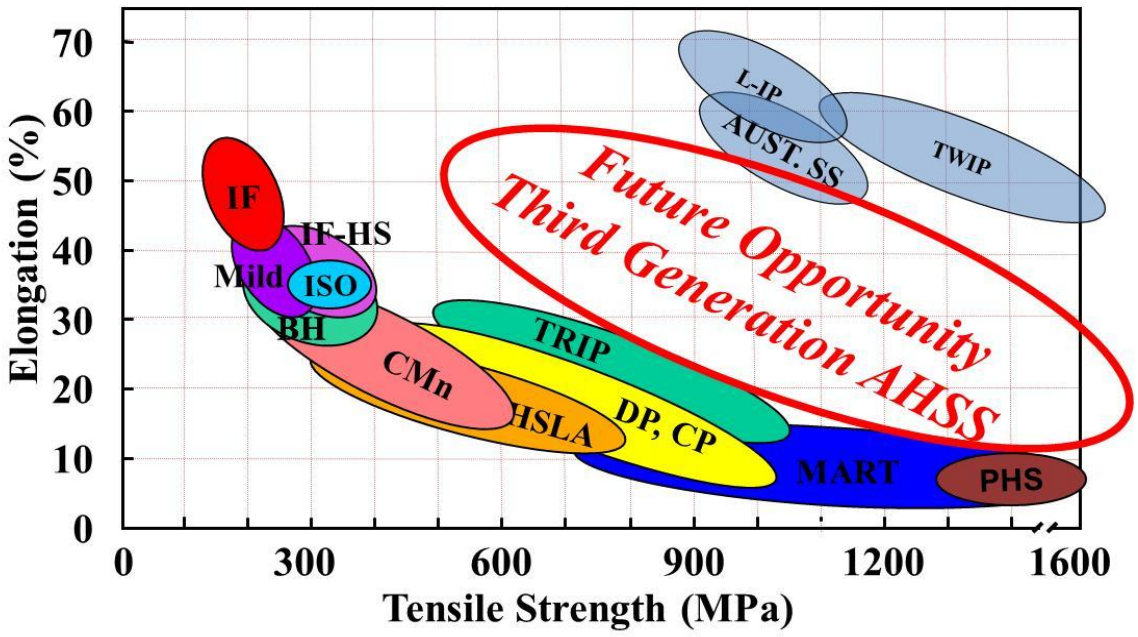

Fig. 1.2 Mechanical performance of advanced high strength steels compared to other conventional steels [5, 6].

Martensite in AHSS can adopt one of two general types of microstructure: martensite with a low carbon content (<0.6 wt.%C) has a lath microstructure; while martensite with a higher carbon content has a plate-like microstructure. In this dissertation, we focus on a low-carbon martensite (< 0.3 wt.%C), in which lath martensite is the predominant morphology [10-12]. A representative four-level lath martensite (α') microstructure, consisting of prior austenite grains, packets, blocks, and laths is shown schematically in Fig. 1.3 [13]. Laths typically have sub-micron dimensions; blocks consist of collections of laths, and in a 0.2 wt.%C steel, can have sizes ranging from 1-10 μm, a collection of blocks forms a packet with dimensions of order 3-150 μm, and packets develop within prior austenite grains with sizes between 10-500 μm [14, 15]. It is commonly accepted that the crystallographic orientations within the blocks are related to those of the prior austenite (γ) grains by the Kurdjumov-Sachs (K-S) orientation relationship, which is expressed as $(111)_{\gamma} // (110)_{\alpha'}, [101]_{\gamma} // [111]_{\alpha'}$ with a total of 24 possible crystallographic variants [13, 16]. The strength of martensite in AHSS depends primarily on its carbon content. The yield strength of martensite increases with increasing carbon content.

Compared to the four-level hierarchical microstructure of lath martensite, ferrite and austenite phases in AHSS have simple microstructures. Generally ferrite and austenite phases are assumed to be the body-centered cubic (BCC) and face-centered cubic (FCC) single crystals, respectively. The strength of ferrite in DP and TRIP steels in general is determined by its composition, grain size, initial dislocation density or residual stresses induced by the volume expansion associated with the austenite to martensite transformation.

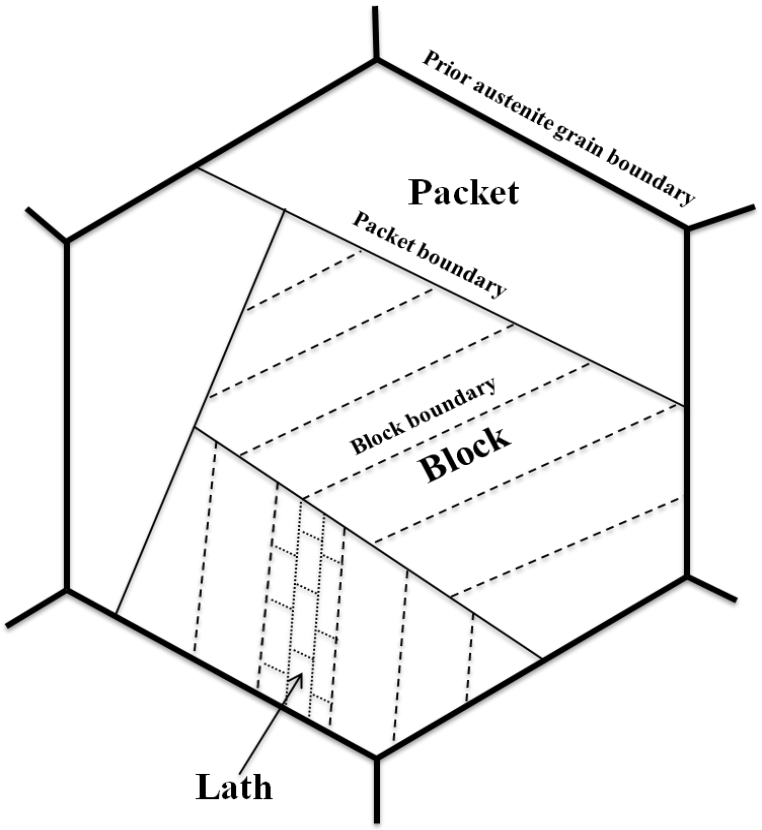

Fig. 1.3 Schematic showing the lath martensite microstructure typical of low carbon steels (adapted from [13]).

There is currently substantial focus in the computational material science community on building models to predict the flow behavior of AHSS from their microstructures. The simplest such models use a 2D idealization of the microstructure, together with a phenomenological isotropic J_2 flow rule and/or isotropic Ludwik hardening law to investigate the flow behaviors of DP and TRIP steels [9, 17, 18]. Realistic microstructures from 2D AHSS micrographs are used in these models [9, 17, 18]. Most recently, Ramazani *et al.* pointed out that the 2D plane strain modeling using a phenomenological isotropic J_2 flow rule, even with realistic microstructures,

underpredicts the flow strengh of DP steels, while 3D modeling gives a quantitatively reasonable description of the tensile flow curve [19]. The isotropic physically-based micromechanical models were also used to simulate the flow behavior of TRIP steels [20]. The model used for the simulations of the flow curves of the individual phases is based on the Mecking-Kocks theory [21, 22] and utilizes physical properties such as the microstructural parameters, the dislocation density, and the chemical composition of the individual phases [20]. The flow curves of TRIP steels were modeled by the successive application of a Gladman-type [23] mixture law for two-phase steels. Compared to the above-mentioned models, more sophisticated models use a crystal plasticity model based on Schmid's law to characterize the phases of DP steels [24, 25]. These generally model a ferritic microstructure using a rate-dependent single crystal plasticity model and the martensitic phase is addressed with either a crystal plasticity [25, 26] or an isotropic hardening J_2 flow model [24]. More recently, the effect of crystallographic orientation on the microscale flow behavior and plastic localization of DP steel has been investigated using 2D crystal plasticity model [27]. The crystal-plasticity-based models also offer the most detailed representation of a complete martensitic microstructure [28, 29]. These generally model a martensitic microstructure at the level of individual blocks, with laths represented approximately through material state variables characterizing dislocation densities.

Recently, several researchers have also focused on predicting the formability and failure behavior of AHSS from their predicted microstructures. The hole-expansion formability of DP steels has been modeled using Ludwik's equation to predict the flow curves of ferrite and martensite phases [30]. Other models used continuum Gurson-

Tvergaard-Needlemann (GTN) damage model to characterize stretch-flangeability in the hole-expansion formability of DP steels [31]. Using a 2D realistic microstructure of DP and TRIP steels and the phenomenological isotropic J_2 flow rule, together with Ludwik's equation to model the flow curves of individual phases, the failures of DP and TRIP steels were modeled [9, 17, 32]. These studies were successful in predicting the failure modes and ductility of DP and TRIP steels through plastic strain localization. More recently, the crystal plasticity finite element method was used to model the failures of DP steels [24, 27, 33]. Progress has also been made in modeling failure mechanisms such as void growth in martensitic microstructures [34]. The constitutive laws in crystal plasticity models, however, contain no material based length-scales, and therefore cannot capture microstructural size effects. Discrete dislocation models are a promising approach to address this [35], but at present fully three-dimensional discrete dislocation simulations cannot treat a sufficiently large enough material volume to model microstructural effects accurately.

In all prior models that were designed to predict the flow and failure behavior of AHSS, a significant outstanding challenge is that such models contain large numbers of material parameters, which must be fit to experimental data. Some of these, such as characteristic misorientations across lath, block or packet boundaries in martenstitic microstructures, can be determined experimentally [36]. Others, such as parameters characterizing flow strength or hardening relations of individual phases in AHSS, are more difficult to determine, and are usually selected so as to fit the experimentally measured macroscopic stress-strain behavior under some convenient strain path. This

fitting process is usually poorly conditioned, in the sense that many different combinations of material parameters can yield similar macroscopic stress-strain behavior.

Determining the material paramters characterizing flow or hardening relations of the individual phases in the complex microstructures of AHSS is critical to obtaining accurate predictions of its macroscopic behavior of AHSS. The mechanical behavior of individual phases of DP steels has been evaluated by using nanohardness or ultramicrohardness [24, 37], in-situ neutron diffraction [38] or in-situ high energy X-ray diffraction techniques [26, 39, 40]. Hardness measurements require a very small indentation contact area, and so are susceptible to indentation size effects [41]. In addition, it is difficult to ensure that the material being indented is homogeneous below the indenter. In the neutron diffraction technique, it is difficult to separate the ferrite and marteniste diffraction peaks due to the similar BCC and body-centered tetragonal (BCT) crystal structures in ferrite and martensite [26, 39, 40]. It has recently been shown that high energy X-ray diffraction has the capability of separating (200) and (211) diffraction peaks for the ferrite and martensite phases, but diffraction measurements can only measure the average lattice strain in the ferrite and martensite as a function of macroscopic stress, so extracting the mechanical response of the individual phases is difficult. A common approach has been to fit material parameters to match lattice strain measurements obtained using X-ray or neutron diffraction measurements [25-27]. Recently, an alternative to these approaches has been developed, in which micronscale specimens are extracted directly from the microstructure, and their load-displacement relation is subsequently determined using a nanoindenter. For example, Stewart *et al.* have used micropillar compression technique to measure the constituent behavior of DP

steels [42]; while Ghassemi-Armaki *et al.* have measured the mechanical response of individual martensite blocks and packets extracted from a fully martensitic steel [15]. The ability of micropillar experiments to determine the properties of the phases directly significantly improves the accuracy of microstructure-based simulations. Micropillar calibrated constitutive models have been described in [15].

1.2. Summary of the proposed approach for modeling of AHSS

We propose a micropillar-calibrated crystal-plasticity-finite-element approach to predict the deformation response of AHSS. Here is the summary of the approach.

a) Measuring the flow properties of individual phases in AHSS using micropillar compression tests. Dr. H. Ghassemi-Armaki at Brown University has measured the flow and hardening behavior of individual phases in AHSS using micropillar compression tests [15, 43].

b) Fitting micropillar compression data using crystal-plasticity models. The material parameters required in crystal-plasticity models for individual phases of AHSS are directly extracted from the flow curves of individual phases measured by the micropillar compression tests in (a). The micropillar-calibrated crystal plasticity models will be used in macroscopic simulations in (c) and (d). The determined properties of the phases directly significantly improve the accuracy of microstructure-based simulations.

c) Generating fully 3D representative volume elements (RVEs) and predicting the macroscopic flow curves and flow potentials of AHSS. A simulated annealing process [44] is used to generate the fully 3D RVEs of AHSS. The

overall macroscopic uniaxial stress-strain curves and flow potential surfaces of AHSS are predicted using the crystal-plasticity models with parameters determined from micropillar compression tests in (b).

d) Predicting the forming limit strains using the macroscopic non-associated plasticity finite element method. The parameters of the macroscopic non-associated plasticity model are fit using the 3D RVEs subjected to multiaxial loading with the micropillar-calibrated crystal plasticity modes in (b). The forming limit strains are predicted using a 3D sheet necking finite element model [45, 46].

1.3. AHSS selected for study

To apply the proposed approach described in the previous section, we focus on two types of AHSS: MS and DP steels. We investigate the deformation response of both AHSS types in the dissertation. The first type of AHSS to be considered, MS steel includes only the martensite phase (see Fig. 1.4). MS steels have some of the highest strength levels and strength-to-weight ratios among materials currently available for body structure applications in the automotive industry. These properties make them attractive materials for components where high strength is critically important, such as bumper reinforcement beams, door intrusion beams, side sill reinforcements, belt line reinforcements, springs, and clips. More widespread use is hampered primarily by their limited ductility and formability. Therefore, there is considerable interest in finding ways to optimize their microstructure so as to improve their ductility. With this in mind, the

influence of microstructural variables on the flow and failure behavior of MS steels is an issue of considerable current interest.

The second steel is a dual-phase (DP) steel that includes both soft ferrite and hard martensite phases (see Fig. 1.4). These steels were developed in the mid-seventies in order to meet the increasing needs of weight reduction and improved crash performance of vehicles. They have a typical microstructure consisting of a soft ferrite phase with dispersed islands of a hard martensite phase [47-49] (see Fig. 1.4). DP steels are particularly widely used in automotive applications such as bumper reinforcement beams, door intrusion beams, seating components and structural cross members due to their remarkable combination of strength and ductility compared to MS steels. The unusual properties of DP steels can be attributed to their complex and highly heterogeneous microstructure (see Fig. 1.4). This complexity can be exploited to generate DP steels with a wide range of properties that include high tensile to yield strength ratio, continuous yielding, high work hardening rate and good ductility.

The microstructures of the two types of AHSS are shown in Fig. 1.4. The MS steel can be thought of as a DP steel with the limiting volume fraction of 100% martensite. The DP steels have between 35% and 65% of martensite, with a higher volume fraction in DP980. In addition to the different volume fraction of martensite, the ferrite grains are finer in DP steel DP980 than in DP steel DF140T. The bulk uniaxial stress-strain curves of the two types of AHSS are shown in Fig. 1.5. The fully martensitic steel has higher nominal strength but less ductility, while the two DP steels DF140T and DP980 have lower nominal strength but better ductility. In addition, the two DP steels have similar nominal strength but different ductilities.

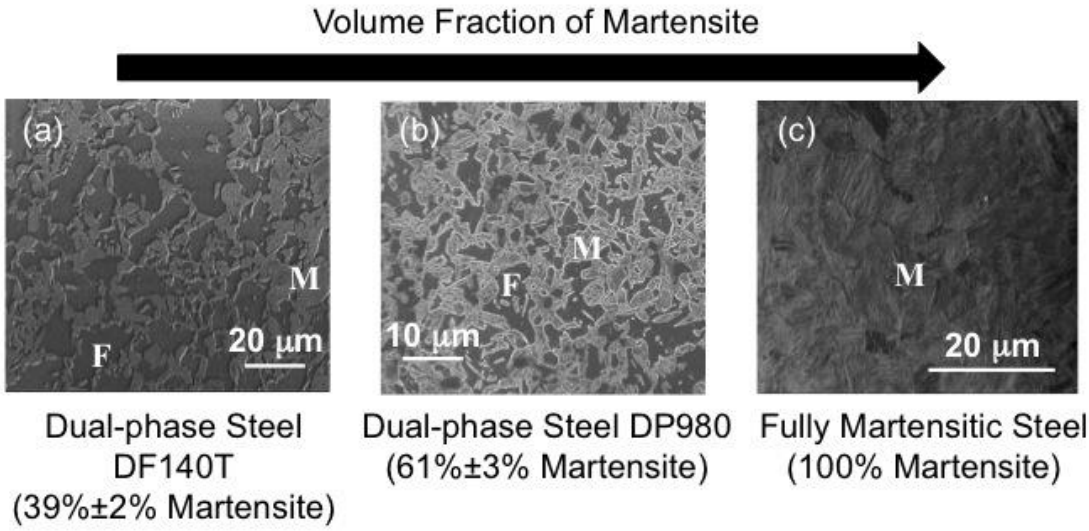

Fig. 1.4 Comparison of the microstructures of three AHSS: (a) DP steel DF140T, (b) DP steels DP980 and (c) fully martensitic steel. Light regions are martensite phase (marked by "M") and dark regions are ferrite phase (marked by "F"). (SEM images provided by Dr. H. Ghassemi-Armaki at Brown University).

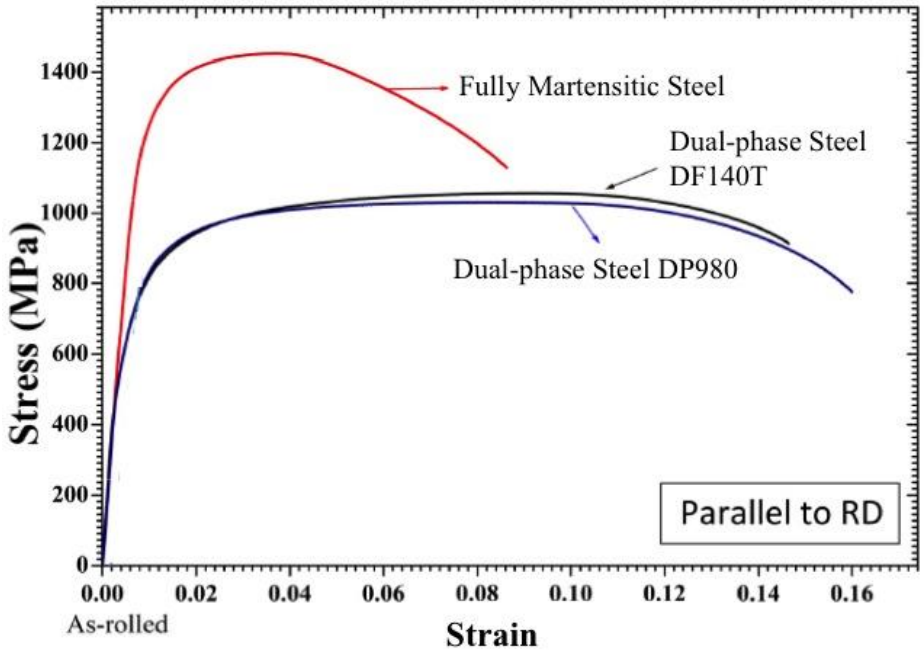

Fig. 1.5 Bulk uniaxial stress-strain curves of three AHSS along rolling direction (RD). (Data provided by Dr. H. Ghassemi-Armaki at Brown University).

Our computations begin by addressing the behavior of the fully martensitic steel. Using the measurements of the deformation response of microscale volumes of material extracted from a low-carbon MS sheet steel (MartINsite® 190), we will predict the overall response of the bulk MS microstructure in Section 2.8, using crystal-plasticity-based finite element simulations. The micropillar compression experimental data are used to determine material properties in Section 2.6, by using an optimization process to determine parameters that best fit the experimental data. Fully 3D models of the MS microstructure are then assembled using a microstructure reconstruction technique [44], and finite element computations are used to determine the macroscopic uniaxial stress-strain response of the material in Section 2.8. The predicted macroscopic response is shown to be in excellent agreement with experimental measurements. Finally, our microstructure-based model predicts the detailed distributions of prior austenite/packet/block boundary stresses in MS microstructure in Section 2.8, which provides insights into their effect on the bulk strength or ductility.

We will next study and compare the microscale flow and hardening behavior of DP steels (DF140T and DP980) in Sections 2.7, 3.5 and 4.4. These are both commercial grade steels with ~0.15 wt.% and ~0.1 wt.% bulk carbon content, respectively. The two steels have significantly different microstructures: for example, the martensite volume fraction in DP980 is approximately 50% greater than that in DF140T. Despite these differences, they have nearly identical uniaxial tensile stress-strain behavior. To explain these observations, the material parameters in the crystal-plasticity-based constitutive equations for the ferritic and martensitic phases of the steels will be determined using

micropillar compression stress-strain curves in Sections 2.7 and 3.5. Based on these measurements, a 3D computational model will be created of each DP steel microstructure in Section 4.3, and subjected to loading representing uniaxial tension.

This combination of experiment and computation has been found to predict the uniaxial behavior of both DP steels accurately. In addition, it provides a number of insights into the microstructural origins of their tensile behavior. In particular, the martensite phase in DF140T is found to have a compressive strength approximately twice that of the martensite phase in DP980. This strength difference is offset by the different volume fractions of martensite in the two steels, explaining how they exhibit nearly identical tensile flow strength. In addition, our results show that the ferritic micropillars have a strongly orientation dependent flow strength, which cannot be explained by a conventional crystal plasticity model based on Schmid's law. We find that these discrepancies can be resolved by adopting more sophisticated crystal plasticity models developed recently for BCC materials with non-Schmid behavior. The non-Schmid behavior in the ferrite leads to a small reduction in the tensile flow stress of the dual phase steels, as well as a small tension-compression asymmetry. Finally, our microstructure-based model predicts the detailed distributions of strain, ferrite/martensite interfacial stress and prior austenite/block boundary stress in both steel microstructures in Section 4.4, which provide insights into their different tensile ductility.

To measure and compare the tension-compression asymmetry induced by the non-Schmid behavior in the ferrite phase of DP steels, a non-associated plastic flow model is adopted and the forming limit strains in both DP steels are predicted in Section 4.5. The higher strength-differential value and lower forming limit strain under some loading

paths in DF140T will be predicted, which also imply the less ductility compared to DP980.

1.4. Overview of mechanical behavior of active biopolymer networks

If plant and animal cells are regarded as an automobile vehicle, the cytoskeleton is the body of the cell vehicle. In the previous Sections and Chapters 2-4, we described the mechanical behavior of AHSS used widely in automobile vehicle body parts. In this section and Chapter 5, we will discuss the mechanical behavior of cytoskeleton, especially active biopolymer networks, which are the body parts of cell vehicles. Although AHSS and active biopolymer networks are the main constituent materials of body parts of automobile vehicles and cells, respectively, the physical mechanisms involved in the deformation response of both materials are totally distinct.

The mechanical properties of plant and animal cells are governed by the cytoskeleton, which is a flexible and dynamic network of biopolymer fibers combined with a group of associated regulatory and crosslinking proteins [50, 51]. One of the key aspects of the mechanical behavior of these networks is their highly nonlinear elastic response to applied stresses [52], in particular their ability to strain stiffen by orders of magnitude when subject to large stresses. Cells also employ molecular motors to convert chemical energy into mechanical work [50]. Motors generate internal stress in the networks even in the absence of external loading [50, 53]. In this manner, cells can regulate their mechanical properties by using both active and passive components. Fig. 1.6 shows the force generator in fibroblast cells and the force is generated by three main components, that is, actin filament, Myosin II motors and crosslinkers.

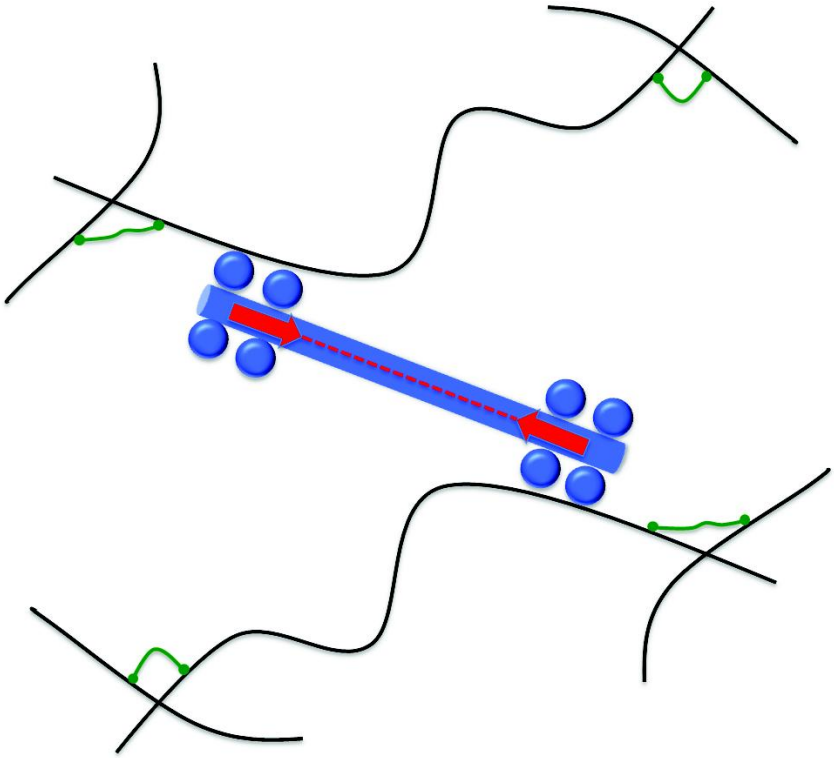

Fig. 1.6 A schematic of actin filaments (black lines) with myosin motors (blue) and compliant crosslinks (green lines). Myosin motor exerts equal and opposite forces on the filaments on which it is attached, which results in a force dipole (pair of red arrows). These forces lead to the extension of the filamin crosslinks.

While the mechanical behavior of semiflexible polymer networks with compliant and rigid crosslinks has been studied in detail both experimentally and theoretically [54-61], the interplay between active mechanisms of stress generation through motor activity and passive strain hardening properties of crosslinks has only been considered very recently [53, 59]. In this regard, reconstituted actin networks can be particularly useful, since the density of crosslinks and motors can be varied in a desired manner to gain insights into the mechanisms of strain hardening and nonlinear elastic response. Indeed, recent experiments on networks that consist of actin filaments crosslinked by

filamin A (FLNa) and bipolar filaments of muscle myosin II show that in the absence of any applied loads [59], the motors stiffen the network by about two orders of magnitude. The degree of stiffening was found to increase with increasing density of myosin motors. Another key observation from this study relates to the magnitude of stiffening caused by compliant and incompliant crosslinks. While FLNa is a large, highly flexible dimer that promotes orthogonal F-actin crosslinking, scruin is an incompliant crosslink. Interestingly, it was found that in distinct contrast to FLNa, scruin does not promote active stiffening of F-actin networks upon addition of myosin. These results clearly show that actomyosin contractility when combined with appropriate crosslinks can allow the cell to operate in a nonlinear regime to actively control its mechanical response.

Why do compliant crosslinks in active networks lead to large strain stiffening while no significant increase in stiffness is observed in the case of incompliant crosslinks? To answer this question and to quantitatively study the interplay of internal strains generated by molecular motors and external loads, we will study the mechanical response of active networks using finite element simulations in Chapter 5.

A number of approaches including mean-field models, effective medium theory and numerical simulations have been used to study the elastic response of passive networks with both compliant and incompliant crosslinks [54-57]. However the role of crosslinks in the mechanical response of networks with molecular motors has not been considered theoretically. Our work in Chapter 5 shows that the nature and density of the crosslinks play a key role in determining the strain stiffening response in active biopolymer networks. FLNa is a crosslink that is compliant at small pulling forces, but is stiff beyond a critical value of stretch [52]. We find that even in the absence of

applied loads, motors lead to almost completely stretch out the compliant crosslinks taking them into the stiffened regime, which in turn also leads to bending of the filaments. As the crosslinks are fully stretched, the applied load is accommodated by the deformation of filaments. Since it is more difficult to deform the filaments compared to stretching of compliant crosslinks, the network stiffens by as much as two orders of magnitude compared to the case when motors are absent. On the other hand, when the crosslinks are incompliant, the contractile forces due to motors do not alter the network morphology in a significant manner leading to much lesser stiffening (typically by a factor of two) in agreement with experiments [59].

1.5. Outline of dissertation

The dissertation is divided into two parts. The first part (Chapters 2-4) will discuss the micropillar-calibrated modeling of low-carbon martensitic steels and DP steels. The second part (Chapter 5) will discuss the strain-stiffening modeling of active biopolymer networks.

In Chapter 2, a brief overview of the martensite phase in steels and the experimental data of lath martensitic micropillar compression tests are first provided. The lath martensitic microstructure is generated following a simulated annealing process [44] with brick meshing. Using the dislocation-density-based crystal plasticity model incorporating the crystalline structure, anisotropy, orientation relations, prior austenite orientations and initial dislocation densities of lath martensite, the material parameters of lath martensite in MS and DP steels will be determined through combining the micropillar compression tests and a MATLAB optimization procedure. The dislocation-

density-based crystal plasticity model and its implementation in an ABAQUS UMAT will also be described. To confirm the micropillar compression tests of lath martensite, the uniaxial stress-strain curves of 3D fully martensitic steel RVEs are predicted in the end of Chapter 2, which are in excellent agreement with the experimental measurements. The prior austenite/packet/block boundary stress distributions are also analyzed to provide insights into their effect on the bulk strength or ductility of MS steels.

In Chapter 3, the overview of ferrite phase of AHSS and the experimental data of ferrite micropillar compression tests will first be introduced. The mechanical properties and material parameters in the crystal plasticity model of the ferrite phase in AHSS will then be investigated in detail. The procedure for determining material parameters is similar to the one used for lath martensite in Chapter 2. The non-Schmid Bassani-Wu crystal plasticity model for the ferrite phase will be described in detail in this Chapter, including its implementation in an ABAQUS UMAT.

In Chapter 4, after determining the volume fraction of martensite in DP steels via measuring the area fraction of martesite in SEM images, the 3D DP heterogeneous microstructures are generated using the technique outlined in Chapter 2. Then the uniaxial stress-strain curves of 3D DP RVEs are predicted, which are good agreement with the experimental measurements. To investigate the different ductilities of the two commercial DP steels with similar nominal strength, the macroscopic non-associated flow behavior resulting from the non-Schmid behavior of the ferritic phase of the two DP steels are studied and compared. The strain/stress partitioning and interfacial stress distributions are also analyzed to explain the different ductilities of these two DP steels.

The second part of the dissertation (Chapter 5) will investigate the strain-stiffening behavior of active biopolymer networks using finite element method. The random 2D biopolymer network models with two distinct crosslinkers are generated using MATLAB, and then are sheared up to 100% macroscopic strain to study the strain-stiffening behavior. The effect of myosin motors modeled as static force-dipoles on the biopolymer networks with two different crosslinks will also be discussed in detail in Chapter 5.

The research in this dissertation is summarized in Chapter 6, and suggestions for future work are made.

Chapter 2. Mechanical Behavior of Martensite Phase in AHSS

To predict the overall mechanical behavior of AHSS, material parameters in crystal plasticity models must be fit to experimental data. Usually these parameters are selected so as to fit the experimentally measured macroscopic stress-strain behavior under some convenient strain path. This fitting process is usually poorly conditioned, in the sense that many different combinations of material parameters can yield similar macroscopic stress-strain behavior. To overcome the limitation, in this and next Chapters, material parameters of martensite and ferrite phases in AHSS are fit to micropillar compression experiments, which directly measure the properties of individual phases within a complex multiphase microstructures.

In this Chapter, the mechanical behavior of the martensite phase in AHSS will be discussed. After an overview of the martensite phase in AHSS in Section 2.1, experimental data from lath martensite micropillar compression tests will be introduced in Section 2.2. The numerical generation of a lath martensite microstructure will be discussed in detail in Section 2.3, where the four-level hierarchical microstructures of lath martensite will be generated. The dislocation-density-based crystal plasticity model for lath martensite blocks and its implementation in an ABAQUS UMAT will be described in Sections 2.4 and 2.5. Finally, the material properties of lath martensite in AHSS will be determined in Sections 2.6 and 2.7 through fitting the micropillar compression stress-

strain curves of lath martensites in different AHSS. A 3D RVE of fully martensitic steels will be constructed using the method described in Section 2.3 and the overall uniaxial stress-strain curves of fully martensitic steels will be predicted in Section 2.8. These are shown to be in excellent agreement with the experimental measurements.

2.1. Overview of martensite phase of AHSS

Martensite, named in honor of the German engineer Adolf Martens, is one of the most important constituents in AHSS [62]. It is formed from austenite containing carbon atoms, based on the diffusionless nature of the martensitic transformation, and inherits the carbon atoms of the parent austenite [63]. The carbon atoms are trapped in octahedral interstitial sites between iron atoms, producing a tetragonal BCC structure (also known as a BCT structure). Together with the volume expansion when FCC austenite transforms to BCT martensite, the lattice-invariant deformation which results from slip or twinning plastic deformation mechanism induces a high density of dislocations and/or twins in the martensite microstructures [63].

The overall response of the martensite microstructure has been found to be highly sensitive to both its composition and overall size scale (which is largely a function of thermo-mechanical processing history). For example, the strain hardening rate of MS steels increases with increasing carbon content [63, 64], partly as a result of solute strengthening, and partly because increasing carbon content tends to lead to finer martensitic microstructures [16, 65]. The yield strength of lath martensite has been shown to scale with the inverse square root of the characteristic size of the microstructure (e.g. grain, block or packet size), as predicted by the Hall-Petch formula [14, 66-70]. This size

dependence has been attributed to the tendency of inter-block and packet boundaries to block dislocation motion: for example, micro-cantilever tests have shown that the initial hardening rate of specimens containing a block boundary is higher than that in a specimen consisting of a single block [70], possibly as a result of dislocation pile-up adjacent to the block boundary. Likewise, nanoindentation has been used to probe the strength of single blocks of martensite in low carbon steels with attempts to separate the strengthening contributions of the matrix and the block/packet boundaries in martensite [71-73]. A rather surprising finding from an in-situ nanoindentation study in the TEM [74] and at odds with the line of reasoning in [70] was that lath boundaries were effective in stopping matrix dislocations, at producing pile-ups and activating sources in adjacent laths whereas block boundaries acted as sinks for matrix dislocations and were not effective in producing dislocation pile-ups and this was attributed to the crystallography of the block boundary.

One of the interesting properties of the martensite phase in steels is the strength-differential effect. Around 1970, it was established that as-hardened, quenched or tempered martensitic steels are significantly stronger in uniaxial compression than in uniaxial tension, which is known as the strength-differential effect [75-80]. The strength difference between the compressive and tensile flow stress decreases with increasing tempering temperature and increases with the carbon content [75, 79]. Several hypotheses have been advanced to explain the strength-differential effect [75], for example, the microcrack hypothesis, the residual-stress hypothesis, the retained-austenite hypothesis, the internal Bauschinger hypothesis, the solute/dislocation interaction hypothesis and the volume-expansion hypothesis. Later, Hirth and Cohen proposed a nonlinear model which

can account for a 3-6% strength-differential [75]. Spitzig *et al.* argued that the strength-differential effect is primarily a manifestation of the general pressure dependence of flow stress [79, 80]. Through evaluating the strength-differential effect in four commercial steels, Singh *et al.* showed that the pressure dependent flow stress model proposed by Spitzig and Richmond [81] appears better than the nonlinear model proposed by Hirth and Cohen [75] to explain the strength-differential effect in martensite.

However, whether there exists the strength-differential effect in the martensite phase to be studied is still undetermined experimentally. The strength-differential effect of martensite will be ignored in the following modeling work.

In addition to fully martensitic steels, the behavior of the martensite phase in dual phase steels is also of great interest. Two decades ago, several experiments showed that plastic deformation of the martensite phase in DP steels is absent except for the regions very close to the fracture surface in the high-carbon DP steels [82-85], which is similar to other high strength low alloy steels where the ferrite phase deforms while the harder phase does not experience any significant deformation. But in low-carbon (<0.1 wt.%) DP steels (like the DP steels to be considered in the disseratation), Mazinani and Poole observed that substantial martensite plasticity occurs under certain conditions [8], for example when the strength of martensite is reduced either by lowering its carbon concentration or by tempering. Rashid and Cprek also observed that martensite deforms plastically after excessive straining of ferrite matrix [86].

Based on the observation of martensite plasticity in low-carbon DP steels, various models of hardening behavior in the martensitic phase of DP steels have been used to predict the overall behavior of DP steels. For example, Kadkhodapour *et al.* assumed that

the martensitic phase in commercial DP980 steel exhibits a nearly flat flow curves (elastic-nearly perfectly plasticity) [24]. In contrast, the martensite phase in DP980 was assumed to have linear hardening behavior in Sun *et al.*'s work [9]. All these assumptions are based on phenomelogical measurement, and none of previous work directly extracts the plastic flow and hardening behavior of martensite phase in AHSS without the influence of other phases. The accurate measurement of material properties of the martensite phase in AHSS is important to predict the overall deformation reponse of AHSS. The micropillar compression test is a good technique to accurately extract the material properties of individual phase in multiphase steels. In the following sections of this Chapter, we will use a combination of micropillar compression tests and dislocation-density-based crystal plasticity model to extract the plastic flow and hardening properties of the martensite phase in two types of AHSS.

2.2. Experimental data of lath martensitic micropillar compression tests

All of the experiments in this Section were conducted by Dr. H. Ghassemi-Armaki at Brown University [15, 43]. Several micropillars ranging in diameter from 0.3 μm to 3.6 μm were excised from the as-rolled MS and DP steel sheets. As the lath dimensions for low carbon martensite are typically in the 200 nm regime [71], all micropillars were expected to contain multiple laths. However, since the block dimensions are typically in the 1-4 μm range, the micropillars at the large end of the range examined will likely contain multiple blocks and possibly even include a packet boundary in the cross-section and perhaps more in the through-thickness of the

micropillar whereas in the sub-micron pillar size range, the likelihood of including multiple blocks diminishes.

Uniaxial compression stress-strain curves obtained by deforming micropillars of various diameters from MS steel sheet are shown in Fig. 2.1(a) and (b). The stress-strain curves shown in Fig. 2.1(a) are for pillars that equal or exceed 2 μm in diameter whereas those presented in Fig. 2.1(b) correspond to sub-micron pillars. The stress-strain curves in Fig. 2.1(a) can be separated into two general groups. In Fig. 2.1(a), micropillars 1 and 2 (which have a diameter of 2.0 μm) begin yielding at ~1200 MPa and show elastic-nearly perfectly plastic behavior. Micropillars 3 and 4, which have diameters of 3.6 μm and 2.8 μm, appear to display a slightly higher proportional limit but more importantly show pronounced hardening. A set of stress-strain curves is provided in Fig. 2.1(b) for pillars that are typically < 1 μm in diameter. A large scatter in response is observed, both, in terms of the stress required for noticeable onset of plastic deformation as well the subsequent hardening rate. The exact reason for this large scatter is not well understood at the moment. The flow stress at 1% plastic strain is plotted as a function of pillar diameter in Fig. 2.1(c) for twenty-six micropillars. The figure confirms that for diameters greater than 1 μm, the flow stress scatter is minimal and the flow stress is independent of the pillar diameter. Note that martensites extracted from the two DP steels considered in the dissertation show qualitatively similar behavior [43]. In the following modeling of martensite micropillars, we only consider martensite pillars with diameter equal to or greater than 2 μm for MS steel.

(a)

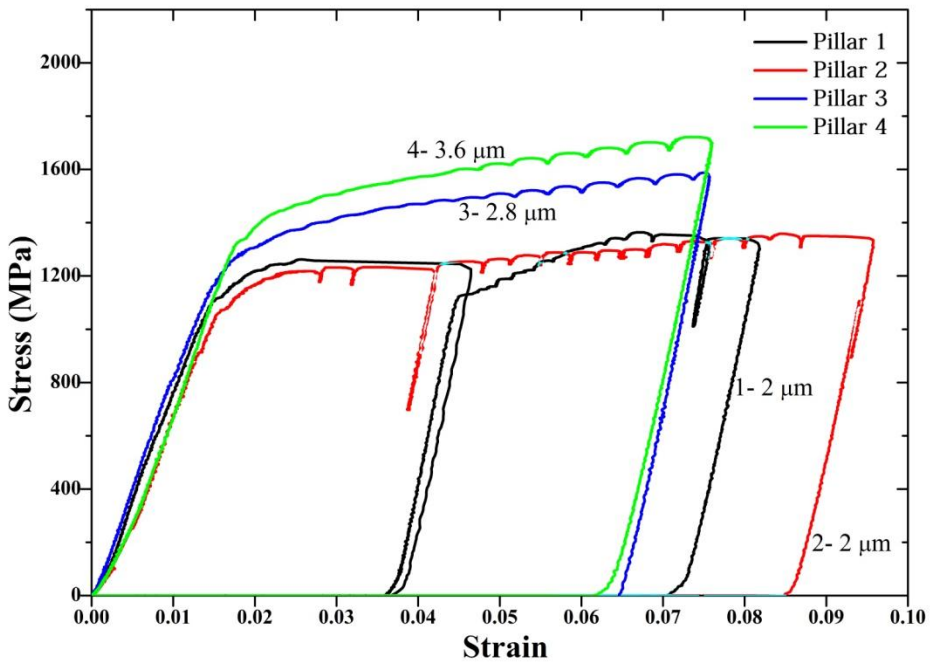
Pillar 1
Pillar 2
Pillar 3
Pillar 4
4- 3.6 µm
3- 2.8 µm
1- 2 µm
2- 2 µm
Stress (MPa)
Strain
0
400
800
1200
1600
2000
0.00
0.01
0.02
0.03
0.04
0.05
0.06
0.07
0.08
0.09
0.10

(b)

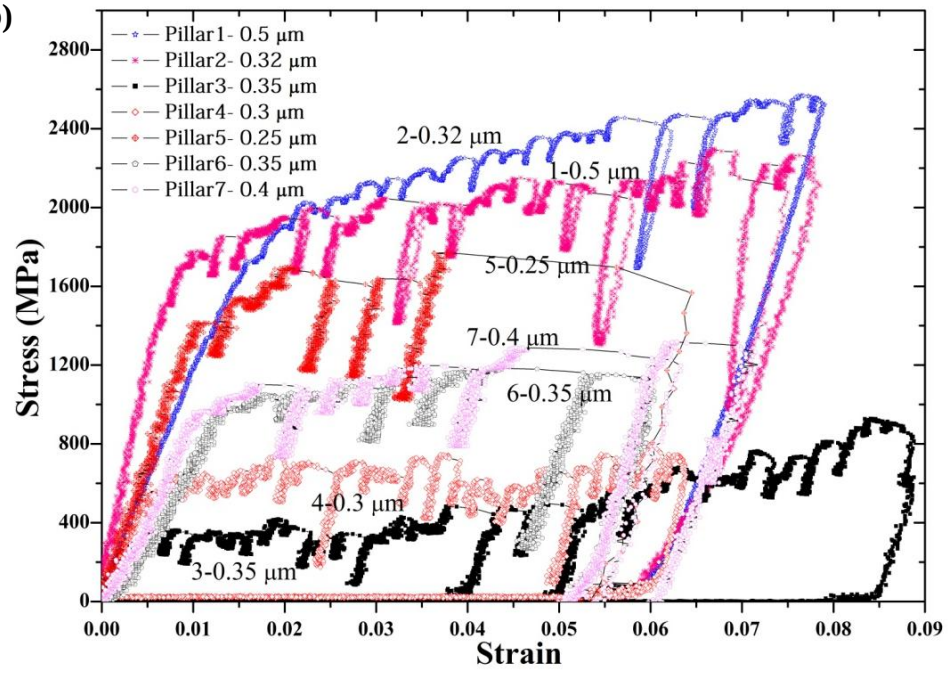
Pillar1- 0.5 µm
Pillar2- 0.32 µm
Pillar3- 0.35 µm
Pillar4- 0.3 µm
Pillar5- 0.25 µm
Pillar6- 0.35 µm
Pillar7- 0.4 µm
2-0.32 µm
1-0.5 µm
5-0.25 µm
7-0.4 µm
6-0.35 µm
4-0.3 µm
3-0.35 µm
Stress (MPa)
Strain
0
400
800
1200
1600
2000
2400
2800
0.00
0.01
0.02
0.03
0.04
0.05
0.06
0.07
0.08
0.09

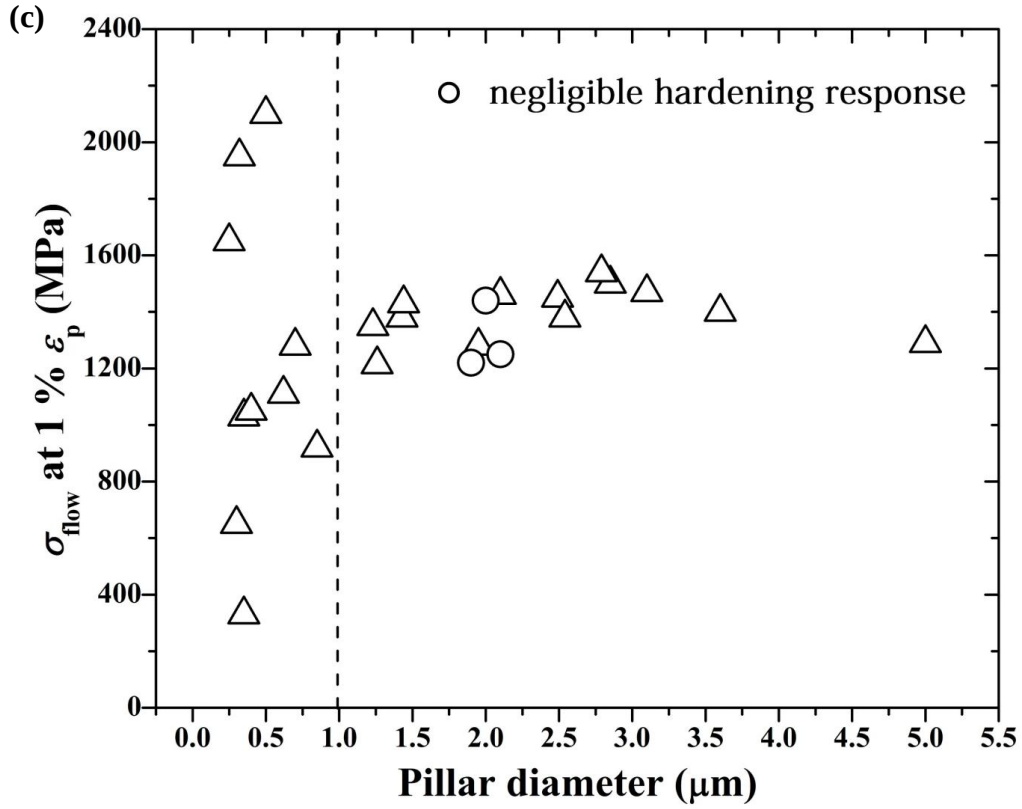

Fig. 2.1 Micropillar compression stress-strain curves for the as-rolled martensitic steel sheet. In (a) Micropillars 1 and 2 exhibit marginal hardening whereas micropillars 3 and 4 show pronounced hardening. All four micropillars have diameters > 1 μm. In contrast, in (b) submicron pillars show a large range of response in flow behavior. The variation in flow stress at 1% plastic strain is shown as a function of pillar diameter in (c) and it is evident that the spread in data diminishes dramtically above a pillar diameter of ~1 μm. The figures are provided by Dr. H. Ghassemi-Armaki at Brown University [15].

Some further insights into the difference in behavior between the two sets of pillars in Fig. 2.1(a) were obtained by examining the micropillars after deformation. Micropillars 1 and 2 (which showed elastic-nearly perfectly plastic behavior) deform by forming a pronounced slip band and what appears to be single slip (Fig. 2.2(a) for the case of micropillar 1; micropillar 2 is shown later in the modeling section in Fig. 2.8(c)). Micropillars 3 and 4 (which exhibit strain hardening behavior) show a more uniform

deformation mode and evidence for multiple slip (Fig. 2.3(a) for the case of micropillar 3; micropillar 4 is shown later in the modeling section in Fig. 2.8(f)).

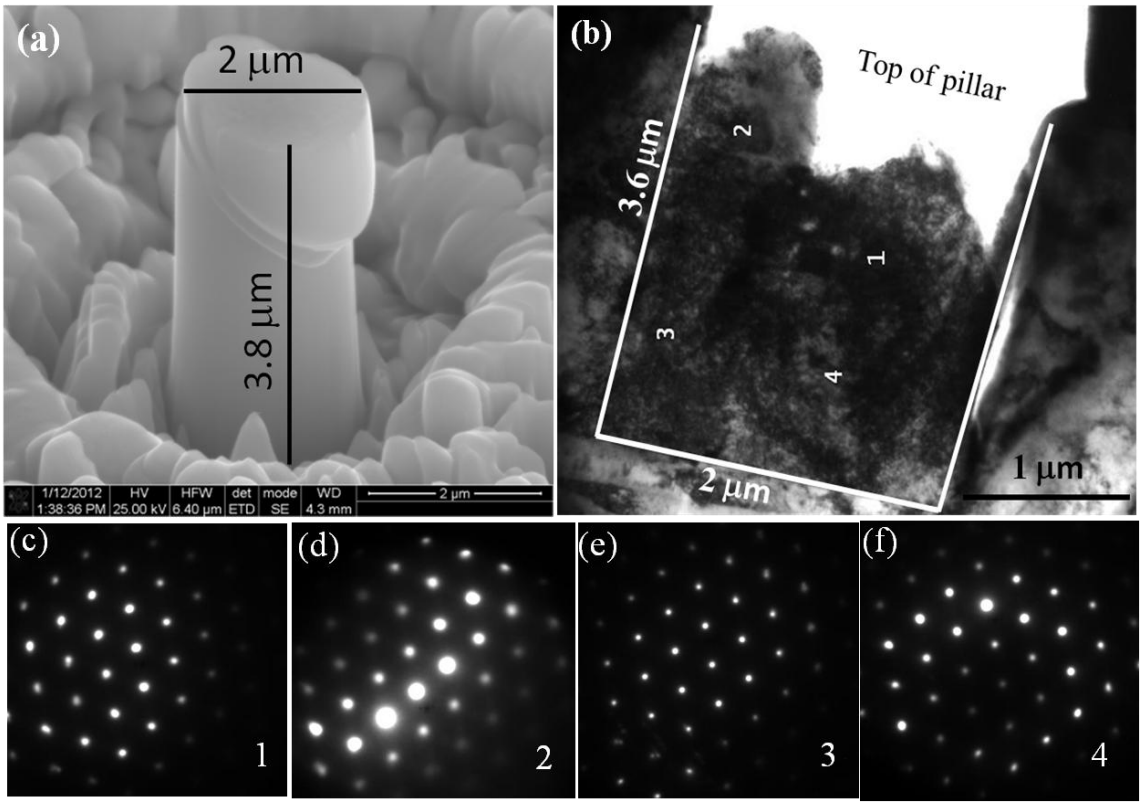

Fig. 2.2 Microstructural observations of deformed micropillar 1 (stress-strain curve in Fig. 2.1) prepared by FIB milling: (a) SEM and (b) low magnification bright field TEM image of the vertical section of the deformed micropillar. (c-f) Selected area diffraction patterns from four locations identified in (b) as 1, 2, 3 and 4 confirm the microstructure is composed of a single martensite block. The figures are provided by Dr. H. Ghassemi-Armaki at Brown University [15].

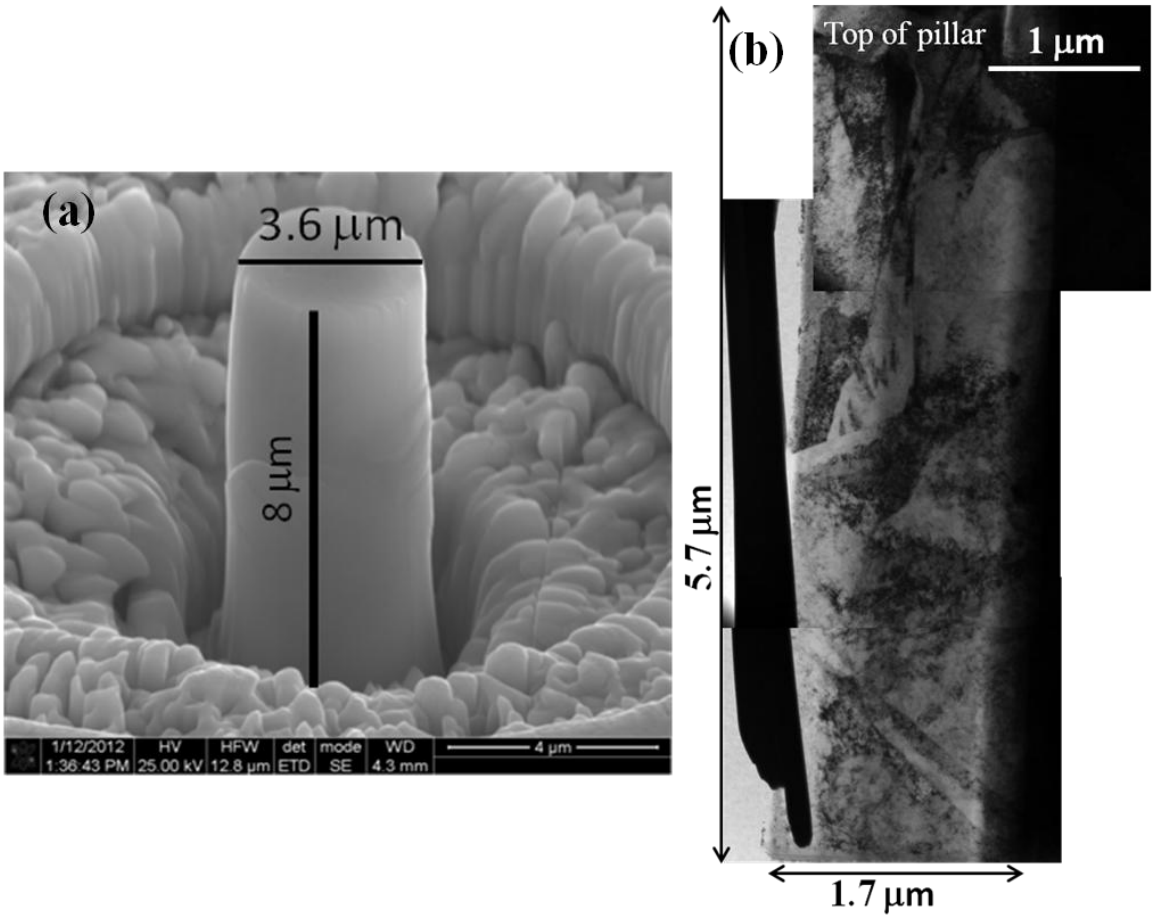

Fig. 2.3(a) SEM and (b) composite bright field TEM image of the entire vertical section of the deformed micropillar 3 (stress-strain curve in Fig. 2.1) revealing the presence of multiple blocks and perhaps one or more packet boundaries. The figures are provided by Dr. H. Ghassemi-Armaki at Brown University [15].

From experiments, it is verified directly that micropillar 1 consists of a single martensite block, while micropillar 3 contains a block or packet boundary. For this purpose, TEM samples were extracted from the deformed micropillars by FIB milling and lift-out. The micropillar 1 has a height of around 3.8 μm after deformation, as shown in Fig. 2.2(a); a low-magnification TEM image of a vertical section of the micropillar obtained by FIB lift-out in Fig. 2.2(b) corresponds to about 3.6 μm in the vertical direction (~ 0.2 μm of the top of the micropillar has been milled during thinning of TEM

sample). The uniform contrast in the bright field image suggests the absence of any block or packet boundaries. Selected area diffraction patterns from 4 regions labeled as (1-4) are presented in Fig. 2.2(c-f) and these verify the above observation that the entire pillar represents a single orientation and does not include block or packet boundaries. Post-deformation bright field TEM images from the different locations of the vertical section of micropillar 3 are presented in the form of a montage in Fig. 2.3(b). The composite bright field TEM image clearly shows multiple block boundaries and perhaps packet boundaries in the micropillar. Our simulations, to be described in detail in Sections 2.6 and 2.7, suggest that the increased hardening is caused by block or packet boundaries and arises as a consequence of geometric constraints. A similar strengthening influence of block boundaries has been observed in micro-cantilever tests on a martensitic specimen [70].

In the context of examining the role of a boundary in influencing plastic flow in a micropillar, Kunz and Greer [87] have reported a reduction in hardening rate in bi-crystal Al specimens and have suggested that the boundary serves as a dislocation sink; in contrast, Ng and Ngan [88] observed an increase in hardening in bi-crystal Al micropillars and reported dislocation accumulation at the boundary but the size range of pillars examined in the two studies was different. Many prior nano- and micropillar studies have focused on the influence of pillar size on their strength [89-95]. Generally, the results show that strength is higher at smaller size although this phenomenon is less pronounced in pillars approaching 2 μm diameter in crystals with cubic structures [94]. Our results suggest that size effects are insignificant in martensite pillars with diameters exceeding 2.0μm. Data for these micropillars are therefore taken to represent behavior of

the bulk martensite, and can accordingly be used to determine material parameters for crystal-plasticity material models for use in finite element simulations. These computations are described in more detail in the following Sections.

2.3. Generation of lath martensitic microstructures

Two major morphologies of the martensite phase, namely lath and plate, form in steels [10, 63]. Lath martensite forms in low- and medium-carbon steels and consists of parallel arrays of lath-shaped crystals. Plate martensite forms in high-carbon steels with non-parallel arrays. The AHSS under consideration belong to low-carbon steels, and therefore only the lath microstructure will be discussed.

The characteristics of a general lath martensite (α') microstructure are shown schematically in Fig. 1.3. The microstructure is hierarchical, with four separate scales. Prior austenite (γ) grains are the largest features. Each prior austenite grain contains a number of packets, which are groups of blocks with the same habit plane $\{111\}_\gamma$. A packet is composed of an ensemble of blocks, which are bundles of laths having approximately the same crystal orientation. It is commonly accepted that the crystallographic orientations within the blocks are related to those of the prior-austenite grains by the Kurdjumov-Sachs (K-S) orientation relationship, which is expressed as $(111)_\gamma // (110)_{\alpha'}, [101]_\gamma // [111]_{\alpha'}$ and has a total of 24 possible crystallographic variants [13, 16]. Recent work has shown sub-block morphology in martensite to be low-angle boundaries [16, 36]. Low angle boundaries do not significantly change the predictions of a continuum plasticity model and so are ignored in our model.

A model martensite microstructure is generated as follows (Fig. 2.4). (i) First, a 3D prior austenite grain structure is generated using a simulated annealing process [44] with brick meshing (Fig. 2.4(a)), where the simulated annealing process refers to the geometric optimization of space-filling objects without too much overlap. Random crystallographic orientations $[A]_{\gamma}$ composed of three orthogonal unit vectors are assigned to the prior austenite grains. (ii) Each prior austenite grain is then divided into packets by using L_{∞} Voronoi tessellation. An element is selected at random within each prior austenite grain to act as the Voronoi center [28, 29, 96] (Fig. 2.4(b)). The distance between Voronoi centers and other elements in the prior austenite grain is measured by the L_{∞} norm or maximum norm [97]. The number of Voronoi centers in each prior austenite grain controls the packet size. One of four $\{111\}_{\gamma}$ habit planes (see Table 2.1) in the K-S orientation relationship is randomly chosen for each packet [16]. (iii) Finally, each packet is sub-divided into blocks, using a similar L_{∞} Voronoi tessellation (Fig. 2.4(c)). One orientation variant selected at random from the 6 possible K-S orientation variants of each packet group (see Table 2.1) is assigned to each block. The number of Voronoi centers in each packet controls the block size. The orientations of the blocks $[A]_{\alpha'}$ are related to the orientations of prior austenite grains via the transformation $[T]=[A]_{\alpha'}[A]_{\gamma}^{-1}$, which can be derived from the 24 K-S orientation variants in Table 2.1 [98].

Since the laths in a block have very similar crystallographic orientations [13, 16], we neglect the orientation difference between laths in a single block and idealize each block as a single crystal. Thus, a block size corresponds to the smallest length scale in the

model microstructure. The primary effect of the laths is to establish a large immobile dislocation density within the block, thus generating a high resistance to plastic deformation. A phenomenological constitutive law, which includes the dislocation density as a state variable, is used to approximate the slip resistance within each block, as described in more detail in next Section.

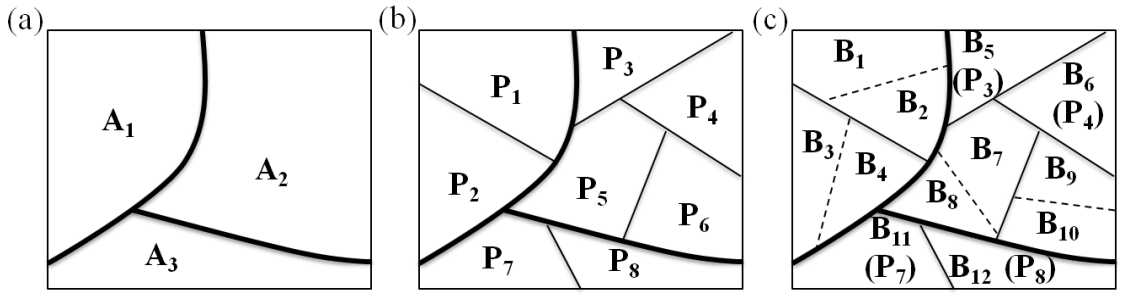

Fig. 2.4 Schematic showing the hierarchic microstructure generation procedure (a)->(b)->(c) of lath martensite in a low-carbon steel. (a) Prior austenite grains A_i are generated by a simulated annealing process [44]. Thick black lines are prior austenite grain boundaries. (b) Each prior austenite grain is divided into packets P_i using L_∞ Voronoi tessellation. Thin black lines are packet boundaries. (c) Each packet is subdivided into blocks B_i using L_∞ Voronoi tessellation. Dashed black lines are block boundaries.

Table 2.1 The 24 crystallographic variants for the K-S orientation relationship [39].

Variant	Planes parallel	Direction parallel	Packet Group
V1	$(111)_\gamma$ // $(011)_{\alpha'}$	$[\bar{1}01]_\gamma$ // $[\bar{1}\bar{1}1]_{\alpha'}$	P1
V2		$[\bar{1}01]_\gamma$ // $[\bar{1}1\bar{1}]_{\alpha'}$	
V3		$[01\bar{1}]_\gamma$ // $[\bar{1}\bar{1}1]_{\alpha'}$	
V4		$[01\bar{1}]_\gamma$ // $[\bar{1}1\bar{1}]_{\alpha'}$	
V5		$[1\bar{1}0]_\gamma$ // $[\bar{1}\bar{1}1]_{\alpha'}$	
V6		$[1\bar{1}0]_\gamma$ // $[\bar{1}1\bar{1}]_{\alpha'}$	
V7	$(1\bar{1}1)_\gamma$ // $(011)_{\alpha'}$	$[10\bar{1}]_\gamma$ // $[\bar{1}\bar{1}1]_{\alpha'}$	P2
V8		$[10\bar{1}]_\gamma$ // $[\bar{1}1\bar{1}]_{\alpha'}$	
V9		$[\bar{1}\bar{1}0]_\gamma$ // $[\bar{1}\bar{1}1]_{\alpha'}$	
V10		$[\bar{1}\bar{1}0]_\gamma$ // $[\bar{1}1\bar{1}]_{\alpha'}$	
V11		$[011]_\gamma$ // $[\bar{1}\bar{1}1]_{\alpha'}$	
V12		$[011]_\gamma$ // $[\bar{1}1\bar{1}]_{\alpha'}$	
V13	$(\bar{1}11)_\gamma$ // $(011)_{\alpha'}$	$[0\bar{1}1]_\gamma$ // $[\bar{1}\bar{1}1]_{\alpha'}$	P3
V14		$[0\bar{1}1]_\gamma$ // $[\bar{1}1\bar{1}]_{\alpha'}$	
V15		$[\bar{1}0\bar{1}]_\gamma$ // $[\bar{1}\bar{1}1]_{\alpha'}$	
V16		$[\bar{1}0\bar{1}]_\gamma$ // $[\bar{1}1\bar{1}]_{\alpha'}$	
V17		$[110]_\gamma$ // $[\bar{1}\bar{1}1]_{\alpha'}$	
V18		$[110]_\gamma$ // $[\bar{1}1\bar{1}]_{\alpha'}$	
V19	$(11\bar{1})_\gamma$ // $(011)_{\alpha'}$	$[\bar{1}10]_\gamma$ // $[\bar{1}\bar{1}1]_{\alpha'}$	P4
V20		$[\bar{1}10]_\gamma$ // $[\bar{1}1\bar{1}]_{\alpha'}$	
V21		$[0\bar{1}\bar{1}]_\gamma$ // $[\bar{1}\bar{1}1]_{\alpha'}$	
V22		$[0\bar{1}\bar{1}]_\gamma$ // $[\bar{1}1\bar{1}]_{\alpha'}$	
V23		$[101]_\gamma$ // $[\bar{1}\bar{1}1]_{\alpha'}$	
V24		$[101]_\gamma$ // $[\bar{1}1\bar{1}]_{\alpha'}$	

2.4. Dislocation-density-based crystal plasticity model

Most finite element analyses pertaining to lath martensite adopt phenomenological plasticity models [9, 17, 99]. These models do not account for the crystalline structure, anisotropy of lath martensite, orientation relations, morphologies, prior austenite orientations and initial dislocation densities. Molecular Dynamics simulations have also been used to predict the defect nucleation and transformation at the molecular level [100-102]. But the limitations of spatial scales minimize the understanding and prediction at the microstructural level. Recently, Hatem and Zikry proposed a dislocation-density-based crystal plasticity finite element model to predict the mechanical behavior of lath martensitic microstructures [28, 29, 96], where the crystalline structure, anisotropy, orientation relations, prior austenite orientations and initial dislocation densities were considered. But the 2D lath martensite microstructure only includes a single prior austenite grain and it cannot predict the overall stress-strain curves of complex lath martensitic microstructures. In this dissertation, we will follow the dislocation-density-based crystal plasticity finite element model proposed by Hatem and Zikry [28, 29, 96] with the revised dislocation density evolution law to predict the mechanical behavior of martensitic steels and the martensite phase in DP steels. The revised dislocation density evolution law was developed by Lee *et al.* [103].

Our computations model each block in the microstructure as a single crystal, using a dislocation-density-based crystal plasticity model similar to one proposed by Hatem and Zikry [28, 29, 96] and Lee *et al.* [103]. The total deformation gradient $\mathbf{F}$ is decomposed as

$$\mathbf{F} = \mathbf{F}^e \mathbf{F}^p \tag{2.1}$$

where $\mathbf{F}^e$ is the elastic deformation gradient and $\mathbf{F}^p$ is the plastic deformation gradient due to slip. The evolution of plastic deformation is described as the cumulative slip rates on all possible slip systems,

$$\mathbf{L}_p = \mathbf{F}^e \dot{\mathbf{F}}^p \mathbf{F}^{p-1} \mathbf{F}^{e-1} = \sum_\alpha \dot{\gamma}^\alpha \mathbf{s}^{*\alpha} \otimes \mathbf{m}^{*\alpha} \tag{2.2}$$

where $\mathbf{L}_p$ is the plastic deformation velocity gradient, $\dot{\gamma}^\alpha$ is the slip rate of slip system α, $\mathbf{s}^{*\alpha}$ and $\mathbf{m}^{*\alpha}$ are the slip direction vector and slip plane normal vector in the deformed configuration, respectively.

The slip systems in BCT lath martensite are assumed to be the same as those of a BCC crystal [104]. Within each block, plastic flow is assumed to take place by shearing on the 24 {110} <111> and {112} <111> systems, with the plastic slip rate on a generic slip system related to the stress acting on the slip plane by

$$\dot{\gamma}^\alpha = \dot{\gamma}_0 \left(\frac{\left| \tau^\alpha \right|}{g^\alpha} \right)^m sign(\tau^\alpha) \tag{2.3}$$

Here, τ^α is the resolved shear stress on slip system α, $\dot{\gamma}_0, m$ are material parameters, and the strength of each slip system g^α is determined from dislocation densities on each slip system according to

$$g^\alpha = Gb \sqrt{\sum_{\beta=1}^{N} a_{\alpha\beta} \rho^\beta} \tag{2.4}$$

where $a_{\alpha\beta} = \mathbf{m}^\alpha \cdot \xi^\beta$, and ξ^β is the line direction of the forest dislocations. The dislocation densities evolve according to [103]

$$\frac{d\rho^\alpha}{dt} = \left| \dot{\gamma}^\alpha \right| \left[\frac{1}{b\, k_a} \sqrt{\sum\nolimits_\beta^n \rho^\beta} - \frac{k_b}{b} \rho^\alpha \right] \tag{2.5}$$

where k_a, k_b are material parameters, and b is the Burgers vector. The dislocation-density-based crystal plasticity model has five material parameters (including the initial dislocation density, taken to be equal on all slip systems), which must be determined from experiments (see Sections 2.6 and 2.7).

2.5. Implementation of dislocation-density-based crystal plasticity model

The dislocation-density-based crystal plasticity model was implemented as user-material subroutine (UMAT) in the commercial finite element code ABAQUS v6.9. The tangent modulus method [105] for rate-dependent crystal plasticity models was used to update the slip rate, strength of slip, resolved shear stresses, and dislocation density of each slip system in the UMAT.

Fig. 2.5 shows the implementation flowchart of the dislocation-density-based crystal plasticity model in the UMAT. The framework of the UMAT is based on Kysar's single crystal plasticity UMAT [106] that was originally developed by Prof. Y.G. Huang at Harvard University.

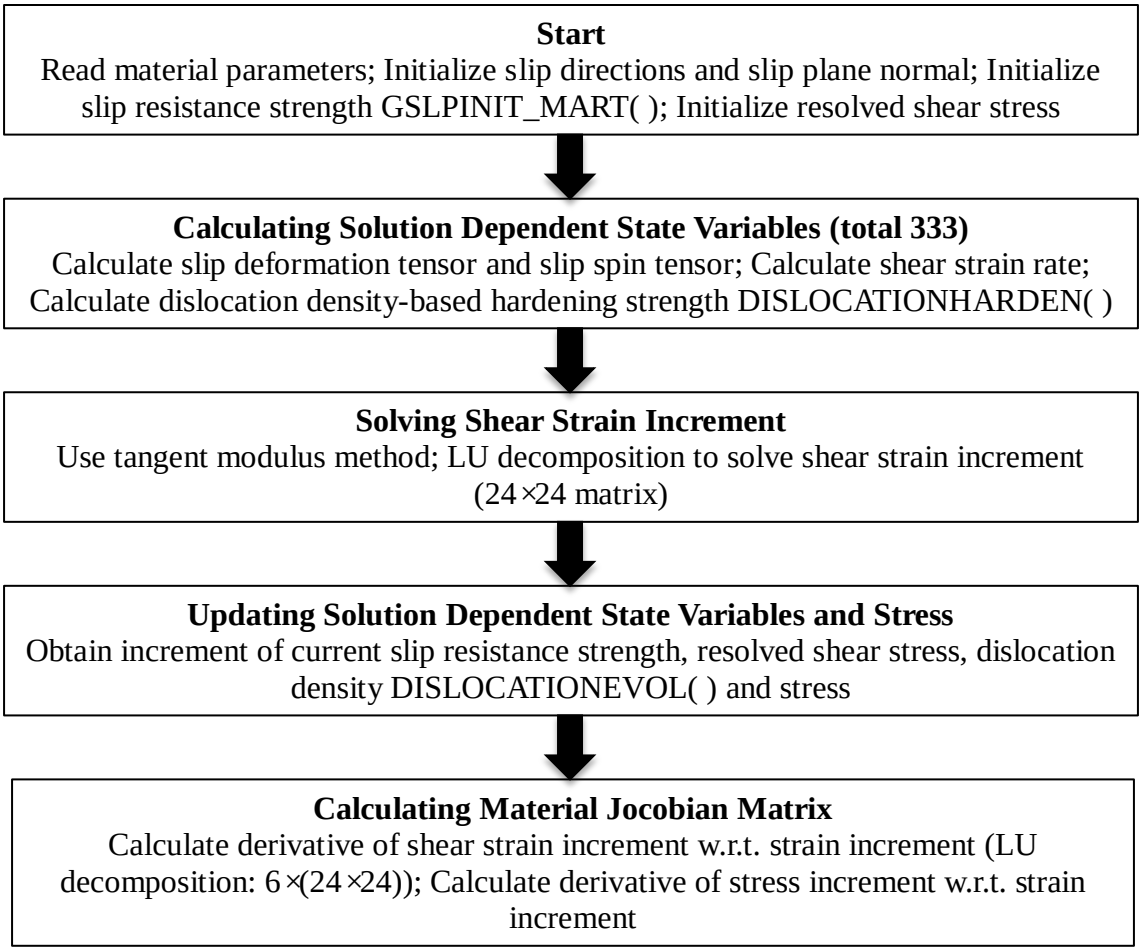

Fig. 2.5 Implementation flowchart of dislocation-density-based crystal plasticity model for martensite

Three new subroutines, GSLPINIT_MART( ), DISLOCATIONHARDEN( ) and DISLOCATIONEVOL( ) were added into Kysar's UMAT. The three new subroutines are detailed in the Appendix A.

Subroutine GSLPINIT_MART( ) is used to calculate the initial value of the current slip resistance strength of each slip system. First, the edge dislocation line direction ξ^{α} is calculated by the cross product of the slip direction $\mathbf{s}^{\alpha}$ and the slip plane normal $\mathbf{m}^{\alpha}$. The initial value of the current slip resistance strength of each slip system is determined based on Eq. (2.4).

Subroutine DISLOCATIONHARDEN( ) is used to calculate the slip hardening moduli. The rate form of Eq. (2.4) gives

$$\dot{g}^{\alpha} = \frac{G}{2\sqrt{\sum_{\beta=1}^{N} a_{\alpha\beta}\rho^{\beta}}} \sum_{\beta=1}^{N} a_{\alpha\beta} \left(\frac{1}{k_a} \sqrt{\sum_{i=1}^{N} \rho^{i}} - k_b \rho^{\beta} \right) \left| \dot{\gamma}^{\beta} \right| \tag{2.6}$$

Then, the self- and latent- hardening moduli are given by

$$h_{\alpha\beta} = \frac{G}{2\sqrt{\sum_{i=1}^{N} a_{\alpha i}\rho^{i}}} a_{\alpha\beta} \left(\frac{1}{k_a} \sqrt{\sum_{i=1}^{N} \rho^{i}} - k_b \rho^{\beta} \right) \tag{2.7}$$

Subroutine DISLOCATIONEVOL( ) is used to calculate the increment of dislocation density based on Eq. (2.5), that is,

$$\Delta\rho^{\alpha} = \frac{\left|\Delta\gamma^{\alpha}\right|}{b} \left[\frac{1}{k_a} \sqrt{\sum_{\beta}^{n} \rho^{\beta}} - k_b \rho^{\alpha} \right] \tag{2.8}$$

2.6. Determining lath martensite material parameters in MS steels

Material parameters for the martensite in MS steels are determined by fitting finite element simulations to the results of experimental micropillar compression tests in Section 2.2. Experimental data for micropillars 2 (which consists of a single block) and 4 (which includes block boundaries) in Section 2.2 in fully martensitic steel were used for fitting purposes [15]. An inhomogeneous state of stress and strain is developed in a micropillar during the compression test. Therefore, full-scale 3D finite element simulations are needed to model the deformation. A 3D microstructure is generated in the model micropillar following the procedure in Section 2.3, except that the micropillar was assumed to be a single prior austenite grain.

The boundary conditions applied in the 3D micropillar simulations are as follows. The top surface of the micropillar is indented by a flat rigid surface representing the flat punch nanoindenter; the base is supported on springs, which approximate the elastic deformation of the underlying material. To model the real interaction between the nanoindenter and the micropillars, the friction between the rigid surface and micropillars is also considered in the 3D micropillar model. The friction coefficient is set to be 0.5 in all the following micropillar simulations. The friction coefficient value was selected so as to prevent slip between the indenter and pillar surface. For friction coefficient values that allow slip, the predicted deformation in the pillars does not match experiments. As long as the friction coefficient is sufficiently high to prevent slip, predictions are insensitive to the value selected.

The crystallographic orientations of the experimental micropillars are not known. Consequently, a random orientation was assigned to the prior austenite grain in the simulations, and the orientation that best fits the experimental data was selected. It was found that the prior austenite grain with $[011]_\gamma$ along the micropillar axial direction could reproduce the experimental results. In the following 3D micropillar simulations, we always adopt $[011]_\gamma$ as the axial direction of the prior austenite grain.

An iterative optimization procedure (illustrated in Fig. 2.6) was used to determine material parameters in the crystal plasticity model that best fit experimental stress-strain curves from the micropillar experiments. The mean-square average of the difference between measured and predicted nominal stress was used for the objective function Φ, which was minimized by the Nelder-Mead Simplex algorithm [107]. Predictions are fit simultaneously to compression data for micropillars containing only a single block (e.g.

micropillar 2), and for those containing multiple blocks (e.g. micropillar 4). Single-block micropillars deform primarily in single slip, and their response is therefore dominated by the slip resistance of an individual slip system. In contrast, micropillars containing multiple blocks deform with multiple active slip systems. The data for micropillars containing multiple slip therefore provide a robust calibration for latent hardening parameters in the crystal plasticity model. The material parameters that best fit micropillar data are listed in Table 2.2. These parameters should not be interpreted as universal to all martensitic steels, of course: considerable variability in properties is likely to arise from chemistry (carbon and alloy content) and processing history (reflected in lath dimensions, and dislocation density).

The predicted nominal stress versus nominal strain curves for two micropillars are compared to experimental measurements in Fig. 2.7. Micropillar 2, which contains a single block, displays approximately elastic-perfectly plastic behavior, characterized by a flat flow stress curve (no hardening) after elastic deformation. In contrast, micropillar 4 (which contains two blocks separated by a packet boundary in the simulation) shows significant strain hardening. K-S variants V9 and V21 were chosen for the two blocks in micropillar 4 (see Fig. 2.8). Our simulation results provide additional support for the hypothesis that block or packet boundaries give rise to the strain hardening behavior observed experimentally in the two largest micropillars. In addition, the crystal plasticity model yields an excellent fit to experimentally measured stress-strain curves. A power-law fit ($\sigma=k\varepsilon^{n}$) to the simulated stress-strain curve for micropillar 4 provides an exponent of 0.075 which is in reasonable agreement with that obtained from experiment on the bulk material (n=0.101).

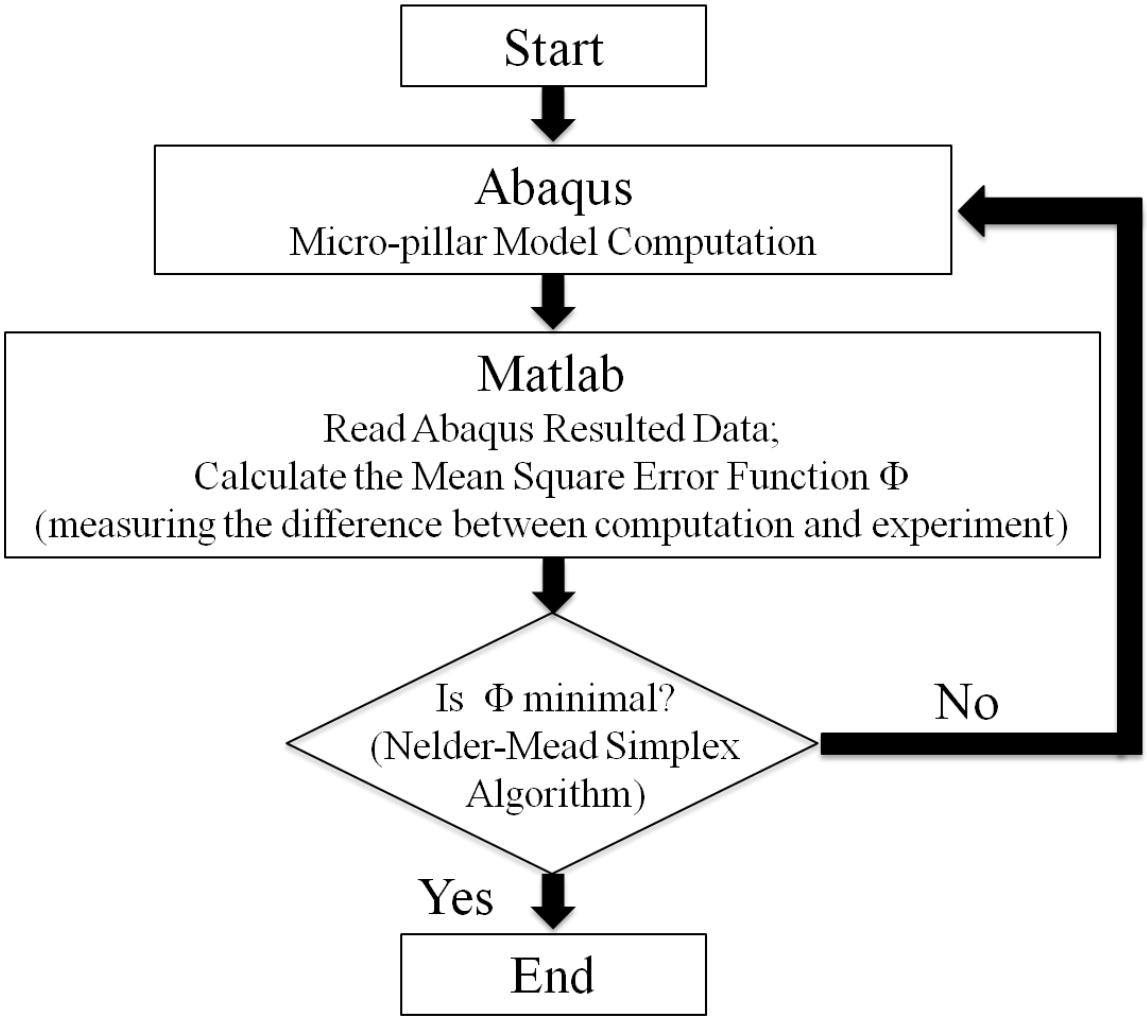

Fig. 2.6 Iterative procedure used to determine material parameters for lath martensitic steels.

Table 2.2 Material parameters obtained from 3D finite element simulations of micropillar compression tests on the martensitic phase of three AHSS.

	Fully Martensitic Steel	DP Steel DF140T	DP Steel DP980
Strain rate $\dot{\gamma}_0$ (s^{-1})	1.72×10^{-3}	1.6×10^{-3}	1.7×10^{-3}
Stress exponent m	69.1	63.7	71.2
Shear modulus G (GPa)	75	75	75
Burgers vector b (nm)	0.3	0.3	0.3
Dislocation nucleation rate k_a	71.2	86.4	73.0
Dislocation annihilation rate k_b	0.152	0.0935	0.14
Initial dislocation density ρ_0 (m^{-2})	5.02×10^{13}	8.2×10^{13}	3.0×10^{13}

Fig. 2.8 shows predicted contours of Von Mises stress and equivalent plastic strain in micropillars 2 and 4, respectively (corresponding to 5% strain in Fig. 2.7). SEM images of the micropillars after deformation are also shown for comparison. The predicted slip distribution in both micropillars is in good qualitative agreement with the deformed shapes observed experimentally. Micropillar 2 deforms primarily by slip on a dominant active slip system with a fairly localized deformation mode. In contrast, multiple slip systems are activated in micropillar 4, which consequently exhibits a more diffuse strain field.

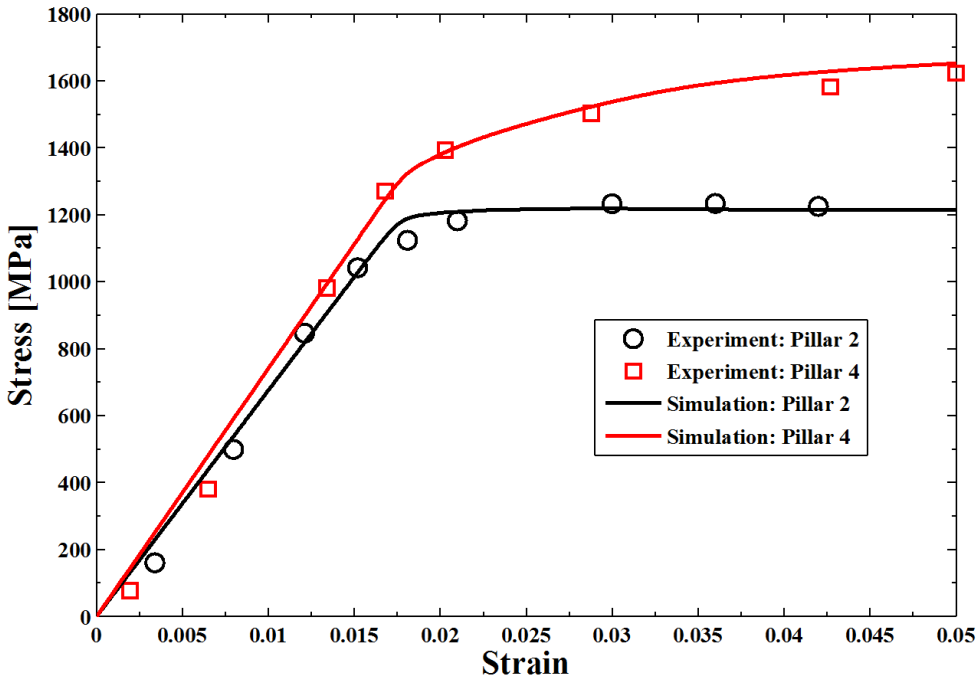

Fig. 2.7 Comparison of measured and predicted stress-strain curves for micropillars extracted from the lath martensitic steel. Micropillar 2 is idealized as a single martensitic block, and exhibits nearly elastic-perfectly plastic behavior. Micropillar 4 in the simulation contains two blocks separated by a packet boundary, and the interaction between them leads to an effective strain hardening behavior. Experimental data are shown in Fig. 2.1(a).

Since it is not possible to experimentally determine the exact microstructure in those micropillars that contain multiple blocks, we have tested the sensitivity of our predictions to the pillar microstructure. For this purpose, we used the material parameters listed in Table 2.2, and varied the number of blocks and packets in the pillar. It was found that the most significant microstructural variable was the misorientation between the two blocks in the pillar. For example, Fig. 2.9 shows predicted stress–strain curves for a pillar containing two types of interface. In one case, the blocks in the pillar have orientations corresponding to K-S variants V9 and V21, and are therefore separated by a packet boundary. This microstructure gives rise to a strong geometric constraint at the interface, and hence results in high strain hardening. The second example shows results for a pillar containing blocks with K-S variants V9 and V7, which are separated by a block boundary. In this case, the geometric constraint at the interface is weaker, and so produces a lower strain hardening slope. It is important to understand the physical origin of the predicted strengthening effect of packet and block boundaries. The role of the interface is to change the deformation mode from single slip (in a pillar consisting of a single block) to multiple slip (in pillars consisting of multiple packets or blocks). This activates latent hardening, which is the dominant contribution to the increased flow strength of the pillar. The difference between block boundaries and packet boundaries is a consequence of the different slip behavior in the material adjacent to these boundaries.

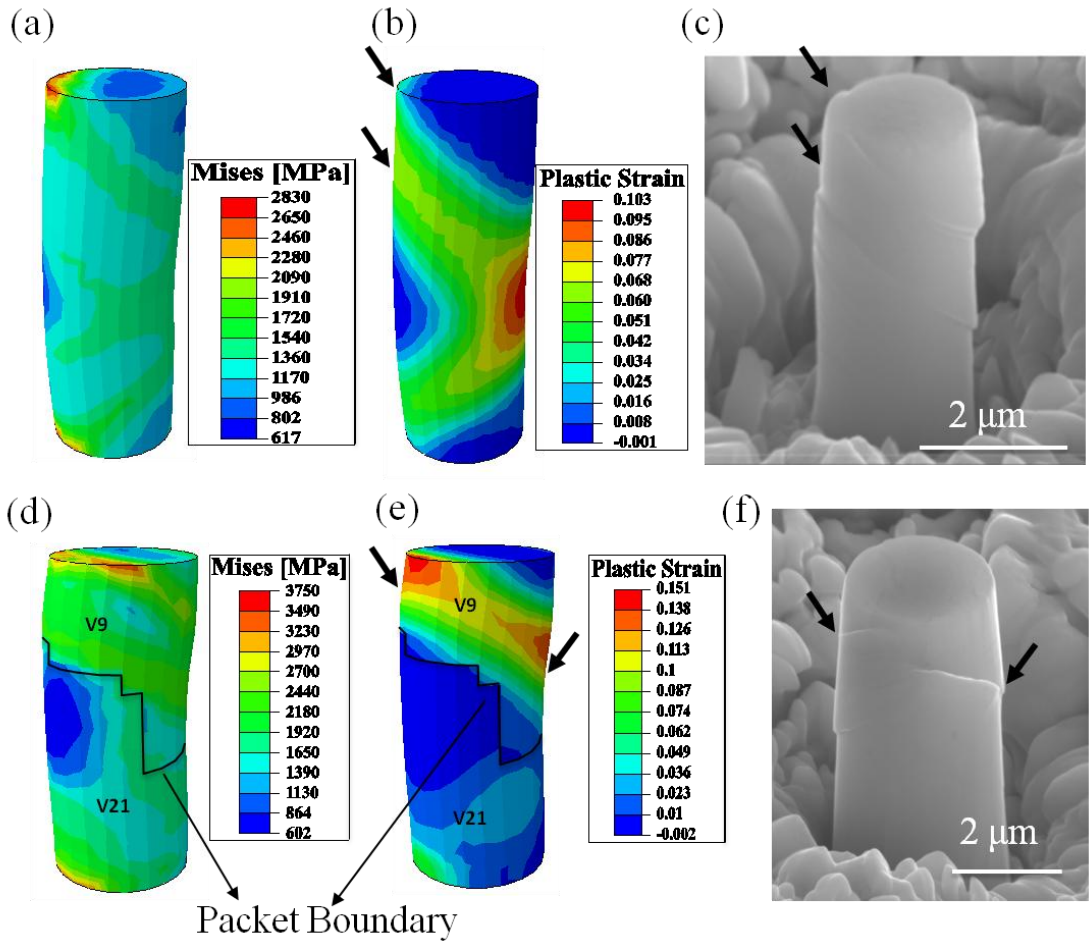

Fig. 2.8 3D Finite element simulations of micropillar indentation experiments. (a) Von Mises stress and (b) equivalent plastic strain contours of deformed micropillar 2 at 5% strain. (c) SEM image of the deformed micropillar 2 for comparison with (a) and (b). (d) Von Mises stress and (e) equivalent plastic strain contours of deformed micropillar 4 at 5% strain. (f) SEM image of the deformed micropillar 4 for comparison with (d) and (e). Black lines in contours (d) and (e) are the packet boundary. Experimental data appear in [15].

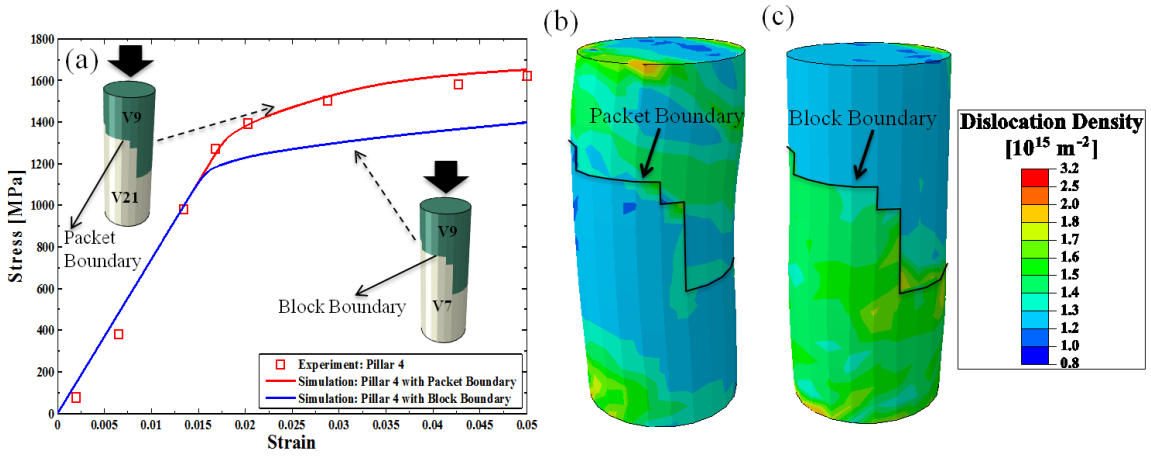

Fig. 2.9 Comparison of strain hardening behavior of micropillars with packet boundary and with block boundary. (a) Stress-strain curves of two micropillars and (b,c) dislocation density contours of micropillars with (b) packet boundary and with (c) block boundary. Black lines in contours (b) and (c) are the packet boundary and the block boundary, respectively. Experimental data appear in [15].

2.7. Determining lath martensite material parameters in DP steels

Similar to the determination of martensite material parameters in MS steels in the previous section, we will determine the martensite material parameters in DP steels DF140T and DP980 in this section. We assume that micropillars that exhibit little strain hardening (pillar 2 in DF140T and pillar A in DP980 in Fig. 2.10) consist of a single martensite block while those that show significant strain hardening (pillar 1 in DF140T and pillar B in DP980 in Fig. 2.10) consist of multiple bocks [43]. Parameters for martensite in DP steels were fit to pillars with elastic-perfectly plastic response (which were taken to be a single martensite block) and those with a hardening response (which contained a packet boundary). The resulting material parameters are listed in Table 2.2.

Fig. 2.10 compares the measured and predicted stress-strain curves for martensitic micropillars in both DP steels. The results are qualitatively similar to previous experiments and simulations of deformation in micropillars extracted from fully

martensitic steels in Section 2.6. With an appropriate set of parameters, the model accurately predicts both the elastic-perfectly plastic response of pillars consisting of a single block, as well as the hardening behavior of pillars that contain a block or packet boundary. Interestingly, the optimal set of parameters representing the two DP steels indicates that the largest difference between them is the initial dislocation density ($8.2\times10^{13}m^{-2}$ for DF140T and $3.0\times10^{13}m^{-2}$ for DP980). DF140T has a higher initial dislocation density, and consequently has greater flow strength than DP980. These observations are consistent with differences in partitioned carbon content between the martensite phases of the two steels (~0.35 wt.% in martensite phase of DF140T versus ~0.15 wt.% in martensite phase of DP980), since the dislocation density increases with carbon content in low-carbon steels [65, 108].

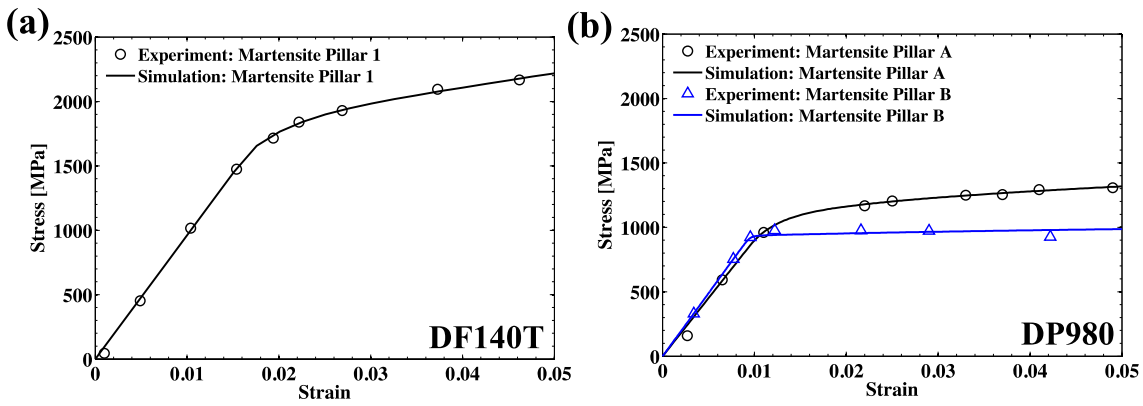

Fig. 2.10 Comparison of measured and predicted stress-strain curves for martensitic micropillars extracted from DP steels (a) DF140T and (b) DP980. Micropillar 1 of DF140T and micropillar A of DP980 in the simulations contain several blocks separated by packet boundaries, and the interaction between them leads to an effective strain hardening behavior. Micropillar 2 of DP980 is idealized as a single martensitic block, and exhibits elastic-nearly perfectly plastic behavior. Experimental data appear in [43].

2.8. Comparison of measured and predicted behavior for MS steels

The numerical simulation can be validated by predicting the uniaxial tensile stress-strain response of a full 3D RVE of the martensite, and comparing the predictions to experimental measurements in Fig. 1.5 [15]. For this purpose, a three-dimensional RVE (Fig. 2.11(a)) was constructed using the method described in Section 2.3. A typical distribution of blocks in a representative volume element is shown in Fig. 2.11(a). The volume element was then subjected to periodic boundary conditions representing uniaxial tension along the x-direction, and the average stress in the volume element is computed. Note that the boundary conditions preclude necking in the volume element, so results were only computed for strains up to 4% to rule out any possible effects of necking.

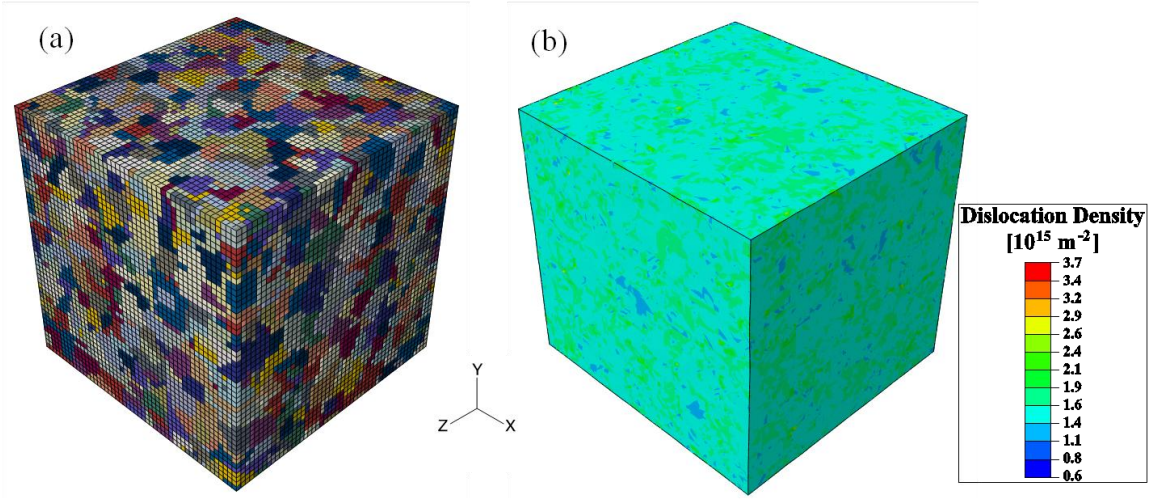

Fig. 2.11 (a) One example of 3D RVEs and (b) dislocation density contour of the RVE at 4% macroscopic strain. Blocks are distinguished by colors (a). The size of RVE is 100μm x 100μm x 100μm and the brick element size is 2μm x 2μm x 2μm. Total 125,000 elements are used.

A qualitative validation of the model is provided by the predicted dislocation density distribution shown in Fig. 2.11(b). The dislocation density contour (Fig. 2.11(b)) shows that its value is around $10^{15} m^{-2}$ which is close to the experimental observation [65, 108], note that the experimental data was measured before plastic deformation. In addition, Fig. 2.12 compares the measured and predicted uniaxial tensile stress-strain curves for three RVEs with random microstructures. The model slightly overestimates the initial yield stress of the material. This discrepancy may be a consequence of tension-compression asymmetry in the martensite resulting from non-Schmid behavior of slip [75, 76, 78]. Nevertheless, the good agreement between theory and experiment validates the microstructure-based procedure for predicting macroscopic properties of steels. In particular, the model correctly predicts the strain hardening behavior of the bulk material, even though individual martensite blocks in single slip exhibit nearly elastic-perfectly plastic behavior. The hardening response of the bulk material is a consequence of geometric constraints between martensite blocks, packets, and grains, which result in multiple slip and activate latent hardening. The hardening rate of the bulk specimen is comparable to that of a pillar containing a packet boundary, suggesting that a similar level of geometric constraint develops in these two types of specimen. Simulations suggest that the overall response of the bulk material is less sensitive than a micropillar to its detailed microstructure, since different representations of statistically similar microstructural RVEs are predicted to have nearly identical flow stresses.

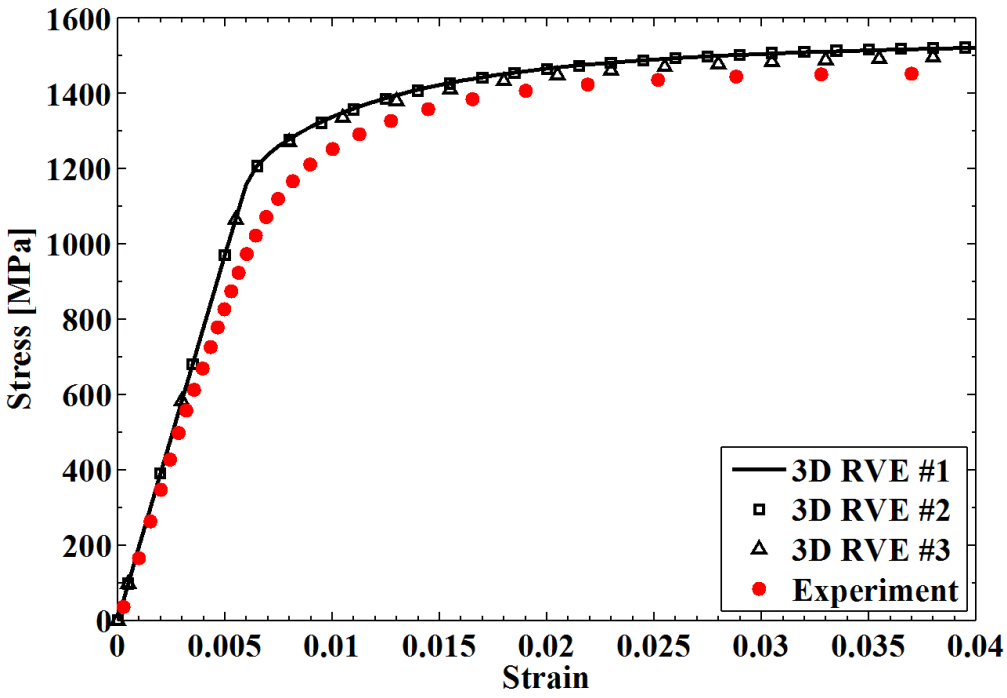

Fig. 2.12 Comparison of measured and predicted uniaxial stress-strain curves of lath martensitic steel. Three RVEs with random microstructures show almost the same flow and hardening behaviors, and in good agreement with experiments. Experimental data appear in Fig. 1.5.

We have also calculated quantitative measures of the stress distribution on the prior austenite/packet/block boundaries. The normal and tangential stresses on the prior austenite/packet/block boundaries in the fully martensitic steel were estimated. This calculation is complicated by the rectangular grid used to mesh the microstructures in our computations, and the boundaries follow a zig-zag path along element boundaries rather than conforming to the true geometry of the boundaries. We have therefore used the following procedure to compute the normal and tangential stress along the boundaries. First, we choose a small cube of material with the point of interest on the boundary at the center. An average normal vector **n** to the boundary within the cube is created using the following definition,

$$\mathbf{n} = \frac{1}{Total\ no.\ of\ boundaries} \sum_{boundaries} \mathbf{n}^{boundary} \tag{2.9}$$

Two mutually perpendicular tangent vectors $\mathbf{t}^1$, $\mathbf{t}^2$ that are perpendicular to $\mathbf{n}$ are created randomly. Then the normal and tangent stresses T_n, T_t are calculated by the following formulas,

$$T_n = \frac{1}{V_{cube}} \int_{V_{cube}} n_i \sigma_{ij} n_j; \quad T_t = \sqrt{T_1^2 + T_1^2}; \quad T_\alpha = \frac{1}{V_{cube}} \int_{V_{cube}} t_i^\alpha \sigma_{ij} n_j \quad (\alpha = 1,2) \tag{2.10}$$

where the volume integrals are computed by summing over elements in the cube. This procedure has been used to compute histograms of the variation of normal and tangential stresses on the prior austenite/packet/block boundaries in fully martensitic steel. The results are shown in Fig. 2.13. The total areas of the histograms are normalized to unity, and are shown at the same global strain (4%). The results show that the normal and tangential stresses acting on packet and block boundaries are similar, while the average normal and tangential stresses acting on prior austenite boundaries are slightly smaller than those on packet/block boundaries. The slight difference between prior austentine and packet/block boundaries might be explained by the uncorrelated crystal orientations between prior austenite grains and the correlated K-S orientations between packets or blocks.

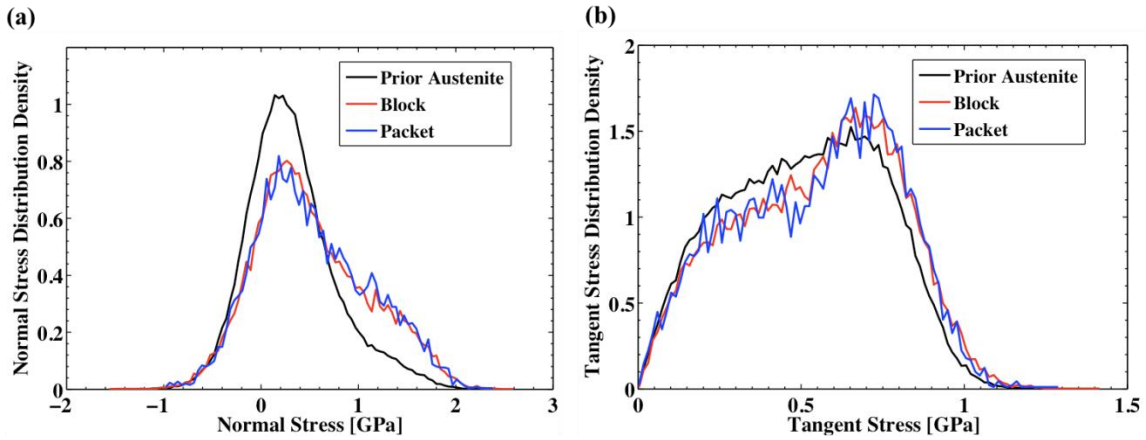

Fig. 2.13 Histograms of (a) normal and (b) tangential stress distributions on the prior austenite/packet/block boundaries in fully martensitic steel at 4% global strain.

Chapter 3. Mechanical Behavior of Ferrite Phase in AHSS

Similar to the previous Chapter where the material properties of lath martensites in AHSS were determined via fitting the micropillar compression stress-strain curves, in this Chapter, the material properties of ferrite phase in DP steels will be determined. In contrast to the hierarchical microstructure of lath martensite, the ferrite grains in DP steels are assumed to be single crystals. After a brief overview of the ferrite phase in DP steels in Section 3.1, the material properties of the ferrite phase in DP steels will be determined in Section 3.3 using the orientation dependent stress-strain curves of ferrite micropillar compression tests in Section 3.2. The crystallographic orientation dependent flow curves and non-Schmid behavior of ferrite phase in DP steels will be highlighted in this Chapter.

3.1. Overview of ferrite phase of AHSS

As mentioned in the Chapter 1, AHSS are multiphase steels which consist of hard islands in a ductile ferritic matrix, and conventional HSS are also ferrite-based steels. The ductile and soft ferrite phase, compared to other phases in AHSS, is the major base material in all high strength steels. The mechanical behavior of the ferrite phase becomes important in order to understand the overall mechanical behavior of AHSS and other steels.

The mechanical behavior of ferrite (also known as α-ferrite or alpha iron) in steels has been discussed several decades ago [109]. The general properties of ferrite in steels have been reviewed in Leslie's book [109], such as yielding, plastic flow, hardening and deformation texture. The strength of the ferrite phase in DP steels is mainly controlled by the steel chemistry, grain size and initial dislocation density [8]. Except for the general properties of BCC ferrite grains, recently, some new features have been observed in ferrite grains in AHSS [37, 48], especially the inhomogeneous hardness in a single ferrite grain near the ferrite/martensite boundaries.

Generally, the ferrite grains in polycrystals are assumed to be similar to ferrite single crystals. But in AHSS, the ferrite grains are always surrounded by the harder phases, like martensite in DP steels and the mechanical behavior of ferrite grains in such heterogeneous microstructures is different from those in homogeneous microstructures [37, 48]. Recently, Tsipouridis *et al.* observed that the hardness of ferrite in DP steels increases as the indent approaches Ferrite/Ferrite grain boundaries and/or Ferrite/Martensite phase boundaries using ultramicrohardness indentation tests [37]. They also observed that the amount of hardness increase depends on the boundary types: indents located close to phase boundaries exhibit higher hardness values than indents located at equal distances from grain boundaries [37]. The similar hardness variation trend in the ferrite phase was also observed in nanoindentation tests of DP steel [48]. The grain- and phase-boundaries as dislocation obstacles have been used to interpret the hardness variation inside the ferrite phase of DP steels, since higher dislocation densities in the ferrite in the vicinity of the phase boundaries were observed [37, 48]. The higher

dislocation densities near the phase boundaries were induced from the austenite-to-martensite transformation on the adjacent ferrite grains [37].

Although the inhomogeneous hardness were observed in ferrite grains near the harder phase in AHSS using hardness indentation tests, the plastic flow and hardening properties cannot be directly measured from hardness indentation tests. In addition, the presence of a harder substrate underneath the indent, irrespective as to whether this is a martensite grain or just a ferrite grain boundary, is an unpredictable factor and may affect the measurements in hardness indentation tests [37]. The micropillar compression tests described in the preceding chapter provide a more reliable measure of mechanical behavior in ferrite. Stewart *et al.* have used the micropillar compression technique to measure the constitutive stress-strain behavior of the ferrite phase in DP steel [42]. The yield and fracture strengths of the ferrite phase in DP steel have also been determined in micropillar compression tests [42]. However the crystallographic orientation dependent behavior of the ferrite phase in DP steels was ignored in Stewart *et al.*'s work, which will be demonstrated to be important in extracting flow and hardening parameters of ferrite in this Chapter.

Another important feature of the ferritic phase in AHSS is the non-Schmid behavior. The physical mechanism of the non-Schmid behavior in ferrite is that the stress may modify the non-planar dislocation core structure and the flow stress consequently depends on the full stress tensor [45, 110-112]. It is based on the evidence that plastic deformation of BCC ferrite is dominated by the glide of screw dislocations, which have a highly non-planar core structure and a high Peierls barrier to dislocation motion [45, 110-115]. This will be discussed in the Section 3.2 in more detail. In light of these

developments, we will use the non-Schmid Bassani-Wu crystal plasticity model to extract the material properties of the ferrite phase in DP steels in this Chapter.

3.2. Experimental data of ferrite micropillar compression tests

All of the experiments in this Section were conducted by Dr. H. Ghassemi-Armaki at Brown University [43]. The nominal stress-strain curves for ferrite micropillars extracted from both DP steels are shown in Fig. 3.1. The orientation of the compression axis in each specimen is listed in Table 3.1. The yield stress is orientation dependent, but lies in the general range between 300-400 MPa for both DP steels. This range is comparable to the initial uniaxial tensile yield stress in the DP steels (see Fig. 1.5). The stress-strain curves can be used to determine material parameters such as the critical resolved shear stress to activate slip, as well as self- and latent-hardening rates for the slip systems. These are described in more detail in the following Sections.

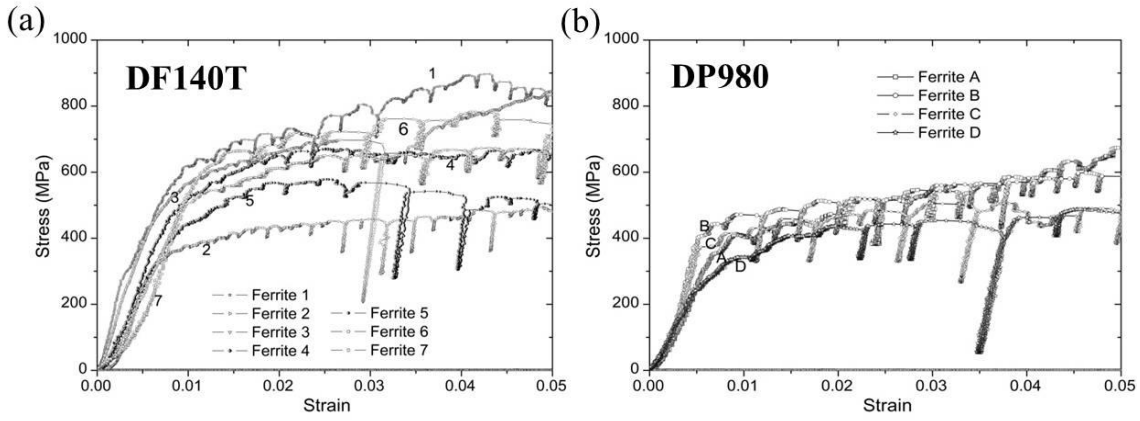

Fig. 3.1 Micropillar compression stress-strain curves for ferrite phases in (a) DF140T steel and (b) DP980 steel. The figures were provided by Dr. H. Ghassemi-Armaki at Brown University [43].

Table 3.1 The specific crystal orientations indices parallel to axis of uniaxial compression for ferrite grains of two DP DF140T and DP980 steels are as follows. The table was provided by Dr. H. Ghassemi-Armaki at Brown University [43].

DF140T	Ferrite 1: [778]	Ferrite 2: [315]	Ferrite 3: [001]	Ferrite 4: [223]	Ferrite 5: [334]	Ferrite 6: [556]	Ferrite 7: [546]
DP980	Ferrite A: [516]	Ferrite B: [324]	Ferrite C: [205]	Ferrite D: [326]	---	---	---

3.3. Non-Schmid Bassani-Wu crystal plasticity model

The ferritic phase in AHSS has a BCC crystal structure. Plastic deformation of BCC metals is dominated by the glide of screw dislocations, which have a highly non-planar core structure and a high Peierls barrier to dislocation motion [45, 110-115]. In FCC metals, yield is determined by the maximum resolved shear stress on the candidate slip systems, and the plastic flow consequently obeys Schmid's law. In contrast, for BCC materials the stress may modify the non-planar dislocation core structure, and the flow stress consequently depends on the full stress tensor [45, 110-112]. This is often referred to as 'non-Schmid' behavior. Significant progress has been made in recent years in modeling slip in BCC materials both at the atomic scale and at continuum length scales. For example, Koester *et al.* confirmed that the non-glide stresses have a strong influence on the hardening behavior of BCC iron using an atomistically informed crystal plasticity model [45, 110, 111]. In a polycrystal, this non-Schmid behavior leads to non-associated flow, which is well known to make the material prone to strain localization [45]. In light of these developments, we have chosen to model the ferrite using a constitutive model developed by [112], which is capable of accounting for non-Schmid behavior in BCC crystals.

Similar to the dislocation-density-based crystal plasticity model for martensite blocks in Section 2.4, the total deformation gradient $\mathbf{F}$ is decomposed as Eq. (2.1). The evolution of the plastic deformation is described as Eq. (2.2). Following Caillard [113], we assume that plastic flow takes place by shearing on the set of {110}<111> slip systems, with the plastic slip rate on a generic slip system related to the stress acting on the slip plane by

$$\dot{\gamma}^{\alpha} = \dot{\gamma}_0 \left(\frac{\left| \tau^{\alpha} \right|}{g_*^{\alpha}} \right)^m sign\left(\tau^{\alpha} \right) \tag{3.1}$$

Here, τ^{α} is the resolved shear stress on slip system α, $\dot{\gamma}_0, m$ are material parameters, and g_*^{α} is a modified slip system strength given by $g_*^{\alpha} = \max(g^{\alpha} - g_{NS}^{\alpha}, 0)$, where g^{α} is an evolving strength representing the effects of self- and forest- hardening; and

$$g_{NS}^{\alpha} = a_1 \mathbf{m}_1^{\alpha} \cdot \boldsymbol{\sigma} \mathbf{s}^{\alpha} + a_2 \mathbf{m}^{\alpha} \cdot \boldsymbol{\sigma}(\mathbf{m}^{\alpha} \times \mathbf{s}^{\alpha}) + a_3 \mathbf{m}_1^{\alpha} \cdot \boldsymbol{\sigma}(\mathbf{m}_1^{\alpha} \times \mathbf{s}^{\alpha}) \tag{3.2}$$

is a correction to account for non-Schmid behavior [112]. In Eq. (3.2), σ is the stress tensor; $\mathbf{s}^{\alpha}$ is the slip direction; $\mathbf{m}^{\alpha}$ is the normal to the slip plane, and $\mathbf{m}_1^{\alpha}$ is a unit vector perpendicular to the {110} plane in the zone of $\mathbf{m}^{\alpha}$ that makes an angle of -60^0 with the reference plane (see Table 3.2), and (a_1, a_2, a_3) are material parameters. Note that more recently Koester *et al.* [111] added three more terms in Eq. (3.2) to account for the non-Schmid effect of pure BCC iron. Here Eq. (3.2) can be regarded as the simple version in reference [111] by ignoring the extra three terms. The relevant unit vectors for each slip system in a BCC crystal are given in Table 3.2 [110].

Table 3.2 The 24 slip systems in BCC crystals [110].

α	Reference system	$\mathbf{s}^{\alpha}$	$\mathbf{m}^{\alpha}$	$\mathbf{m}_1^{\alpha}$
1	$(01\bar{1})[111]$	$[111]$	$[01\bar{1}]$	$[\bar{1}10]$
2	$(\bar{1}01)[111]$	$[111]$	$[\bar{1}01]$	$[0\bar{1}1]$
3	$(1\bar{1}0)[111]$	$[111]$	$[1\bar{1}0]$	$[10\bar{1}]$
4	$(\bar{1}0\bar{1})[\bar{1}11]$	$[\bar{1}11]$	$[\bar{1}0\bar{1}]$	$[\bar{1}\bar{1}0]$
5	$(0\bar{1}1)[\bar{1}11]$	$[\bar{1}11]$	$[0\bar{1}1]$	$[101]$
6	$(110)[\bar{1}11]$	$[\bar{1}11]$	$[110]$	$[01\bar{1}]$
7	$(0\bar{1}\bar{1})[\bar{1}\bar{1}1]$	$[\bar{1}\bar{1}1]$	$[0\bar{1}\bar{1}]$	$[1\bar{1}0]$
8	$(101)[\bar{1}\bar{1}1]$	$[\bar{1}\bar{1}1]$	$[101]$	$[011]$
9	$(\bar{1}10)[\bar{1}\bar{1}1]$	$[\bar{1}\bar{1}1]$	$[\bar{1}10]$	$[\bar{1}0\bar{1}]$
10	$(10\bar{1})[1\bar{1}1]$	$[1\bar{1}1]$	$[10\bar{1}]$	$[110]$
11	$(011)[1\bar{1}1]$	$[1\bar{1}1]$	$[011]$	$[\bar{1}01]$
12	$(\bar{1}\bar{1}0)[1\bar{1}1]$	$[1\bar{1}1]$	$[\bar{1}\bar{1}0]$	$[0\bar{1}\bar{1}]$
13	$(01\bar{1})[\bar{1}\bar{1}\bar{1}]$	$[\bar{1}\bar{1}\bar{1}]$	$[01\bar{1}]$	$[10\bar{1}]$
14	$(\bar{1}01)[\bar{1}\bar{1}\bar{1}]$	$[\bar{1}\bar{1}\bar{1}]$	$[\bar{1}01]$	$[\bar{1}10]$
15	$(1\bar{1}0)[\bar{1}\bar{1}\bar{1}]$	$[\bar{1}\bar{1}\bar{1}]$	$[1\bar{1}0]$	$[0\bar{1}1]$
16	$(\bar{1}0\bar{1})[1\bar{1}\bar{1}]$	$[1\bar{1}\bar{1}]$	$[\bar{1}0\bar{1}]$	$[01\bar{1}]$
17	$(0\bar{1}1)[1\bar{1}\bar{1}]$	$[1\bar{1}\bar{1}]$	$[0\bar{1}1]$	$[\bar{1}\bar{1}0]$
18	$(110)[1\bar{1}\bar{1}]$	$[1\bar{1}\bar{1}]$	$[110]$	$[101]$
19	$(0\bar{1}\bar{1})[11\bar{1}]$	$[11\bar{1}]$	$[0\bar{1}\bar{1}]$	$[\bar{1}0\bar{1}]$
20	$(101)[11\bar{1}]$	$[11\bar{1}]$	$[101]$	$[1\bar{1}0]$
21	$(\bar{1}10)[11\bar{1}]$	$[11\bar{1}]$	$[\bar{1}10]$	$[011]$
22	$(10\bar{1})[\bar{1}1\bar{1}]$	$[\bar{1}1\bar{1}]$	$[10\bar{1}]$	$[0\bar{1}\bar{1}]$
23	$(011)[\bar{1}1\bar{1}]$	$[\bar{1}1\bar{1}]$	$[011]$	$[110]$
24	$(\bar{1}\bar{1}0)[\bar{1}1\bar{1}]$	$[\bar{1}1\bar{1}]$	$[\bar{1}\bar{1}0]$	$[\bar{1}01]$

Self- and latent- hardening in the ferrite are modeled using the standard crystal plasticity constitutive equations

$$\dot{g}^{\alpha} = \sum_{\beta=1}^{N} h_{\alpha\beta} \left| \dot{\gamma}^{\beta} \right| \tag{3.3}$$

where the hardening moduli are

$$h_{\alpha\beta} = qh(\bar{\gamma}) \qquad q_{\alpha\beta} = \begin{cases} 1; & \alpha, \beta \text{ coplanar} \\ q; & \text{otherwise} \end{cases} \tag{3.4}$$

with the latent hardening factor q a material parameter, and the hardening rate is

$$h(\bar{\gamma}) = \left\{ h_s + (h_0 - h_s)\operatorname{sech}^2 \left[\frac{h_0 - h_s}{g_s - g_0} \right] \right\} G(\gamma^{\beta}); \qquad \beta \neq \alpha \tag{3.5}$$

$$G(\gamma^{\beta}) = 1 + \sum_{\beta \neq \alpha} f_0 \tanh(\gamma^{\beta} / \gamma_0) \tag{3.6}$$

Here, $\{h_0, h_s, g_0, g_s, f_0, \gamma_0\}$ are material parameters. This material model contains 12 material parameters, which must be determined from experiment.

3.4. Implementation of non-Schmid Bassani-Wu crystal plasticity model

In the simulations described here, this model was implemented as a user-material subroutine (UMAT) in the commercial finite element code ABAQUS v6.9. The tangent modulus method [105] for rate-dependent crystal plasticity models was used to update the slip rate, the strength of slip and the resolved shear stresses in the UMAT.

Fig. 3.2 shows the implementation flowchart of the non-Schmid Bassani-Wu crystal plasticity model in the UMAT. The framework of the UMAT is based on Kysar's single crystal plasticity UMAT [106] that was originally developed by Prof. Y.G. Huang at Harvard University.

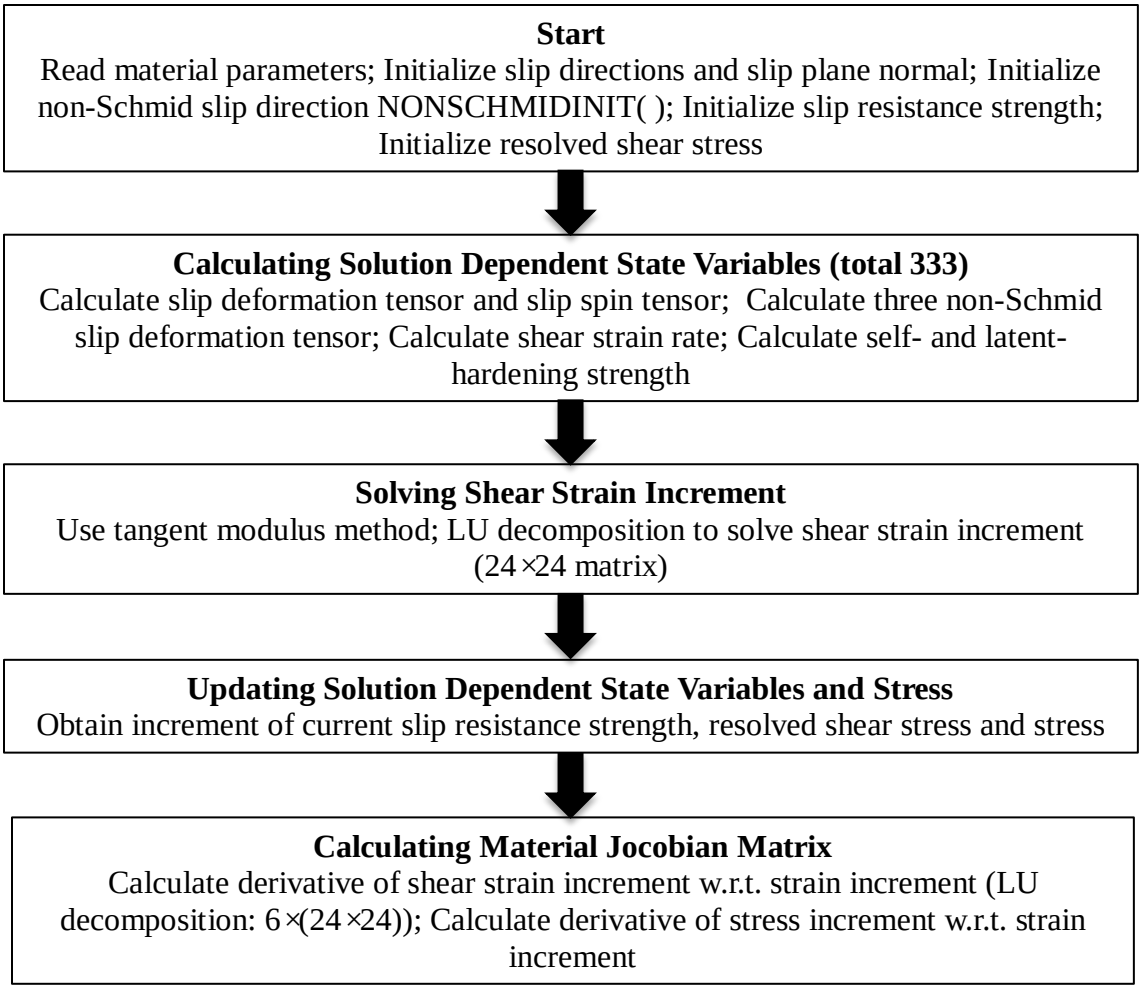

Fig. 3.2 Implementation flowchart of non-Schmid Bassani-Wu crystal plasticity model for ferrite

The new subroutine NONSCHMIDINIT( ) was added into Kysar's UMAT, which is also included in Appendix B. In the new subroutine, the unit vectors $\mathbf{m}_1^\alpha$, $\mathbf{m}^\alpha$, $\mathbf{s}^\alpha$, cross products $\mathbf{m}^\alpha \times \mathbf{s}^\alpha$ and $\mathbf{m}_1^\alpha \times \mathbf{s}^\alpha$, which are denoted by variables SLPNOR1, SLPNOR, SLPDIR, SLPCRS1 and SLPCRS2, respectively, are initialized for 24 slip systems.

The tangent modulus method [105] for rate-dependent crystal plasticity models is used in the UMAT. The basic goal is to estimate an effective slip rate to use over a small

yet finite time step, that is, we seek $\dot{\gamma}^{\alpha} \approx \frac{\Delta\gamma^{\alpha}}{\Delta t}$ for a given time step Δt. We define the increment of shear strain by

$$\Delta\gamma^{\alpha} = \gamma^{\alpha}(t+\Delta t) - \gamma^{\alpha}(t) \tag{3.7}$$

and use the θ-scheme in the finite difference methods [116],

$$\Delta\gamma^{\alpha} = \Delta t\left[(1-\theta)\dot{\gamma}_{t}^{\alpha} + \theta\dot{\gamma}_{t+\Delta t}^{\alpha}\right] \tag{3.8}$$

where the subscript is the time at which the slip rate $\dot{\gamma}^{\alpha}$ is evaluated. The value of θ is recommended to be during 0.5 and 1 [105].

The slip rate $\dot{\gamma}^{\alpha}$ is a function of the resolved shear stress τ^{α} and the current resistance strength g^{α}. Taylor expansion of the slip rate yields

$$\dot{\gamma}_{t+\Delta t}^{\alpha} = \dot{\gamma}_{t}^{\alpha} + \frac{\partial\dot{\gamma}_{t}^{\alpha}}{\partial\tau^{\alpha}}\Delta\tau^{\alpha} + \frac{\partial\dot{\gamma}_{t}^{\alpha}}{\partial g^{\alpha}}\Delta g^{\alpha} \tag{3.9}$$

where $\Delta\tau^{\alpha}$ and Δg^{α} are the increment of the resolved shear stress and the current resistance strength in slip system α within the time increment Δt, respectively. Substituting Eq. (3.9) into Eq. (3.8) gives

$$\Delta\gamma^{\alpha} = \Delta t\left(\dot{\gamma}_{t}^{\alpha} + \theta\frac{\partial\dot{\gamma}_{t}^{\alpha}}{\partial\tau^{\alpha}}\Delta\tau^{\alpha} + \theta\frac{\partial\dot{\gamma}_{t}^{\alpha}}{\partial g^{\alpha}}\Delta g^{\alpha}\right) \tag{3.10}$$

In order to solve the shear strain increment $\Delta\gamma^{\alpha}$, we need to obtain the relations for the increment of resolved shear stress $\Delta\tau^{\alpha}$ and current resistance strength Δg^{α} in terms of the strain increment $\Delta\varepsilon_{ij}$.

Before deriving the increments of resolved shear stress and current resistance strength in terms of the strain increment $\Delta\varepsilon_{ij}$, it is convenient to introduce the slip deformation and spin tensors μ_{ij}^{α} and ω_{ij}^{α}, respectively,

$$\mu_{ij}^{\alpha} = \frac{1}{2}\left(s_i^{*\alpha} m_j^{*\alpha} + s_j^{*\alpha} m_i^{*\alpha} \right) \tag{3.11}$$

$$\omega_{ij}^{\alpha} = \frac{1}{2}\left(s_i^{*\alpha} m_j^{*\alpha} - s_j^{*\alpha} m_i^{*\alpha} \right) \tag{3.12}$$

and the following non-Schmid slip deformation and spin tensors, respectively,

$$\left(\mu_1\right)_{ij}^{\alpha} = \frac{1}{2}\left[s_i^{*\alpha} \left(m_1^*\right)_j^{\alpha} + s_j^{*\alpha} \left(m_1^*\right)_i^{\alpha} \right] \tag{3.13}$$

$$\left(\omega_1\right)_{ij}^{\alpha} = \frac{1}{2}\left[s_i^{*\alpha} \left(m_1^*\right)_j^{\alpha} - s_j^{*\alpha} \left(m_1^*\right)_i^{\alpha} \right] \tag{3.14}$$

$$\left(\mu_2\right)_{ij}^{\alpha} = \frac{1}{2}\left[\left(m_2^*\right)_i^{\alpha} m_j^{*\alpha} + \left(m_2^*\right)_j^{\alpha} m_i^{*\alpha} \right] \tag{3.15}$$

$$\left(\omega_2\right)_{ij}^{\alpha} = \frac{1}{2}\left[\left(m_2^*\right)_i^{\alpha} m_j^{*\alpha} - \left(m_2^*\right)_j^{\alpha} m_i^{*\alpha} \right] \tag{3.16}$$

$$\left(\mu_3\right)_{ij}^{\alpha} = \frac{1}{2}\left[\left(m_3^*\right)_i^{\alpha} \left(m_1^*\right)_j^{\alpha} + \left(m_3^*\right)_j^{\alpha} \left(m_1^*\right)_i^{\alpha} \right] \tag{3.17}$$

$$\left(\omega_3\right)_{ij}^{\alpha} = \frac{1}{2}\left[\left(m_3^*\right)_i^{\alpha} \left(m_1^*\right)_j^{\alpha} - \left(m_3^*\right)_j^{\alpha} \left(m_1^*\right)_i^{\alpha} \right] \tag{3.18}$$

where $\mathbf{m}_2^* = \mathbf{m}^* \times \mathbf{s}^*$ and $\mathbf{m}_3^* = \mathbf{m}_1^* \times \mathbf{s}^*$.

To calculate the increment of the modified slip system strength $g_*^{\alpha} = \max(g^{\alpha} - g_{NS}^{\alpha}, 0)$, we first need to calculate the increment of the non-Schmid part of the modified slip system strength in Eq. (3.2). The non-Schmid slip strength rate is given by

$$\begin{aligned}\dot{g}_{NS}^{\alpha} &= a_1\dot{\mathbf{m}}_1^{*\alpha}\cdot\boldsymbol{\sigma}\mathbf{s}^{*\alpha} + a_1\mathbf{m}_1^{*\alpha}\cdot\dot{\boldsymbol{\sigma}}\mathbf{s}^{*\alpha} + a_1\mathbf{m}_1^{*\alpha}\cdot\boldsymbol{\sigma}\dot{\mathbf{s}}^{*\alpha}\\ &+ a_2\dot{\mathbf{m}}^{*\alpha}\cdot\boldsymbol{\sigma}\mathbf{m}_2^{*\alpha} + a_2\mathbf{m}^{*\alpha}\cdot\dot{\boldsymbol{\sigma}}\mathbf{m}_2^{*\alpha} + a_2\mathbf{m}^{*\alpha}\cdot\boldsymbol{\sigma}\dot{\mathbf{m}}_2^{*\alpha}\\ &+ a_3\dot{\mathbf{m}}_1^{*\alpha}\cdot\boldsymbol{\sigma}\mathbf{m}_3^{*\alpha} + a_3\mathbf{m}_1^{*\alpha}\cdot\dot{\boldsymbol{\sigma}}\mathbf{m}_3^{*\alpha} + a_3\mathbf{m}_1^{*\alpha}\cdot\boldsymbol{\sigma}\dot{\mathbf{m}}_3^{*\alpha}\end{aligned} \tag{3.19}$$

Recall that

$$\begin{aligned}&\mathbf{s}^{*\alpha} = \mathbf{F}^{*}\mathbf{s}^{\alpha}; && \dot{\mathbf{s}}^{*\alpha} = \mathbf{L}^{*}\mathbf{s}^{*\alpha}\\ &\mathbf{m}^{*\alpha} = -\mathbf{m}^{\alpha}\mathbf{F}^{*-1}; && \dot{\mathbf{m}}^{*\alpha} = -\mathbf{m}^{*\alpha}\mathbf{L}^{*}\\ &\mathbf{m}_1^{*\alpha} = -\mathbf{m}_1\mathbf{F}^{*-1}; && \dot{\mathbf{m}}_1^{*\alpha} = -\mathbf{m}_1^{*\alpha}\mathbf{L}^{*}\\ &\mathbf{m}_2^{*\alpha} = \mathbf{m}^{*\alpha}\times\mathbf{s}^{*\alpha} = -\mathbf{F}^{*-T}\mathbf{m}_2\mathbf{F}^{*T}; && \dot{\mathbf{m}}_2^{*\alpha} = \dot{\mathbf{m}}^{*\alpha}\times\mathbf{s}^{*\alpha} + \mathbf{m}^{*\alpha}\times\dot{\mathbf{s}}^{*\alpha} = \mathbf{m}_2^{*\alpha}\left(\mathbf{L}^{*T} - \mathbf{L}^{*}\right)\\ &\mathbf{m}_3^{*\alpha} = \mathbf{m}_1^{*\alpha}\times\mathbf{s}^{*\alpha} = -\mathbf{F}^{*-T}\mathbf{m}_3\mathbf{F}^{*T}; && \dot{\mathbf{m}}_3^{*\alpha} = \dot{\mathbf{m}}_1^{*\alpha}\times\mathbf{s}^{*\alpha} + \mathbf{m}_1^{*\alpha}\times\dot{\mathbf{s}}^{*\alpha} = \mathbf{m}_3^{*\alpha}\left(\mathbf{L}^{*T} - \mathbf{L}^{*}\right)\end{aligned} \tag{3.20}$$

Then the non-Schmid slip strength rate is written as,

$$\begin{aligned}\dot{g}_{NS}^{\alpha} &= a_1\mathbf{m}_1^{*\alpha}\left(\overset{\nabla^{*}}{\boldsymbol{\sigma}} + \boldsymbol{\sigma}\mathbf{D}^{*} - \mathbf{D}^{*}\boldsymbol{\sigma}\right)\mathbf{s}^{*\alpha}\\ &+ a_2\mathbf{m}^{*\alpha}\left(\overset{\nabla^{*}}{\boldsymbol{\sigma}} + \boldsymbol{\sigma}\mathbf{W}^{*} - \mathbf{D}^{*}\boldsymbol{\sigma}\right)\mathbf{m}_2^{*\alpha}\\ &+ a_3\mathbf{m}_1^{*\alpha}\left(\overset{\nabla^{*}}{\boldsymbol{\sigma}} + \boldsymbol{\sigma}\mathbf{W}^{*} - \mathbf{D}^{*}\boldsymbol{\sigma}\right)\mathbf{m}_3^{*\alpha}\end{aligned} \tag{3.21}$$

where $\mathbf{D}^{*}$ is the rate of stretching of the lattice, and $\mathbf{W}^{*}$ is the spin tensor in deformed configuration. The Jaumann rate of the Cauchy stress in deformed configuration is

$$\overset{\nabla^{*}}{\boldsymbol{\sigma}} = \dot{\boldsymbol{\sigma}} - \mathbf{W}^{*}\boldsymbol{\sigma} + \boldsymbol{\sigma}\mathbf{W}^{*} \tag{3.22}$$

To proceed, consider the indentity

$$\left(\boldsymbol{\omega}_1^{\alpha}\boldsymbol{\sigma} - \boldsymbol{\sigma}\boldsymbol{\omega}_1^{\alpha}\right)\cdot\mathbf{D}^{*} = \mathbf{m}_1^{*\alpha}\left(\boldsymbol{\sigma}\mathbf{D}^{*} - \mathbf{D}^{*}\boldsymbol{\sigma}\right)\mathbf{s}^{*\alpha} \tag{3.23}$$

The above identity can be obtained by expressing the terms in component form, that is,

$$\begin{aligned}\left(\left(\omega_1\right)_{il}\sigma_{lj}-\sigma_{il}\left(\omega_1\right)_{lj}\right)D_{ij}^{*} &= \frac{1}{2}s_i^{*}\left(m_1\right)_l^{*}\sigma_{lj}D_{ij}^{*}-\frac{1}{2}s_l^{*}\left(m_1\right)_i^{*}\sigma_{lj}D_{ij}^{*}\\ &\quad -\frac{1}{2}\sigma_{il}s_l^{*}\left(m_1\right)_j^{*}D_{ij}^{*}+\frac{1}{2}\sigma_{il}s_j^{*}\left(m_1\right)_l^{*}D_{ij}^{*}\\ &= \frac{1}{2}s_i^{*}\left(m_1\right)_l^{*}\sigma_{lj}D_{ij}^{*}+\frac{1}{2}\sigma_{jl}s_i^{*}\left(m_1\right)_l^{*}D_{ij}^{*}\\ &\quad -\frac{1}{2}\sigma_{jl}s_l^{*}\left(m_1\right)_i^{*}D_{ij}^{*}-\frac{1}{2}s_l^{*}\left(m_1\right)_i^{*}\sigma_{lj}D_{ij}^{*}\\ &= \left(m_1\right)_l^{*}\left(\sigma_{lj}D_{ji}^{*}-D_{lj}^{*}\sigma_{ji}\right)s_i^{*}\end{aligned} \tag{3.24}$$

And the term in Eq.(3.21) including the Jaumann rate can be written as

$$\begin{aligned}\mathbf{m}_1^{*\alpha}\overset{\nabla^{*}}{\boldsymbol{\sigma}}\mathbf{s}^{*\alpha} &= \mathbf{m}_1^{*\alpha}(\Lambda:\mathbf{D}^{*})\mathbf{s}^{*\alpha}\\ &= \mathbf{m}_1^{*\alpha}\mathbf{s}^{*\alpha}:\Lambda:\mathbf{D}^{*}\\ &= \boldsymbol{\mu}_1^{\alpha}:\Lambda:\mathbf{D}^{*}\end{aligned} \tag{3.25}$$

where we have considered the symmetry in elastic moduli tensor Λ. Substituting Eqs. (3.23) and (3.25) into Eq. (3.21), the term related to parameter a_1 can be expressed as

$$a_1\mathbf{m}_1^{*\alpha}\left(\overset{\nabla^{*}}{\boldsymbol{\sigma}}+\boldsymbol{\sigma}\mathbf{D}^{*}-\mathbf{D}^{*}\boldsymbol{\sigma}\right)\mathbf{s}^{*\alpha}=a_1(\boldsymbol{\mu}_1^{\alpha}:\Lambda+\boldsymbol{\omega}_1\boldsymbol{\sigma}-\boldsymbol{\sigma}\boldsymbol{\omega}_1):\mathbf{D}^{*} \tag{3.26}$$

Finally, based on Eq. (3.21), the increment of the non-Schmid slip strength Δg_{NS}^{α} can be written as

$$\begin{aligned}\Delta g_{NS}^{\alpha} = a_1 &\left[\Lambda_{ijkl} \left(\mu_1\right)_{kl}^{\alpha} + \left(\omega_1\right)_{ik}^{\alpha} \sigma_{jk} + \left(\omega_1\right)_{jk}^{\alpha} \sigma_{ik} \right] \left[\Delta\varepsilon_{ij} - \sum_{\beta} \Delta\gamma^{\beta} \mu_{ij}^{\beta} \right] \\ &+ a_2 \left(\mathbf{m}^{*}\mathbf{m}_2^{*}\right)_{kl} \Lambda_{ijkl} \left[\Delta\varepsilon_{ij} - \sum_{\beta} \Delta\gamma^{\beta} \mu_{ij}^{\beta} \right] \\ &+ a_2 \left(\mathbf{m}^{*}\mathbf{m}_2^{*}\right)_{kl} \sigma_{li} \left(W_{ik}\Delta t - \sum_{\beta} \Delta\gamma^{\beta} \omega_{ik}^{\beta} \right) \\ &- a_2 \left(\mathbf{m}^{*}\mathbf{m}_2^{*}\right)_{kl} \left(\Delta\varepsilon_{ki} - \sum_{\beta} \Delta\gamma^{\beta} \mu_{ki}^{\beta} \right) \sigma_{il} \\ &+ a_3 \left(\mathbf{m}_1^{*}\mathbf{m}_3^{*}\right)_{kl} \Lambda_{ijkl} \left[\Delta\varepsilon_{ij} - \sum_{\beta} \Delta\gamma^{\beta} \mu_{ij}^{\beta} \right] \\ &+ a_3 \left(\mathbf{m}_1^{*}\mathbf{m}_3^{*}\right)_{kl} \sigma_{li} \left(W_{ik}\Delta t - \sum_{\beta} \Delta\gamma^{\beta} \omega_{ik}^{\beta} \right) \\ &- a_3 \left(\mathbf{m}_1^{*}\mathbf{m}_3^{*}\right)_{kl} \left(\Delta\varepsilon_{ki} - \sum_{\beta} \Delta\gamma^{\beta} \mu_{ki}^{\beta} \right) \sigma_{il} \end{aligned} \tag{3.27}$$

Now the increment of the modified slip system strength $g_{*}^{\alpha} = \max(g^{\alpha} - g_{NS}^{\alpha}, 0)$ is given by

$$\begin{aligned}\Delta g_{*}^{\alpha} &= \max(\Delta g^{\alpha} - \Delta g_{NS}^{\alpha}, 0) \\ &= \max\left(\sum_{\beta} h_{\alpha\beta} \left|\Delta\gamma\right| - \Delta g_{NS}^{\alpha}, 0 \right)\end{aligned} \tag{3.28}$$

The resolved shear stress on the α slip system was defined as

$$\tau^{\alpha} = \mathbf{m}^{*\alpha} \cdot \sigma \mathbf{s}^{*\alpha} \tag{3.29}$$

The rate of the resolved shear stress can be written as

$$\dot{\tau}^{\alpha} = \mathbf{m}^{*\alpha} \left(\Lambda : \mathbf{D}^{*} + \boldsymbol{\sigma}\mathbf{D}^{*} - \mathbf{D}^{*}\boldsymbol{\sigma} \right) \mathbf{s}^{*\alpha} \tag{3.30}$$

Then the increment of resolved shear stress is given by

$$\Delta\tau^{\alpha} = \left[\Lambda_{ijkl}\mu_{kl}^{\alpha} + \omega_{ik}^{\alpha}\sigma_{jk} + \omega_{jk}^{\alpha}\sigma_{ik} \right] \left[\Delta\varepsilon_{ij} - \sum_{\beta} \Delta\gamma^{\beta} \mu_{ij}^{\beta} \right] \tag{3.31}$$

The Jaumann rate of Cauchy stress is given by

$$\overset{\nabla^*}{\boldsymbol{\sigma}} = \Lambda : \mathbf{D}^* - \boldsymbol{\sigma}(\mathbf{I} : \mathbf{D}^*) \tag{3.32}$$

where $\mathbf{I}$ is the second order identical tensor. Note the term $\boldsymbol{\sigma}(\mathbf{I} : \mathbf{D}^*)$ has been neglected in the previous since stress is much less than elastic moduli. The Jaumann rate $\overset{\nabla^*}{\boldsymbol{\sigma}}$ is related to the stress rate on axes rotating with the material $\overset{\nabla}{\boldsymbol{\sigma}}$, by

$$\begin{aligned} \overset{\nabla}{\boldsymbol{\sigma}} &= \overset{\nabla^*}{\boldsymbol{\sigma}} - (\mathbf{W} - \mathbf{W}^*) \cdot \boldsymbol{\sigma} + \boldsymbol{\sigma} \cdot (\mathbf{W} - \mathbf{W}^*) \\ &= \Lambda : \mathbf{D}^* - \boldsymbol{\sigma}(\mathbf{I} : \mathbf{D}^*) - (\mathbf{W} - \mathbf{W}^*) \cdot \boldsymbol{\sigma} + \boldsymbol{\sigma} \cdot (\mathbf{W} - \mathbf{W}^*) \end{aligned} \tag{3.33}$$

where $\overset{\nabla}{\boldsymbol{\sigma}} = \dot{\boldsymbol{\sigma}} - \mathbf{W}\boldsymbol{\sigma} + \boldsymbol{\sigma}\mathbf{W}$. The stress increments $\Delta\sigma_{ij}$ on axes rotating with the material are given by

$$\begin{aligned} \Delta\sigma_{ij} &= \Lambda_{ijkl}\left[\Delta\varepsilon_{kl} - \sum_{\alpha}\Delta\gamma^{\alpha}\mu_{kl}^{\alpha}\right] - \sigma_{ij}\Delta\varepsilon_{kk} - \sum_{\alpha}\Delta\gamma^{\alpha}\omega_{ik}^{\alpha}\sigma_{jk} - \sum_{\alpha}\Delta\gamma^{\alpha}\omega_{jk}^{\alpha}\sigma_{ik} \\ &= \Lambda_{ijkl}\Delta\varepsilon_{kl} - \sigma_{ij}\Delta\varepsilon_{kk} - \sum_{\alpha}\left(\Lambda_{ijkl}\mu_{kl}^{\alpha} + \omega_{ik}^{\alpha}\sigma_{jk} + \omega_{jk}^{\alpha}\sigma_{ik}\right)\Delta\gamma^{\alpha} \end{aligned} \tag{3.34}$$

For given strain increments $\Delta\varepsilon_{ij}$, substituting Eqs. (3.28) and (3.31) into (3.10), the shear strain increments $\Delta\gamma^{\alpha}$ can be uniquely determined by,

$$\sum_{\beta}\Bigg\{\delta_{\alpha\beta}+\theta\Delta t\frac{\partial\dot{\gamma}^{\alpha}}{\partial\tau^{\alpha}}\left(\Lambda_{ijkl}\mu_{kl}^{\alpha}+\omega_{ik}^{\alpha}\sigma_{jk}+\omega_{jk}^{\alpha}\sigma_{ik}\right)\mu_{kl}^{\beta}$$
$$-\theta\Delta t\frac{\partial\dot{\gamma}^{\alpha}}{\partial g^{\alpha}}\Bigg\{h_{\alpha\beta}sign(\dot{\gamma}_{t}^{\beta})+a_1\Big[\Lambda_{ijkl}\left(\mu_1\right)_{kl}^{\alpha}+\left(\omega_1\right)_{ik}^{\alpha}\sigma_{jk}+\left(\omega_1\right)_{jk}^{\alpha}\sigma_{ik}\Big]\mu_{ij}^{\beta}$$
$$+a_2\left(\mathbf{m}^{*}\mathbf{m}_2^{*}\right)_{kl}\Lambda_{ijkl}\mu_{ij}^{\beta}+a_2\left(\mathbf{m}^{*}\mathbf{m}_2^{*}\right)_{kl}\sigma_{li}\omega_{ik}^{\beta}-a_2\left(\mathbf{m}^{*}\mathbf{m}_2^{*}\right)_{kl}\mu_{ki}^{\beta}\sigma_{il}$$
$$+a_3\left(\mathbf{m}_1^{*}\mathbf{m}_3^{*}\right)_{kl}\Lambda_{ijkl}\mu_{ij}^{\beta}+a_3\left(\mathbf{m}_1^{*}\mathbf{m}_3^{*}\right)_{kl}\sigma_{li}\omega_{ik}^{\beta}-a_3\left(\mathbf{m}_1^{*}\mathbf{m}_3^{*}\right)_{kl}\mu_{ki}^{\beta}\sigma_{il}\Bigg\}\Bigg\}\Delta\gamma^{\beta} \quad (3.35)$$
$$=\dot{\gamma}_{t}^{\alpha}\Delta t+\theta\Delta t\frac{\partial\dot{\gamma}^{\alpha}}{\partial\tau^{\alpha}}\left(\Lambda_{ijkl}\mu_{kl}^{\alpha}+\omega_{ik}^{\alpha}\sigma_{jk}+\omega_{jk}^{\alpha}\sigma_{ik}\right)\Delta\varepsilon_{ij}$$
$$-\theta\Delta t\frac{\partial\dot{\gamma}^{\alpha}}{\partial g^{\alpha}}\Bigg\{a_1\Big[\Lambda_{ijkl}\left(\mu_1\right)_{kl}^{\alpha}+\left(\omega_1\right)_{ik}^{\alpha}\sigma_{jk}+\left(\omega_1\right)_{jk}^{\alpha}\sigma_{ik}\Big]\Delta\varepsilon_{ij}$$
$$+a_2\left(\mathbf{m}^{*}\mathbf{m}_2^{*}\right)_{kl}\Lambda_{ijkl}\Delta\varepsilon_{ij}+a_2\left(\mathbf{m}^{*}\mathbf{m}_2^{*}\right)_{kl}\sigma_{li}W_{ik}\Delta t-a_2\left(\mathbf{m}^{*}\mathbf{m}_2^{*}\right)_{kl}\Delta\varepsilon_{ki}\sigma_{il}$$
$$+a_3\left(\mathbf{m}_1^{*}\mathbf{m}_3^{*}\right)_{kl}\Lambda_{ijkl}\Delta\varepsilon_{ij}+a_3\left(\mathbf{m}_1^{*}\mathbf{m}_3^{*}\right)_{kl}\sigma_{li}W_{ik}\Delta t-a_3\left(\mathbf{m}_1^{*}\mathbf{m}_3^{*}\right)_{kl}\Delta\varepsilon_{ki}\sigma_{il}\Bigg\}$$

where $\delta_{\alpha\beta}$ is the Kronecker delta. Once the shear strain increments $\Delta\gamma^{\alpha}$ are solved in term of the strain increments $\Delta\varepsilon_{ij}$, all other increments can be obtained through Eqs. (3.28), (3.31) and (3.34).

All the above-mentioned formulas have been implemented into the ABAQUS UMAT.

3.5. Determining ferrite material parameters in DP steels

A comparison between predicted and measured stress-strain curves for ferritic micropillars is shown in Fig. 3.3. The crystal plasticity model with the non-Schmid effect yields a good fit to experimentally measured stress-strain curves (Fig. 3.1) [43]. The low flow strength of the micropillars (e.g. pillar 2 in DF140T) corresponds to single slip, while the higher flow strength of ferritic micropillars (e.g. pillar 3 in DF140T) corresponds to multiple slip. The resulting material parameters are listed in Table 3.3. The non-Schmid parameters are assumed to be same for both steels, since the dislocation

core structures in the two materials are likely to be similar. The ferrite in DF140T has a higher initial yield stress but lower hardening rate than DP980. The higher dislocation density due to the finer ferrite grains in DP980 may explain the higher hardening rates of DP980.

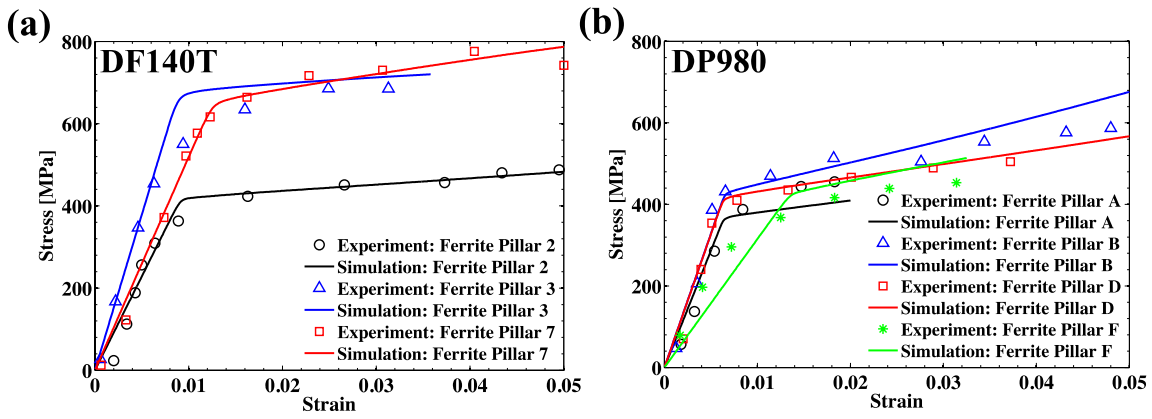

Fig. 3.3 Comparison of measured and predicted stress-strain curves for ferrite micropillars extracted from (a) DF140T and (b) DP980. Crystal plasticity-based model with non-Schmid effect can best fit all ferrite micropillars simultaneously with crystallographic orientations (specified by the initial orientation of the compression axis): (a) [315] (Pillar 2), [001] (Pillar 3) and [556] (Pillar 7) of DF140T and (b) [516] (Pillar A), [324] (Pillar B) and [416] (Pillar C) of DP980. Experimental data appear in Fig. 3.1.

The importance of including non-Schmid behavior in the constitutive model for ferrite can be demonstrated by means of two simple numerical tests. In the first test, we create a 'virtual' micropillar which is identical to DF140T but displays no non-Schmid behavior (i.e. the virtual material has identical material parameters to those listed in Table 3.3, but the coefficients $a_1 = a_2 = a_3 = 0$). The stress-strain curves for this material are compared with experimental data in Fig. 3.4(a). The non-Schmid behavior clearly has a significant effect on the orientation dependence of the flow strength of the ferritic micropillars. As a second test, we have attempted to fit the predictions of a classical

Bassani-Wu crystal plasticity model to the experimentally measured flow behavior in the ferritic micropillars (obtained by enforcing $a_1 = a_2 = a_3 = 0$ during the optimization process). The predicted best fit is compared with experimental data in Fig. 3.4(b). Without the non-Schmid terms, it is impossible to fit the experimental data correctly.

Table 3.3 Material parameters determined by 3D finite element simulations of micropillar compression tests on the ferritic phase of DF140T and DP980.

Two commercial DP steels	DF140T	DP980
Strain rate $\dot{\gamma}_0$ (s^{-1})	0.002	0.009
Stress exponent m	41.0	67.8
Initial hardening rate h_0 (MPa)	97.1	556.3
Saturated hardening rate h_s (MPa)	5.36	188.9
Initial flow stress g_0 (MPa)	253.8	238.7
Saturated flow stress g_s (GPa)	3.22	0.61
Characteristic shear strain γ_0	65.1	55.2
Latent hardening coefficient f_0	99.9	0.08
Latent hardening coefficient q	1.4	1.0
Non-Schmid effect parameter a_1	0.6	0.6
Non-Schmid effect parameter a_2	0.01	0.01
Non-Schmid effect parameter a_3	0.2	0.2

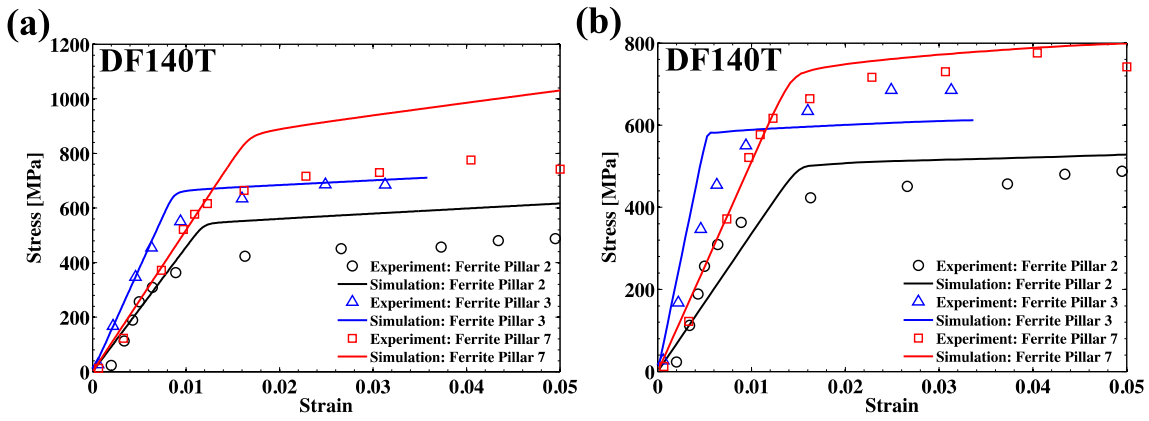

Fig. 3.4 Comparison of measured and predicted stress-strain curves for ferritic micropillars extracted from DF140T using (a) non-Schmid crystal plasticity model with optimal material parameters but $a_1 = a_2 = a_3 = 0$ and (b) the best fit of a classical Bassani-Wu crystal plasticity model without non-Schmid behavior to the experimental data, respectively. Experimental data appear in Fig. 3.1.

Chapter 4. Mechanical Behavior of Dual Phase Steels

Using material parameters determined in Chapters 2 and 3, the mechanical behavior of DP steel microstructures will be predicted in this Chapter. The volume fraction of martensite in both DP steels will be determined in Section 4.1. After generating the 3D RVEs of both DP steels in Section 4.2, the predicted and measured uniaxial stress-strain curves of both DP steels will be compared in Section 4.3, which shows that the predictions match experiments very well using micropillar-calibrated crystal plasticity models described in Chapters 2 and 3. Finally, the non-associated plastic flow behavior of both DP steels resulting from the non-Schmid behavior of ferrite is described in Section 4.4, where the strength differential values and forming limit strains are determined using the 3D RVEs of both DP steels subjected to multiaxial loading.

4.1. Determination of volume fraction of martensite in DP steels

For DP steels, the volume fraction of martensite is one of the important factors needed to determine their mechanical behavior. The measurement of the volume fraction of the martensite in DP steels becomes essential before investigating the plastic behavior of DP steels. A simple way to determine the volume fraction of martensite is to measure the area fraction of martensite in several SEM pictures of DP steels and then average

these area fractions. The volume fraction of martensite in DP steels can be approximated by the average area fraction through the following relation,

$$\overline{A_M} = \frac{1}{N}\sum_{s=1}^{N} A_M^s = \frac{1}{N}\sum_{s=1}^{N} \frac{n_M^s}{n^s} = \frac{1}{N \cdot n}\sum_{s=1}^{N} n_M^s = \frac{1}{n^{tot}}\sum_{s=1}^{N} n_M^s = \frac{n_M^{tot}}{n^{tot}} \xrightarrow{N\to\infty} V_M \tag{4.1}$$

where $\overline{A_M}$ is the average area fraction of martensite, N is the total number of SEM pictures, A_M^s is the area fraction of martensite of the *s*-th SEM picture, n^s is the total pixel number of the *s*-th SEM picture, n_M^s is the total pixel number of martensite in the *s*-th SEM picture, n^{tot} is the total pixel number of all SEM pictures and n_M^{tot} is the total pixel number of martensite for all SEM pictures. Here we assume that the each SEM picture has the same pixel number, that is, $n^s = n$.

Using 4 SEM images for DF140T and 13 SEM images for DP980, we determine the volume fraction of martensite in DP steels DF140T and DP980. We first convert the SEM pictures into black-white binary images by setting a threshold in MATLAB, and then calculate the pixel number of black color (unity in MATLAB) in black-white binary images. Fig. 4.1 shows examples of SEM pictures and the corresponding black-white binary images used to calculate the pixel number of black color (martenstie phase). Following Eq. (4.1), we obtain the volume fractions of martensite, 0.39 ± 0.02 for DF140T and 0.61 ± 0.03 for DP980.

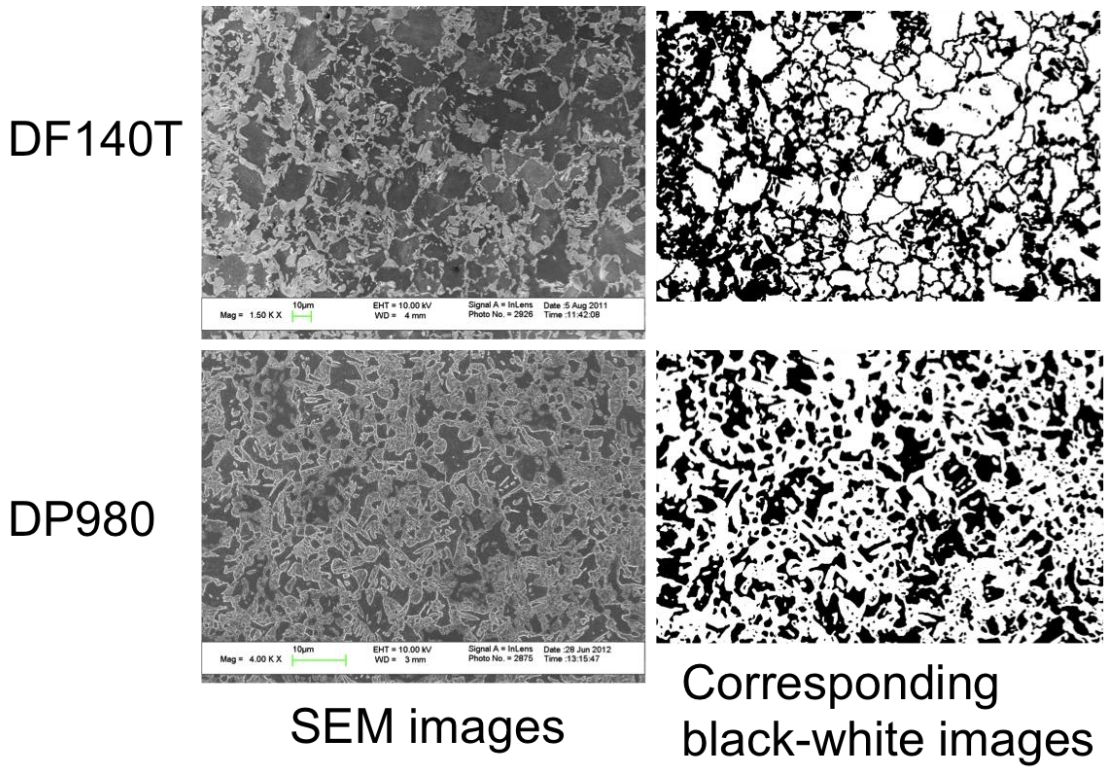

Fig. 4.1 Examples of SEM images and the corresponding black-white binary images used to determine the volume fraction of martensite in DP steels DF140T and DP980. Light and dark regions in SEM images are martensite and ferrite phases, respectively. Black and white colors in black-white images denote the martensite and ferrite phases, respectively. (SEM images provided by Dr. H. Ghassemi-Armaki at Brown University).

4.2. Generation of DP steel microstructures

The calibrated crystal plasticity models for ferrite and martensite can now be combined to predict the overall flow behavior of the two DP steels. To this end, a computational representation of the DP steel microstructure must be generated. The DP steels studied in this paper consist of ferrite grains, which are surrounded by particles of lath martensite, as illustrated in Fig. 1.4. A computational model of this microstructure is generated as follows (Fig. 4.2). First, a 3D ferrite grain structure is generated using a simulated annealing process [44] with brick meshing (Fig. 4.2(a)), where the simulated annealing process refers to the geometric optimization of space-filling objects without too

much overlap. Random crystallographic orientations are assigned to the ferrite grains. Secondly, prior austenite grains are nucleated randomly on the ferrite grain boundaries and then grown at a fast rate along ferrite grain boundaries and a slow rate along other directions (Fig. 4.2(b) and Fig. 4.2(c)). A growth-rate ratio of 2:1 was found to generate a microstructure very similar to the experimental micrographs. The growth of prior austenite grains is terminated when the volume fraction reaches a prescribed target value (61%±3% in DP980 and 39%±2% in DF140T). Note that the prior austenite grain nucleation and growth processes are based on brick meshing, that is, brick elements representing ferrite grains will be converted to represent prior austenite grains.

A martensitic microstructure is then generated within each of the prior-austenite grains, following the procedure described in detail in Section 2.3 [15]. First, random crystallographic orientations $[A]_{\gamma}$ are assigned to each prior austenite grain. The prior austenite grains are then divided into packets using L_{∞} Voronoi tessellation. An element is selected at random within each prior austenite grain to act as the Voronoi center [28, 29, 96] (Fig. 4.2(d) and Fig. 4.2(e)). The distance between Voronoi centers and other elements in the prior austenite grain is measured by the L_{∞} norm or maximum norm [97]. The number of Voronoi centers in each prior austenite grain controls the packet size. One of four $\{111\}_{\gamma}$ habit planes in the Kurdjimov-Sachs (K-S) family of orientations is randomly chosen for each packet [13, 16]. Finally, each packet is sub-divided into blocks, using a similar L_{∞} Voronoi tessellation (Fig. 4.2(f)). The number of Voronoi centers in each packet controls the block size. One orientation variant selected at random from the 6 possible K-S orientation variants of each packet group is assigned to each block. The orientations of the blocks $[A]_{\alpha'}$ are related to the orientations of prior austenite grains via

the transformation $[T]=[A]_{\alpha'}[A]_{\gamma}^{-1}$, which can be derived from the 24 K-S orientation variants [98].

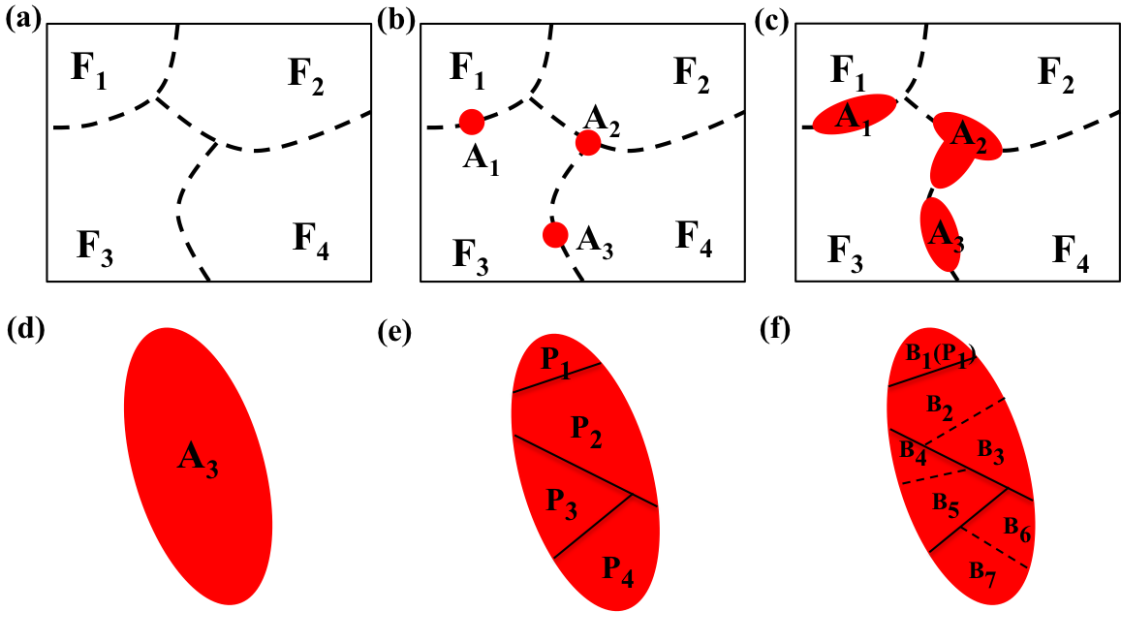

Fig. 4.2 Schematic showing the DP microstructure generation procedure (a)->(b)->(c) of ferrite and lath martensite in a low-carbon DP steel. Procedure (d)->(e)->(f) shows the microstructure generation of lath martensite in a low-carbon DP steel. (a) Ferrite grains F_i are generated by a simulated annealing process [44]. Thick dashed black lines are ferrite grain boundaries. (b) Prior austenite grains A_i (red color) are nucleated randomly on the ferrite grain boundaries and (c) then grown at a fast rate along ferrite grain boundaries and a slow rate along other directions. (d)-(e) Each prior austenite grain A_i is divided into packets P_i using L_∞ Voronoi tessellation. Thin black lines are packet boundaries. (f) Each packet is subdivided into blocks B_i using L_∞ Voronoi tessellation. Thin dashed black lines are block boundaries.

RVEs generated using this procedure are shown in Fig. 4.3 for both steels. The RVEs capture macroscopic features such as differences in the volume fraction of martensite in the two steels (61%±3% in DP980, compared to 39%±2% in DF140T). In addition, the microstructure generation procedure can duplicate the initial texture in the steel, as well as the shape and distributions of the two phases.

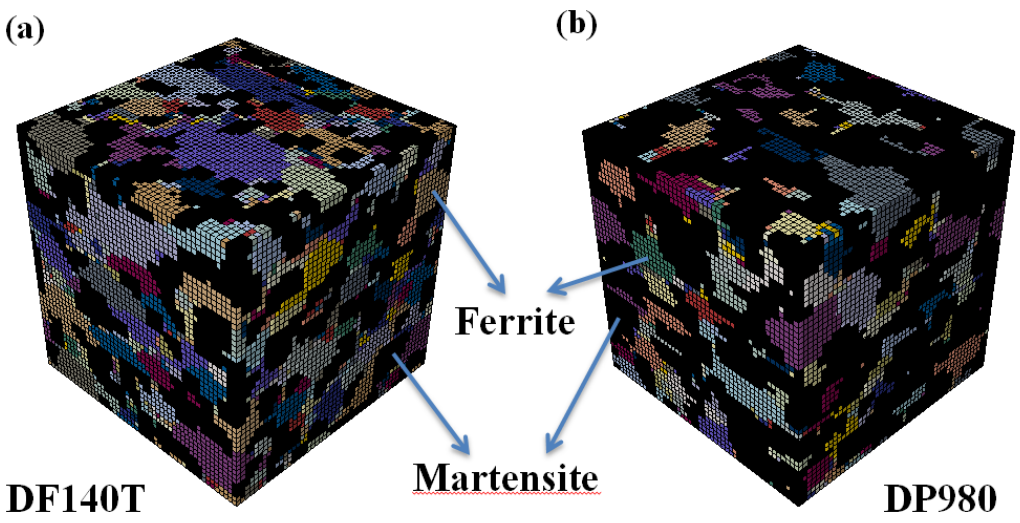

Fig. 4.3 Representative volume elements generated for (a) DF140T and (b) DP980. Ferrite grains or martensite blocks are distinguished by the different colors. Black color denotes the martensite phases in both steels. More black color in (b) indicates higher volume fraction of martensite in DP980 (61% ±3%) than in DF140T (39% ±2%). The size of RVE is 100μm x 100μm x 100μm and the brick element size is 2μm x 2μm x 2μm. Total 125,000 elements are used.

4.3. Comparison of measured and predicted behavior for DP steels

The computational model, as well as the procedure used to determine material parameters for the two phases of the steel from micropillar experiments, can be validated by comparing the predicted behavior of the model microstructures described in the preceding section with experimental measurements in Fig. 1.5 [43]. To this end, the volume elements were subjected to periodic boundary conditions representing uniaxial tension, and the average stresses in the volume elements are computed. Note that the boundary conditions preclude necking in the volume element, so predictions can only be compared to experiment for strains below 10%, which correspond to uniform elongation.

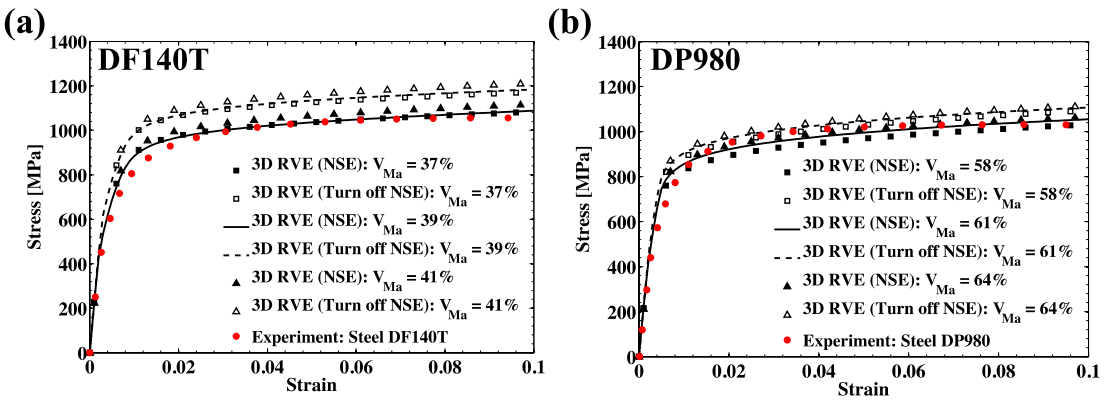

Fig. 4.4 Comparison of measured and predicted uniaxial stress-strain curves of (a) DF140T and (b) DP980. For each DP steel, three RVEs with measured mean volume fraction of martensite (39% for DF140T and 61% for DP980) and its standard variance (2% for DF140T and 3% for DP980) show almost the same flow and hardening behaviors, and in good agreement with experiments. Predicted results with turning off non-Schmid effect show larger deviation from experimental results, compared to the predicted results with non-Schmid effect. NSE in legends means the non-Schimd effect. Experimental data appear in Fig. 1.5.

Fig. 4.4(a) and Fig. 4.4(b) compare the measured and predicted uniaxial tensile stress-strain curves of DF140T and DP980. Numerical predictions are shown for representative volume elements with martensite volume fractions in a narrow range about the nominal value, to assess the influence of statistical variations in volume fraction. The predicted stress-strain curves are in excellent agreement with experimental data in Fig. 1.5 [43]. Fig. 4.5 and Fig. 4.6 compare the Von Mises stress and equivalent plastic strain contours of DP140T and DP980. The simulations confirm that the two steels achieve their strength in different ways: in DP980, there is a large martensite volume fraction, but the flow strength of the martensite is comparatively low; whereas DF140T has a smaller volume fraction of martensite with a higher strength.

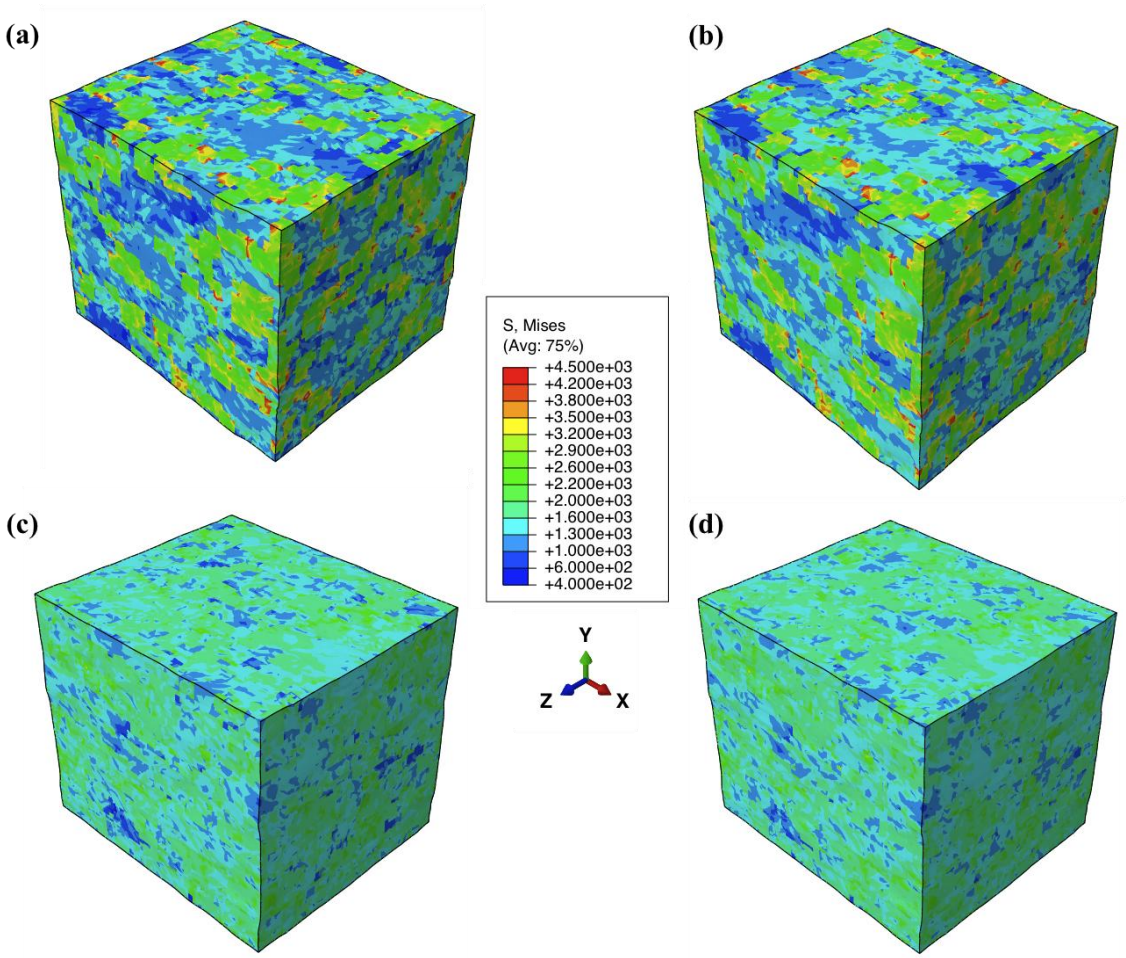

Fig. 4.5 Von Mises stress contours of (a) DF140T (V_m=39%), (b) DF140T (V_m=39% and turn off non-Schmid effect), (c) DP980 (V_m=61%) and (d) DP980 (V_m=61% and turn off non-Schmid effect). The unit of stress in legend is MPa.

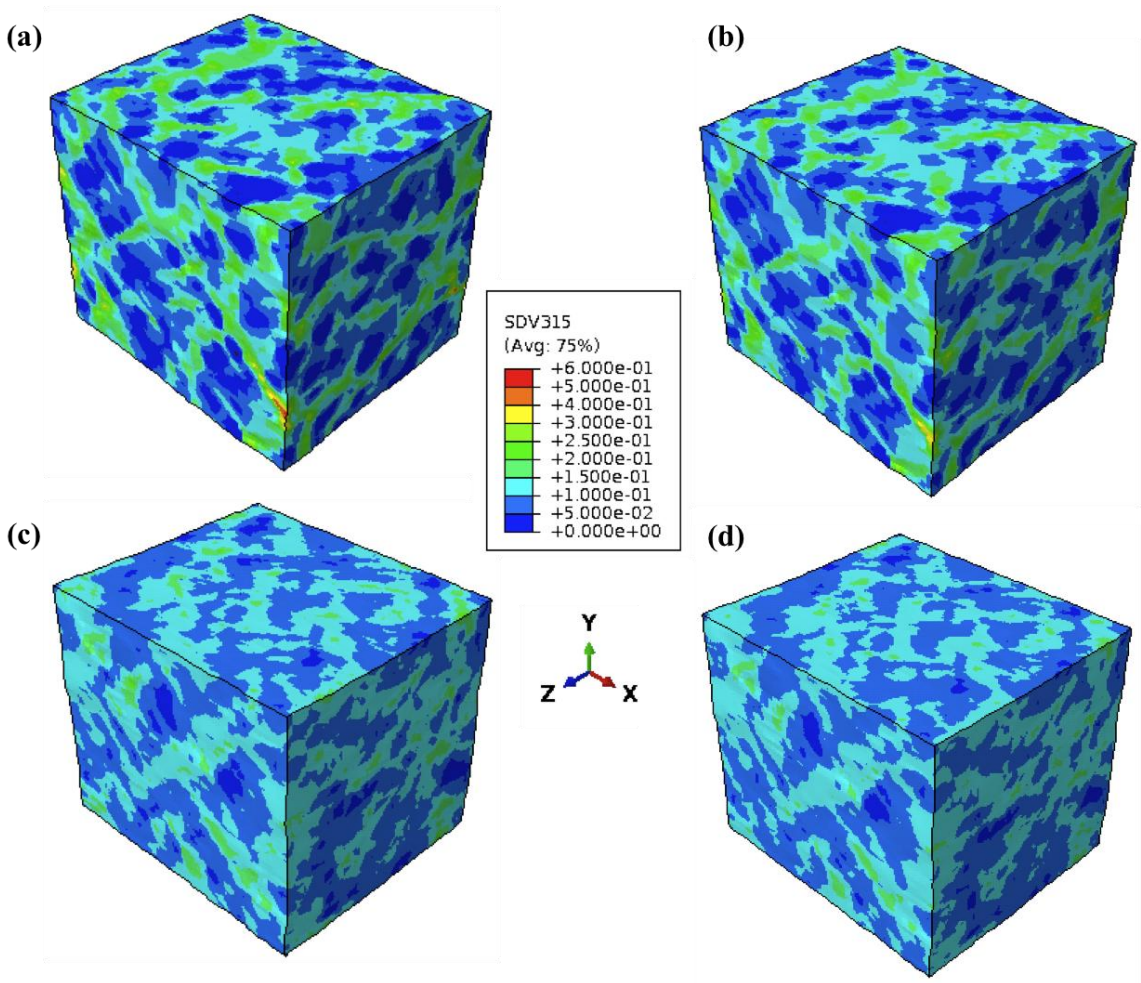

Fig. 4.6 Equivalent plastic strain contours for (a) DF140T (V_m=39%), (b) DF140T (V_m=39% and turn off non-Schmid effect), (c) DP980 (V_m=61%) and (d) DP980 (V_m=61% and turn off non-Schmid effect).

The simulations also provide a way to probe the roles of the different phases in determining the overall response of the microstructure. For this purpose, Fig. 4.7 shows the fraction of the average equivalent plastic strain rate that is accommodated by martensite and ferrite in the two steels. The fractions of the average equivalent plastic strain rate in the ferrite and martensite are computed as

$$f_f = \frac{\left\langle \dot{\varepsilon}_{eq}^{f} \right\rangle}{\left\langle \dot{\varepsilon}_{eq}^{f} \right\rangle + \left\langle \dot{\varepsilon}_{eq}^{m} \right\rangle}; \quad f_m = 1 - f_f \tag{4.2}$$

respectively, where $\left\langle \dot{\varepsilon}_{eq}^{f} \right\rangle$ denotes the volume averaged strain rate in the ferrite phase, which is computed from the finite elements using

$$\left\langle \dot{\varepsilon}_{eq}^{f} \right\rangle = \frac{1}{V^f} \int_{V^f} \dot{\varepsilon}_{eq} dV \approx \frac{\sum_{i=1}^{N_{el}^f} \dot{\varepsilon}_{eq}^{i} \cdot V_{el}^{i}}{\sum_{i=1}^{N_{el}^f} V_{el}^{i}} \tag{4.3}$$

Here, V^f is the volume of ferrite phase, V_{el}^{i}, $\dot{\varepsilon}_{eq}^{i}$ are the volume and equivalent plastic strain rate of the *i*-th element in the ferrite, respectively, and N_{el}^{f} denotes the total number of ferrite elements. The average equivalent plastic strain rate of martensite $\left\langle \dot{\varepsilon}_{eq}^{m} \right\rangle$ can be calculated using a similar formula. Note that the deformation is time-independent and then the fraction of plastic strain rate is equivalent to the fraction of plastic strain.

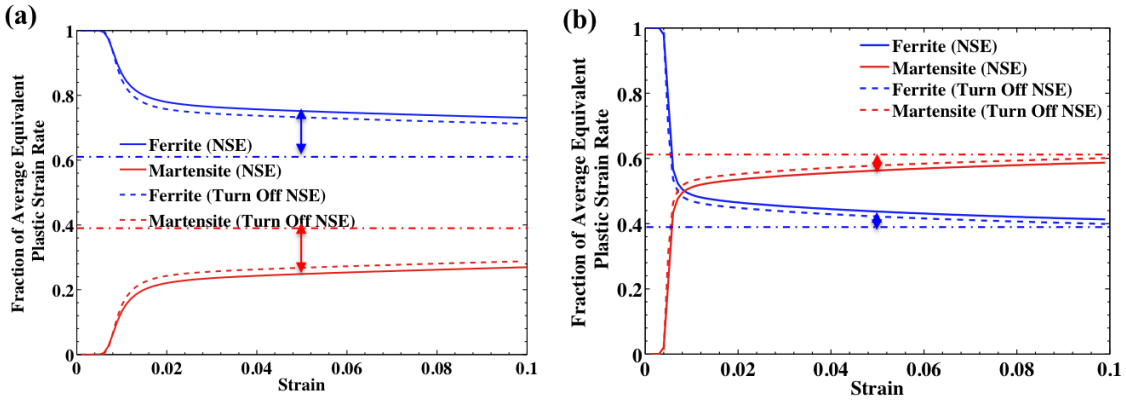

Fig. 4.7 Fraction of average equivalent plastic strain rates in ferrite and martensite phases for (a) DF140T and (b) DP980. Blue and red dash-dot lines are the volume fractions of ferrite and martensite, respectively. In (b) DP980, the plastic strain rate fractions in the two phases match the volume fractions closely (see the length of double-ended arrows in (b)). In contrast, the plastic strain rate fraction in DF140T differs significantly from the volume fractions (see the length of double-ended arrows in (a)). Note that the deformation is time-independent and then the fraction of plastic strain rates is equivalent to the fraction of plastic strain.

In both steels, yield occurs first in ferrite, at a uniaxial stress of approximately 400MPa. This point corresponds approximately to the deviation from linearity in the experimental stress-strain curve. For a brief period (up to a strain of 0.6% in DP980 or 0.4% in DF140T) the ferrite contributes 100% of the total plastic strain. Shortly thereafter (at a stress level of approximately 700MPa), the martensite begins to deform plastically. The onset of plastic flow in the martensite corresponds to the point where a substantial decrease in hardening rate occurs in the macroscopic stress-strain curves. Thereafter, the strain rate partition remains approximately constant in both steels. The fraction of plastic strain rate in DP980 roughly approaches the volume fraction of individual phases, as predicted by a simple Taylor model [117]. In contrast, the plastic strain rate fraction in DF140T differs significantly from the volume fraction (the difference is marked by the double-ended arrows in Fig. 4.7). The deviation from Taylor behavior in DF140T is a consequence of the large difference between the strengths of the martensite and ferrite phases in this material. The deviation can be interpreted to quantify the difference between the actual strain rate in each phase and the imposed macroscopic strain rate, and is thus a measure of the strain incompatibility in the microstructure. The larger strain incompatibility in DF140T may be indirectly related to its lower tensile ductility.

Fig. 4.4 and Fig. 4.7 also show the influence of non-Schmid behavior in the ferrite on the predicted overall tensile flow stress and strain rate partitioning in the two steels. For purposes of comparison, a ‘virtual material’ was created in which the ferrite has the same properties as those of the experimentally calibrated material model, except that non-Schmid behavior was removed by setting $a_1 = a_2 = a_3 = 0$. The uniaxial stress-strain response of this model material is shown as open symbols and dashed lines in Fig. 4.4,

and the strain partition is shown as dashed lines in Fig. 4.7. The effect of non-Schmid behavior in the ferrite is to reduce the tensile strength of both steels. The effect is greater in DF140T than in DP980 due to a higher volume fraction of ferrite in DF140T. The non-Schmid behavior of the ferrite has a number of additional implications. It leads to a small tension-compression asymmetry in the dual phase steels. The strength differential parameter [45] measuring the tension-compression asymmetry is 0.06 in DF140T and 0.012 in DP980. In addition, non-Schmid behavior leads to non-associated flow in a polycrystalline microstructure, which tends to make a material more prone to localization [45]. This may provide a partial explanation for the difference in ductility between the two materials. Both strength differential parameter and non-associated flow will be discussed in detail in the next Section.

In addition to computing the partitioning of strain rates between the two phases of the steels, we have calculated quantitative measures of the stress distribution in their microstructures. Experiments suggest that fracture generally nucleates at the interface between ferrite and martensite in both steels [33]. The stresses acting on these interfaces is therefore of particular interest. To this end, we have estimated the normal and tangential stresses on the ferrite/martensite interfaces in both steels. This calculation is complicated by the rectangular grid used to mesh the microstructures in our computations, and the interfaces follow a zig-zag path along element boundaries rather than conforming to the true geometry of the interface. We have therefore used a procedure similar to that described in Section 2.8 to compute the normal and tangential stress along the interfaces. This procedure has been used to compute histograms of the variation of normal and tangential stresses on the ferrite/martensite interfaces in both steels. The results are

shown in Fig. 4.8. The total areas of the histograms are normalized to unity for both steels, and are shown at the same global strain (10%). The results show that the peak values of the normal stress in DF140T reach 2.4GPa, while in DP980 the maximum normal stress reaches only 1.9GPa. Similarly, both the average and peak shear stresses acting on interfaces in DF140T significantly exceed those in DP980. These differences can be explained by the higher flow stresses of the martensite phase in DF140T, and also provides an addition possible explanation for the lower ductility of DF140T compared with DP980.

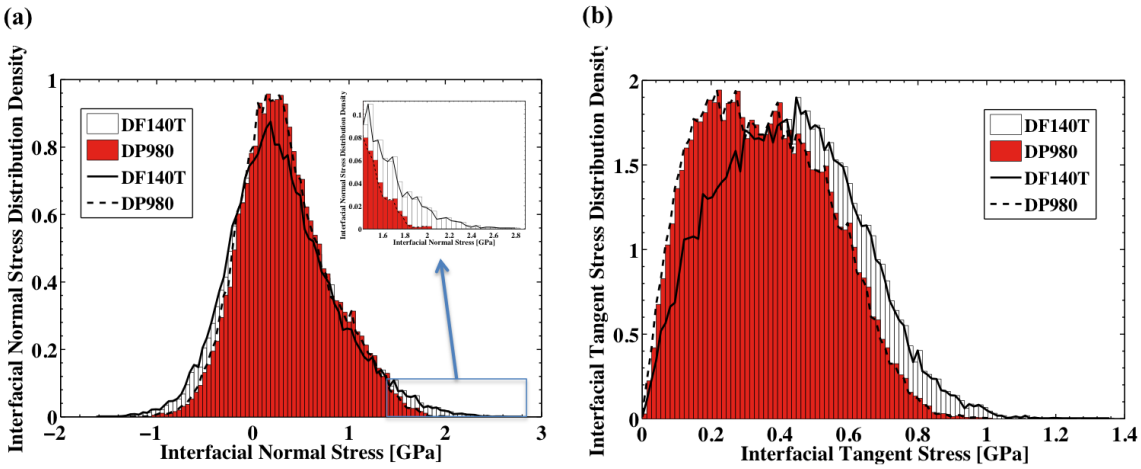

Fig. 4.8 Histograms of (a) interfacial normal and (b) interfacial tangent stress distributions in DF140T and DP980 at 10% global strain. Inset in (a) is the amplified distribution tail region marked by the rectangle.

Similarly, the normal and tangential stresses acting on the prior austenite/packet/block boundaries in both DP steels were also estimated. The same procedure in Section 2.8 has been used to compute histograms of the variation of normal and tangential stresses acting on the prior austenite/packet/block boundaries in both DP steels. The results are shown in Fig. 4.9. The total areas of histograms are normalized to

unity, and are shown at the same global strain (10%). The results show that the normal and tangential stresses acting on prior austenite and block boundaries are similar, while the average normal and tangential stresses acting on prior austenite boundaries are slightly smaller than those on block boundaries. The slight difference between prior austenite and block boundaries might be explained by the uncorrelated crystal orientations between prior austenite grains and correlated K-S orientations between packets or blocks, which is similar to the observation for fully martensitic steel in Section 2.8. Note that there is no packet boundary in the DP RVEs under consideration. In addition, the results show that the peak values of normal stress acting on prior austenite and block boundaries in DF140T reach 3.0GPa, while in DP980 the maximum normal stress acting on prior austenite and block boundaries reaches only 2.4GPa. Similarly, both the average and peak tangential stresses acting on prior austenite and block boundaries in DF140T significantly exceed those in DP980. These differences can be explained by the much higher flow stresses of the martensite phase in DF140T.

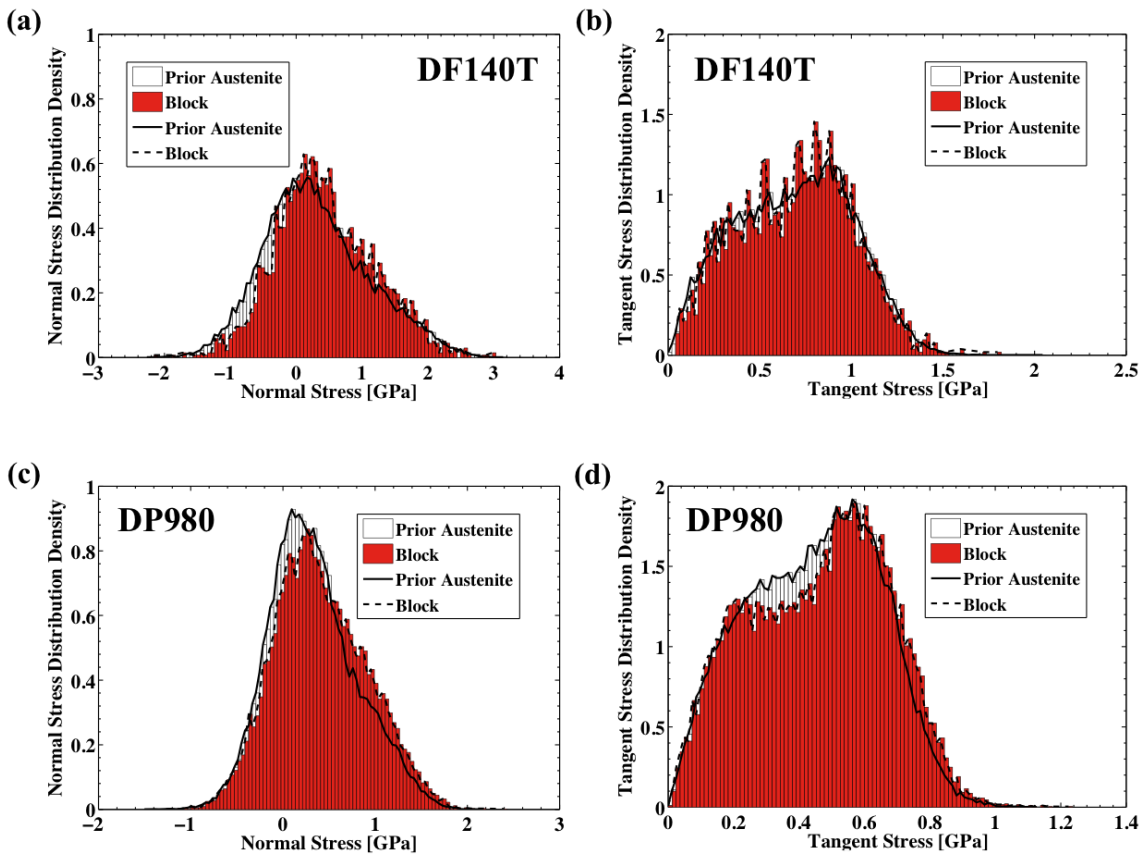

Fig. 4.9 Histograms of (a)/(c) normal and (b)/(d) tangent stress distributions on prior austenite/block boundaries in (a)-(b) DF140T and (c)-(d) DP980 at 10% global strain.

4.4. Non-associated flow in DP steels

The non-Schmid behavior of the ferrite has a number of additional implications. It leads to non-associated plastic flow in the DP steels, which tends to make a material more prone to localization [45]. This may provide a partial explanation for the difference in ductility between the two DP steels DF140T and DP980.

To describe the non-associated plastic flow of DP steels, we adopt a simple coarse-grain constitutive model [45]. The flow potential is the same as the J_2 flow,

$$G = \sqrt{3J_2} \tag{4.4}$$

while the yield function is a function of both second and third invariants of the deviatoric Cauchy stress,

$$F = \frac{3}{(3\sqrt{3}+2b)^{1/3}}\left[(J_2)^{3/2} + bJ_3\right]^{1/3} \tag{4.5}$$

where $J_2 = s_{ij}s_{ij}/2$ and $J_3 = s_{ij}s_{jk}s_{ki}/3$ are the second and third invariants of the deviatoric Cauchy stress, s_{ij}. For this simple coarse-grain constitutive model, the parameter b in the yield function (4.5) is the measure of the non-associated flow. The classical Von Mises yield function can be recovered by setting $b = 0$.

Another measure of non-associated flow, perhaps more intuitive than b, is the strength differential (*SD*) given by,

$$SD = \frac{2(\sigma_T - \sigma_C)}{(\sigma_T - \sigma_C)} = \frac{2[(1-2b/3\sqrt{3})^{1/3} - (1+2b/3\sqrt{3})^{1/3}]}{[(1-2b/3\sqrt{3})^{1/3} + (1+2b/3\sqrt{3})^{1/3}]} \tag{4.6}$$

where σ_T and σ_C are the initial yield stresses in tension and compression, respectively.

Before using the above-mentioned non-associated plastic flow model in DP steels, we need to know the values of b or *SD* in DP steels. The values of b or *SD* can be easily measured by testing the tension and compression yield stresses in Eq. (4.6) in experiments. Due to the shortage of the experimental tests, here we use the micropillar-calibrated RVEs in Section 4.3 to fit the yield function in Eq. (4.5).

The average stresses are calculated along the two planar loading directions (denoted by x and y) in 3D micropillar-calibrated RVEs subjected to multiaxial displacement loading. These average stresses are used to fit the parameter b in Eq. (4.5) (dots in Fig. 4.10). In Fig. 4.10 the yield surfaces (curves in Fig. 4.10) are determined by the Eq. (4.5) using the optimal fitting parameter b. Note that for the rate-dependent

viscoplasticity used in our crystal-plasticity model, there are no true yield surfaces corresponding to stress states that would initiate yielding in a rate-independent material, and the yield surfaces in rate-dependent viscoplasticity are the constant offset effective plastic strain surfaces [118]. It is necessary to show the evolution of yield surfaces with different constant offset effective plastic strain (Fig. 4.10). For each yield surface, one optimal parameter b or SD is obtained by fitting the yield function (4.5) using the average stresses measured from 3D RVEs subjected to multiaxial loading. The evolution of parameter *SD* with the offset effective plastic strain for DP steels DF140T and DP980 is shown in Fig. 4.11. The *SD* value for DF140T is around 4 times larger than the one for DP980. The larger *SD* value makes a material more prone to localization [45]. This may provide a partial explanation for the difference in ductility between the two DP steels DF140T and DP980.

Once the strength differential *SD* values for two DP steels DF140T and DP980 are known, we have the capability to model the macroscopic forming behavior of DP steels using the non-associated flow model. One of the interested things in forming behavior of DP steels is to determine the forming limit strain. We follow the 3D sheet necking finite element model in [45, 46] to predict the forming limit strains in both DP steels.

The material parameters used in the non-associated flow model [45, 46] are listed in Table 4.1. Only the non-associated parameter b or *SD* is different for two DP steels. But the small difference leads to different forming limit strains for these two DP steels. Fig. 4.12 shows the different forming limit strains ($\varepsilon_{cr}^{\mathrm{DF140T}} = 0.02$ for DF140T versus $\varepsilon_{cr}^{\mathrm{DP980}} = 0.029$ for DP980) under a strain path (ρ=-0.2) near the plain strain state using the

3D sheet necking modeling in [46]. Using the 3D sheet necking modeling in [46], we also plot the forming limit diagram under different loading paths (see Fig. 4.13). Compared to associated flow ($b = SD = 0$), the non-associated flow obviously increases or decreases the forming limit strains of DP steels along different loading paths. The deviation of forming limit strains for the non-assocated flow from the associated flow increases with the increasing of strength differential *SD* value. This may also explain why DF140T has less ductility than DP980 since the *SD* value in DF140T is larger due to a higher volume fraction of ferrite.

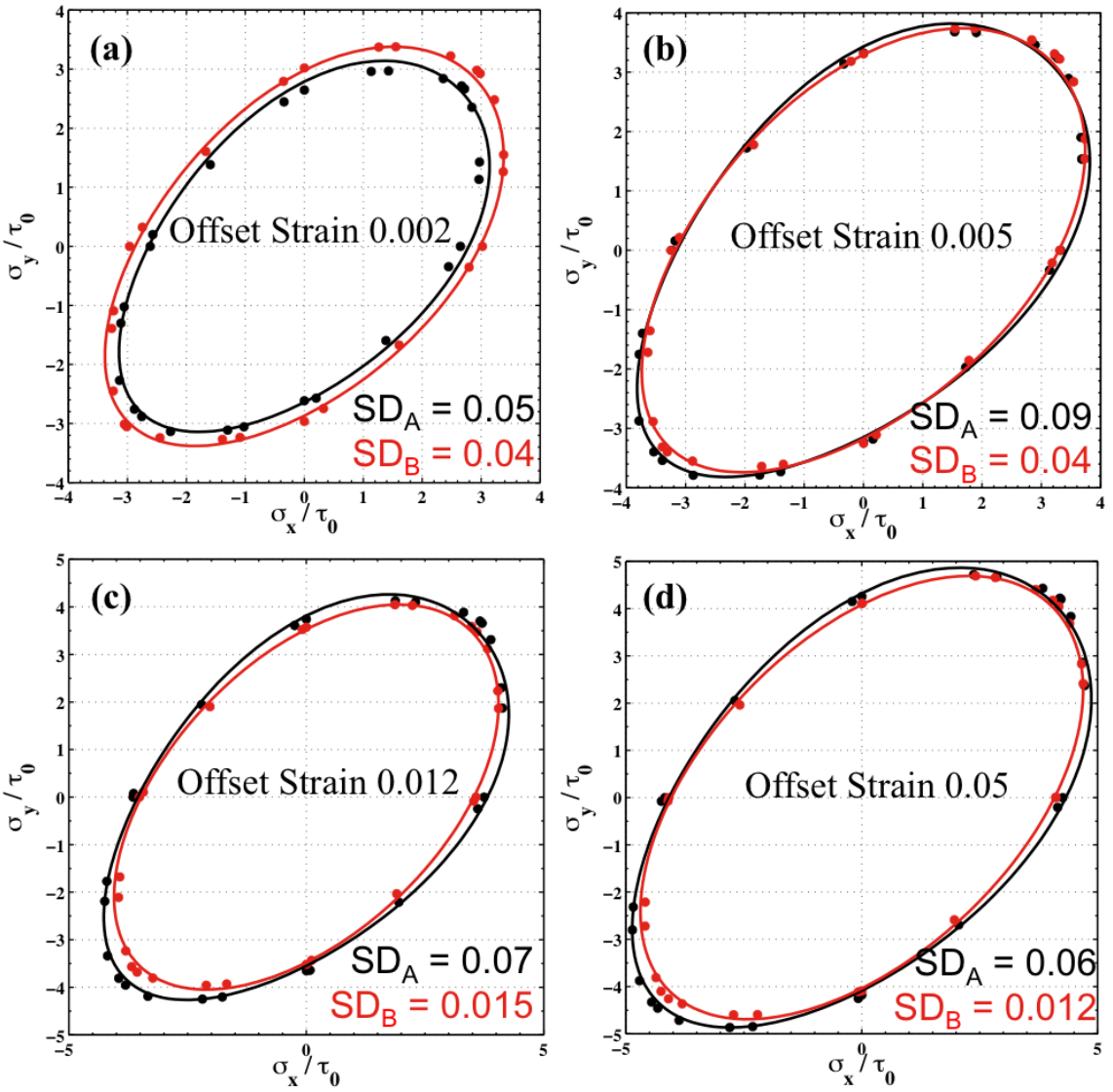

Fig. 4.10 Yield surfaces with different offset effective plastic strains (a) 0.2%, (b) 0.5%, (c) 1.2% and (d) 5%. The dots are calculated from 3D micropillar-calibrated RVEs and curves are obtained from the non-associated yield function in Eq. (4.5) using the optimal fitting parameter b. Black dots and curves denote DF140T, and red dots and curves denote DP980. SD_A and SD_B denote the strength differential values of DF140T and DP980, respectively.

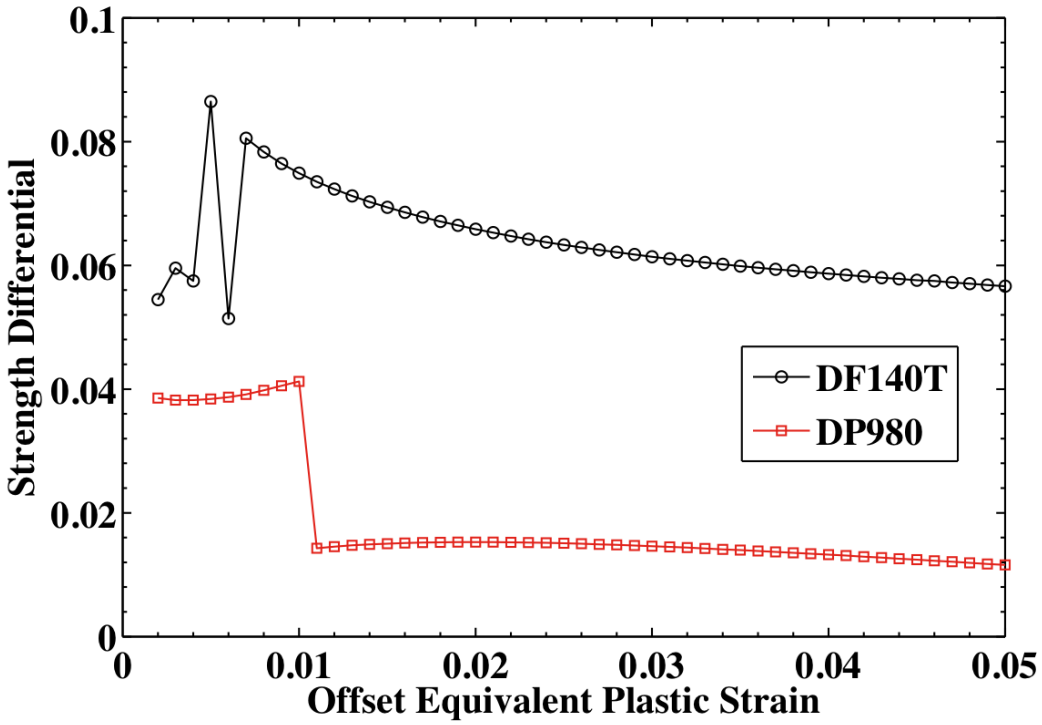

Fig. 4.11 Evolution of strength differential *SD* value with the offset equivalent plastic strain for DP steels DF140T and DP980.

Table 4.1 Material parameters used in 3D sheet necking finite element model in reference [45].

Two commercial DP steels	DF140T	DP980
Young's modulus (MPa)	2.1E5	
Poisson ratio	0.3	
Strain rate $\dot{\phi}_0$ (s^{-1})	1.0	
Exponent m	0.0002	
Initial hardening stress σ_0 (MPa)	675.0	
Characteristic plastic strain ε_0	0.001	
Hardening exponent n	20.0	
Non-associated parameter b	-0.273	-0.058

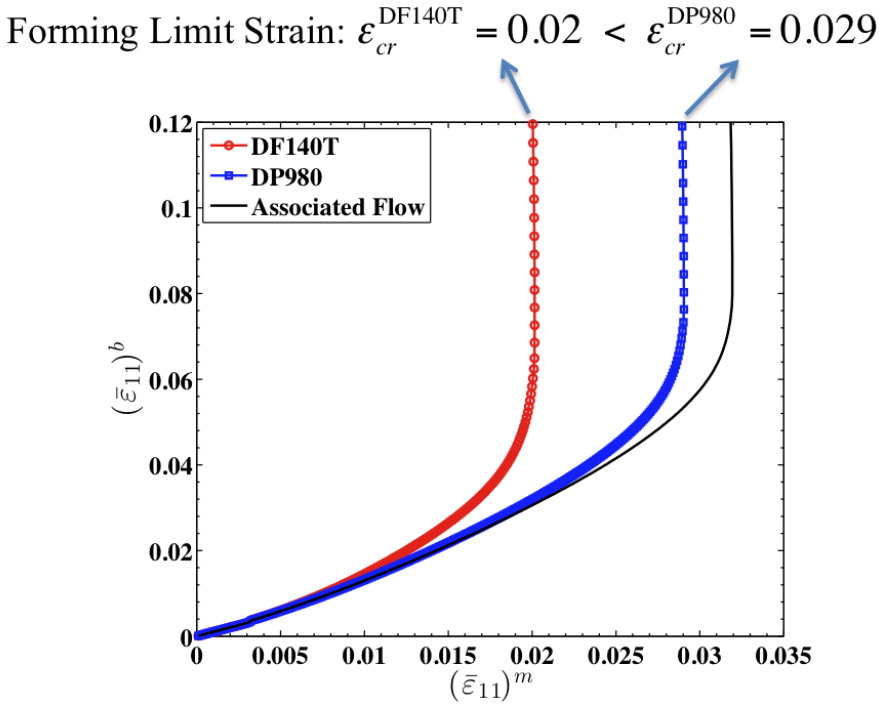

Fig. 4.12 Average logrithmic strain $\left(\bar{\varepsilon}_{11}\right)^b$ in band vs average logrithmic strain $\left(\bar{\varepsilon}_{11}\right)^m$ in matrix using the non-associated plastic flow model [45] with the specific loading path ρ=-0.2. Associated flow behavior is also included by setting parameter $b=0$. $\varepsilon_{cr}^{DF140T}$ and ε_{cr}^{DP980} denote forming limit strains for DF140T and DP980, respectively.

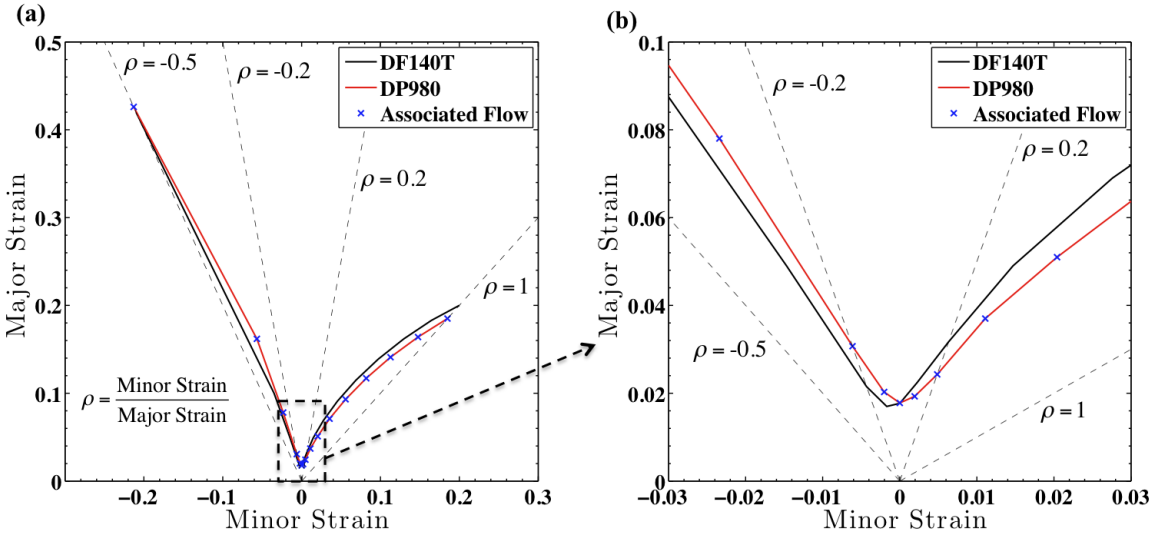

Fig. 4.13 (a) Forming limit diagram for both DP steels using the non-associated plastic flow model [45]. The amplified region denoted by the dashed rectangle in (a) is shown in (b). Different ρ denote different loading paths.

Chapter 5. Mechanical Behavior of Active Biopolymer Networks

In the preceding Chapters, we have discussed the nonlinear mechanical behavior of hard AHSS (Young's modulus ~ 200 GPa). In this Chapter, we will study the nonlinear deformation behavior of active biopolymer networks, which is extremely softer (Young's modulus ~ 1 Pa [59]) compared to hard AHSS. The distinct deformation mechanisms of active biopolymer networks also lead to the different nonlinear deformation behavior, known as the strain stiffening behavior, which will be discussed in Section 5.2. Before the discovery of the nonlinear strain stiffening behavior of active biopolymer networks using finite element method, the construction of 2D active biopolymer networks will be described in Section 5.1.

5.1. Construction of active biopolymer networks

The biopolymer networks considered in our study are constructed as follows. Straight filaments of length $L = 10$ μm (comparable to the actin filament lengths of ~10–15 μm [59]) and random orientations are assembled in a square box of width $W = 40$ μm. When two filaments cross each other, they are connected by a nonlinear spring (to be described below) or are linked rigidly. Filaments that cross the top and bottom boundary are cut and the dangling ends are removed, while periodic boundary conditions are imposed along the lateral boundaries. The system is loaded by restricting the horizontal displacements of the nodes of the filaments at the top and bottom of the box to γW and

zero, respectively, where γ is the applied shear strain. We assume that the polymer filaments that make up our network are semiflexible, so that the persistence length of the individual chains is much longer than the average distance between the two crosslink sites, and comparable to the contour length of individual polymer chains. Therefore we ignore thermal energy arising from fluctuation of the filaments and consider only the extensional and bending energies of the filaments. Using κ and μ to denote bending modulus and stretching modulus of F-actin, respectively, we choose μ/L = 1.6 MPa and $\sqrt{\kappa/(\mu L^2)} = 2.3\times10^{-4}$ (both representative of F-actin networks [50, 55]). The normalized line density of our network ($\bar{\rho} = L_T L / W^2$, where L_T is the total length of filaments in the cell) is $\bar{\rho} = 12.5$, which is well above the rigidity percolation threshold of $\bar{\rho} = 5.7$ [119].

The contour length of FLNa is $l_0 \approx 150\, nm$ [58, 59] and its persistence length is $l_p \sim 20\, nm$ [52, 59]. For stretches less than the contour length, this crosslink behaves like a linear spring with spring constant $k_{cl} = 2k_B T/(3l_p l_0)$ [120], where $k_B T = 4.11\, pN \cdot nm$. When stretched beyond its contour length l_0, the stiffness of the crosslink increases very rapidly [56, 57]. Following the work of Broedersz *et al.* [56, 57], we therefore model the crosslinks as piecewise linear springs such that the force $F = -k\Delta l$, where $k = k_{\mathrm{cl}}$ for length $\Delta l < l_0$, while $k \gg k_{\mathrm{cl}}$ when $\Delta l > l_0$, where Δl is the extension of the crosslink. Scruin crosslinks on the other hand are inextensible [52]. Very recent measurement shows that force applied by a single skeletal myosin head on an F-actin is in the range 1 pN–5 pN [121]. Myosin is typically assembled into thick filaments with several heads; the filaments typically have lengths of $\sim$1 μm [59, 122]. To model the contractile force

generated by the motors we model them as force dipoles as shown schematically in Fig. 1.6. In our simulations, the motors are assembled by picking a point at random on a filament and then picking another point located on a neighboring filament such that the distance of the two points lies in the range of 0.5–2 μm. A typical force of 10 pN is applied along the line connecting the two points to simulate the pulling effect of the motors as shown in Fig. 1.6.

5.2. Finite element modeling

The elastic fields in the sheared filament network are computed using commercial finite element software ABAQUS v6.8, discretizing each filament with 100 equal-sized Timoshenko beam elements (B21). All simulations are carried out in a finite deformation setting; *i.e.*, the effect of geometry changes on force balance and rigid body rotations are explicitly taken into account. The macroscopic shear stress τ for our model is the total horizontal reaction force at the top of the simulation box divided by W. The dimensionless stress $\bar{\tau}$ in Fig. 5.1 is defined as $\bar{\tau} = \tau L / \mu$, and the modulus $\bar{K}' = d\bar{\tau} / d\gamma$. To gain insight into different deformation mechanisms, we also compute the total energy associated with stretching of the crosslinks in the cell, E_c, the total bending energy of all the filaments, E_b, and the sum of the bending and stretching energies or the total strain energy of all the filaments, E_f. We first consider the case where there are no motors present and the crosslinks are either rigid (black dashed lines in Fig. 5.1 and Fig. 5.2) or compliant (black solid lines in Fig. 5.1 and Fig. 5.2). As in earlier work [56, 57], the modulus in the latter case shows a sharp increase when the crosslinks are fully stretched and enter the hardened regime (note that 3D simulations show similar

results [54]). It can be seen from Fig. 5.2 that below this threshold the total energy of the network is dominated by the energy of stretching the crosslinks, but above this threshold the filaments first bend and then stretch. In the case of rigid crosslinks, for small strains, the deformation of the network is dominated by bending of the filaments followed by stretching and orientation of the filaments along the direction of shearing. Note that at very large applied strains, both the networks show identical response due to stretching of the filaments.

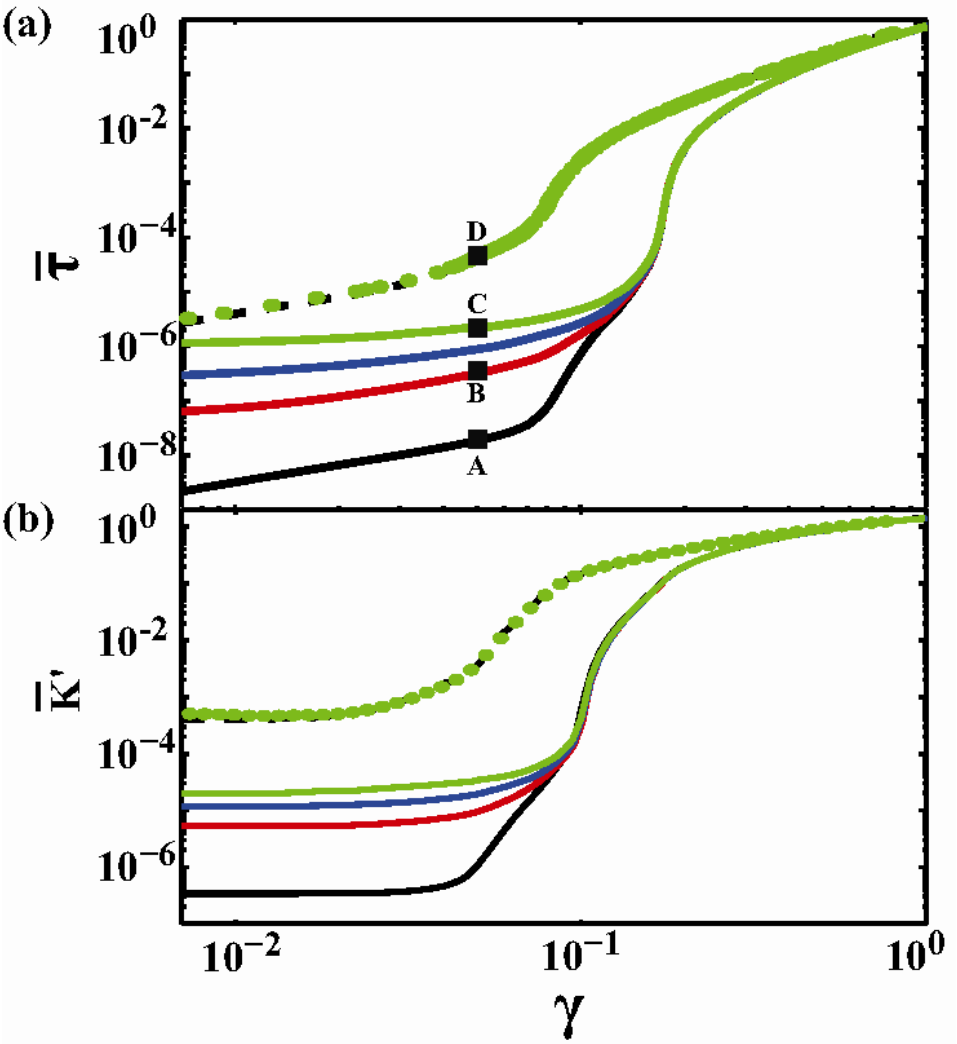

Fig. 5.1 Stress ($\bar{\tau}$) and differential shear stiffness ($\overline{K'}$) *vs* shear strain (γ) for active F-actin network with rigid or compliant crosslinks. The myosin motors only stiffen the F-actin network with rigid crosslinks by a factor of 1.4 at small strains: network without myosin motor (black dashed line) and N_m/N_{actin} = 6.4 (green circles). However the myosin motors stiffen the flexibly crosslinked F-actin network up to a factor of 70: network without myosin motors (black solid line), with N_m/N_{actin} = 0.9 (red solid line), with N_m/N_{actin} = 3.1 (blue solid line), and with N_m/N_{actin} = 6.4 (green solid line). N_m and N_{actin} correspond to the total number of motors and filaments, respectively. Each motor exerts a force of 10 pN on the actin filament.

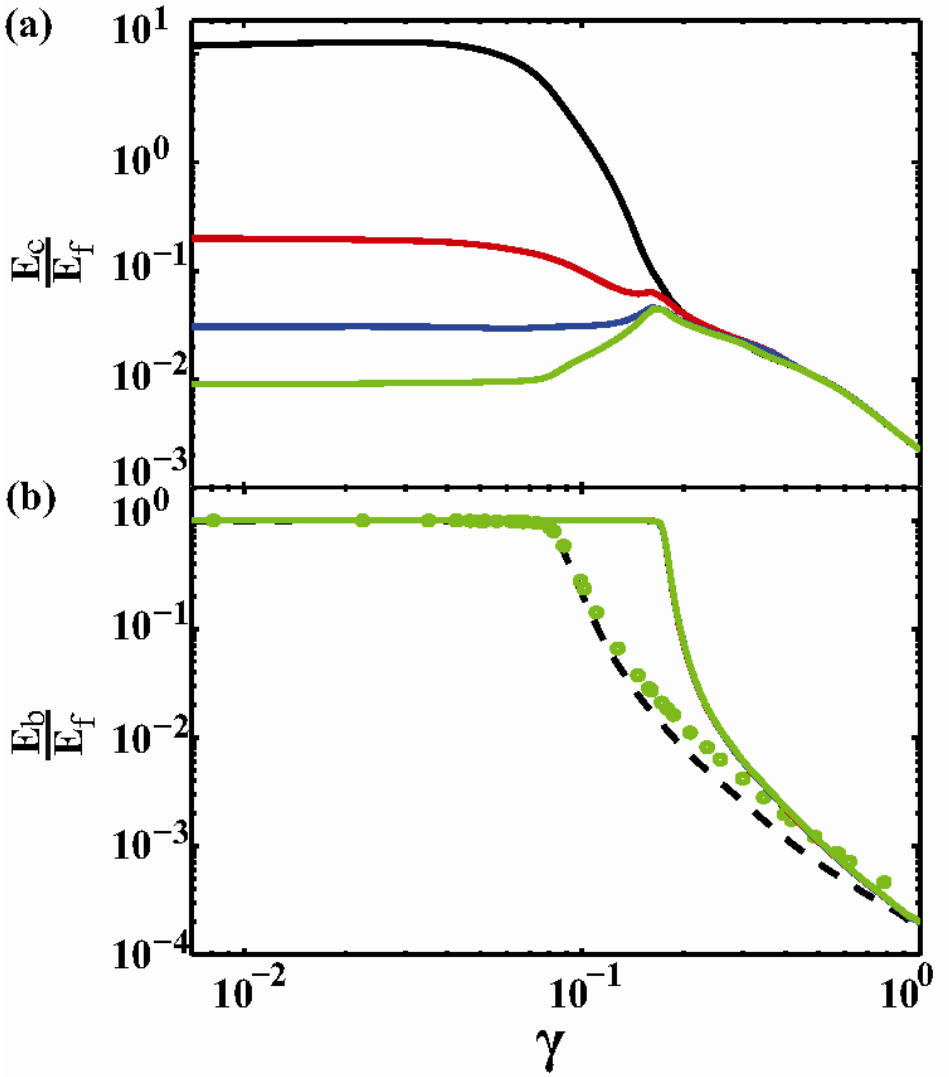

Fig. 5.2 (a) The ratio of total stretching energy (E_c) of compliant crosslinks to total energy (E_f) of filaments in the system, and (b) the ratio of total bending energy (E_b) of the filaments in the system to total strain energy of all the filaments (E_f) as a function of shear strain (γ). At small strains, the rigidly crosslinked F-actin network is dominated by bending of F-actin , regardless of whether myosin motors are present (green circles) or absent (black dashed line). However, myosin motors drive the deformation from stretching of the crosslinks to bending of F-actin as evidenced by the decrease in the ratio E_c/E_f from the case with no motors (black solid line), to the cases with increasing contractile forces (not plotted here) or motor densities (N_m/N_{actin} = 0.9 (red solid line), N_m/N_{actin} = 3.1 (blue solid line), and N_m/N_{actin} = 6.4 (green solid line)). All flexibly crosslinked F-actin networks with or without myosin motors show nearly identical behavior of the ratio E_b/E_f (green solid line in (b)).

Next we consider the response of the network with compliant crosslinks in the presence of motors. At small strains, Fig. 5.1 shows that the networks continuously

stiffen with increasing density of motors. Even with one motor per filament, the stiffness of the network increases by over one order of magnitude. Networks with about six motors per filament are stiffer than the networks without motors by about two orders of magnitude. To understand the reason for this marked increase in stiffness, we consider (a) the ratios of energies associated with different deformation modes (Fig. 5.2), (b) the distributions of the lengths of the crosslinks (Fig. 5.3) and c) the shapes of the deformed filaments (Fig. 5.4). Fig. 5.2 shows that even at small applied strains, the ratio of the total energy of the crosslinks to the total strain energy of all the filaments decreases significantly with increasing motor density. Indeed, the histogram of crosslink extensional lengths in Fig. 5.3 confirms that the motors are able to induce stretching of almost all the crosslinks to their contour length, l_0, beyond which it is difficult to stretch them. This causes bending of the filaments, which explains the decrease in the ratio of the total energy of stretching of crosslinks to the total energy of the filaments, E_c/E_f, with increase in the density of motors. Upon application of a small external load, the deformation is primarily borne by the bending of the filaments leading to stiffer response compared to the case where motors are absent. The dominance of the bending modes is clearly seen in Fig. 5.4: for small applied strain of 0.05, the filaments in the network without motors are straight whereas significant bending of the filaments can be seen in the network with motors. Also note from Fig. 5.3 that most of the crosslinks in the former case have not been stretched to the maximum extent. As the applied strain is large ($\sim$0.3), in all cases there is a transition in the deformation modes of the filaments from bending to stretching, at which point the response of all the networks is identical.

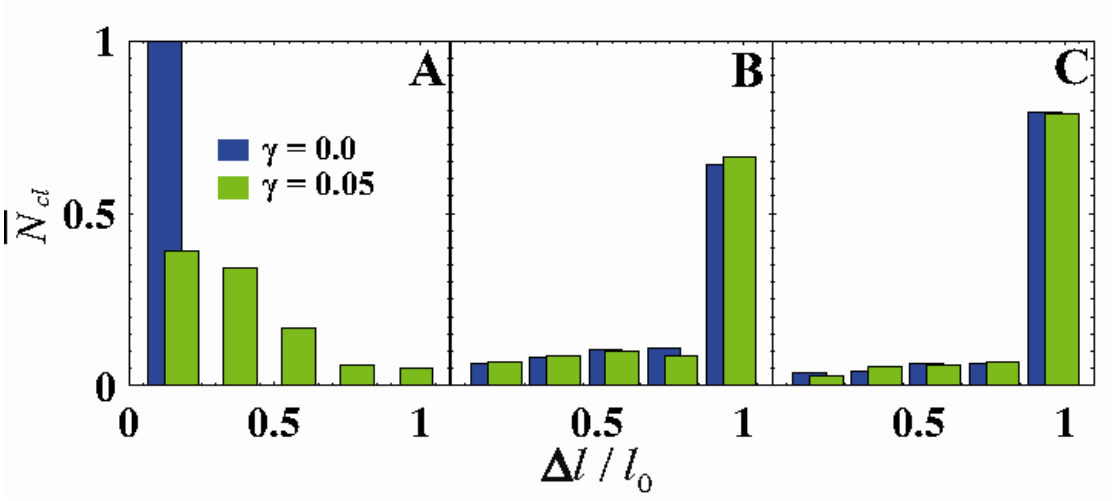

Fig. 5.3 Distribution of the extension of the crosslinks Δl relative to their contour length l_0 at shear strains $\gamma = 0$ (blue) and $\gamma = 0.05$ (green). $\bar{N}_{cl}$ is the number of crosslinks normalized by the total number of crosslinks in the active network. The symbols A–C corresponded to the black squares given in Fig. 5.1. In B and C myosin motors drive most compliant crosslinks up to contour lengths, l_0, whereas when no motors are present (A), the crosslinks have not been stretched to their fullest extent. Note that more crosslinks are stretched to their contour lengths in C than in B owing to the larger motor density in the former case.

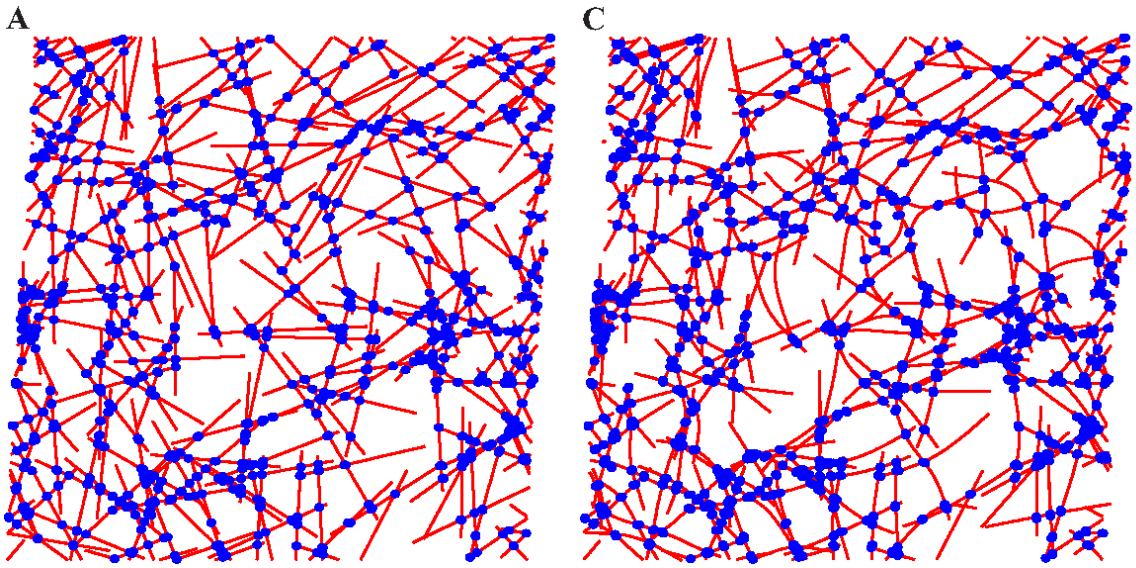

Fig. 5.4 The deformation of F-actin network corresponding to the points A and C in Fig. 5.1. Deformation is dominated by stretching of compliant crosslinks (A) or bending of flexibly crosslinked F-actin (C). Red lines are actin filaments and blue dots indicate the location of crosslinks.

In contrast to the filaments with compliant crosslinks, the stress-strain curves and the incremental moduli of networks with rigid crosslinks are not significantly altered by the presence of motors. Indeed, we find only an increase close to a factor of two in the modulus of the network at small strains. We can understand this by noting that the filaments in rigidly crosslinked networks deform primarily through bending. The motors do not qualitatively change this picture. The effect of the motors on bending deformation is small unlike the large change in the lengths of the crosslinks that they induce in the case of compliant networks. Our calculations therefore provide an explanation for the key role played by the nature of the crosslinks on the mechanical response of active networks.

It is well known that in uncrosslinked networks the myosin filaments effectively fluidize actin networks by actively sliding antiparallel actin filaments past one another, which can lead to large scale reorganization of the network. However in a crosslinked network, upon addition of myosin, there was no noticeable change in network structure [59]. When myosin and FLNa were both present, the network still remained homogeneous and unbundled suggesting that relative sliding between the motors and filaments is relatively small, which justifies the treatment of the motors as force dipoles. It is also possible that myosin-driven tension may release FLNa crosslinking. Also, scruin can inhibit myosin binding. These issues, the effect of potential sliding and perhaps the stretching of myosin motors themselves can be considered in future work using the model we have developed here.

5.3. Conclusions

In summary, by using material parameters typical for actin networks with compliant crosslinks, we have shown that myosin II motors generate internal stresses by stretching the crosslinks which in turn pull on the actin filaments. Once the crosslinks are fully stretched to their contour lengths, the differential stiffness of the network can increase by two orders of magnitude in excellent agreement with recent experiments [59]. In addition, our simulations show that motors do not lead to any significant stiffening in the response of rigidly crosslinked networks, also in accord with experiments [59]. These observations underscore the importance of the nature of crosslinks on determining the strain hardening behavior of active networks and provide guidelines for tuning mechanical response of biomimetic systems.

Chapter 6. Conclusions and Future Work

6.1. Conclusions

The nonlinear deformation response of two distinct materials is studied using finite element simulations in the dissertation. One is the hard AHSS widely used in automobile vehicles and its nonlinear mechanism of plastic deformation is due to dislocations. Another is soft active biopolymer networks in plant and animal cells and its nonlinear mechanism of deformation is due to the deformation mode transition from bending to stretching.

For the hard AHSS, our proposed approach in Section 1.2 has successfully modeled the deformation response of two types of AHSS: fully martensitic steels and DP steels. The combination of micropillar compression experiments and microstructure-based crystal plasticity finite element simulations accurately determined the material properties of lath martensite and ferrite in AHSS and predicted the overall flow behavior of both types of AHSS.

The measured flow curves for martensite micropillars with diameters exceeding 2.0 μm can be used to determine material parameters in a dislocation-density-based crystal plasticity model of individual martensite blocks. Numerical simulations confirm that hardening behavior can be attributed to the geometric constraints arising from boundaries between blocks. Boundaries between blocks in two separate packets were found to give rise to greater strain hardening than those between blocks within a single

packet. Full 3D crystal plasticity simulations, with material properties determined from martensite micropillar tests, were then used to predict the macroscopic uniaxial stress–strain behavior of a representative volume element of martensite. The predicted stress–strain behavior is in excellent agreement with experimental measurements, and validates the use of micropillar tests to determine material parameters for individual phases of a complex microstructure. The similar stress distributions on prior austenite/packet/block boundaries are also predicted.

Using the same approach described in Section 1.2, the constitutive behavior, uniaxial tensile response, strain partitioning and interfacial stress distributions in two commercial DP steels, DP980 and DF140T, have also been determined.

The crystallographic orientation dependence of the flow strength in the ferritic phases is predicted successfully by a crystal plasticity model that accounts for the non-Schmid behavior commonly exhibited by BCC single crystals. Classical models based on Schmid's law do not predict the orientation dependence correctly.

The compressive response of micropillars extracted from the martensite phases of the two DP steels is qualitatively similar to behavior observed in fully martensitic steel. The pillars exhibit either elastic-perfectly plastic behavior, or a strain hardening response, depending on whether the pillars consist of a single block or block/packet boundary. The dislocation-density-based crystal plasticity model that accounts for the hierarchical microstructure of martensite also predicts behavior in the martensite micropillars milled from DP steel sheets that is in good agreement with experiment.

A 3D computational representation of the microstructures of the DP steels, in which crystal plasticity models (calibrated by micropillar experiments) were used to

describe both the ferritic and martensitic phases, predicts uniaxial tensile stress-strain curves that are in excellent agreement with experiment. Computations show that features observed in the uniaxial tensile stress-strain curves can be explained by changes in strain partitioning in the steels with increasing strain. First yield occurs in the ferrite at 400MPa. The period of rapid strain hardening between 400MPa and 700MPa is associated with continued deformation in the ferrite, while the martensite remains elastic. Above 700MPa, the martensite yields, leading to a reduction in strain hardening rate. Beyond this point, the strain partitioning between ferrite and martensite remains approximately constant in both steels. Further strain hardening in the steady-state regime is produced primarily by the martensite.

The strain rate partitioning in the two DP steels during steady-state uniaxial tensile deformation differs significantly. In DP980, the contribution to the total plastic strain rate from martensite and ferrite roughly follows the individual volume fractions as predicted by a Taylor model; while in DF140T, martensite contributes only 25% of the total strain rate, which is much less than its volume fraction of 39%.

The non-Schmid behavior observed in ferrite leads to a 9% reduction in the flow strength of DF40T and 5% reduction in the flow strength of DP980. The strength differential parameter measuring the tension-compression asymmetry is 0.06 in DF140T and 0.012 in DP980. The forming limit strain under a specific loading path (ρ=-0.2) near the plane strain state is 0.02 in DF140T and 0.029 in DP980. The difference results from the higher volume fraction of ferrite in DF140T. The non-associated flow obviously increases or decreases the forming limit strains of DP steels along different loading paths.

The deviation of forming limit strains for the non-associated flow from the associated flow increases with the increasing of strength differential *SD* value.

For the soft active biopolymer networks, using material parameters typical for actin networks with compliant crosslinks, we have shown that myosin II motors generate internal stresses by stretching the crosslinks which in turn pull on the actin filaments. Once the crosslinks are fully stretched to their contour lengths, the differential stiffness of the network can increase by two orders of magnitude in excellent agreement with recent experiments. In addition, our simulations show that motors do not lead to any significant stiffening in the response of rigidly crosslinked networks, also in accord with experiments. These observations underscore the importance of the nature of crosslinks on determining the strain hardening behavior of active networks and provide guidelines for tuning mechanical response of biomimetic systems.

6.2. Future work

In light of the work in the dissertation, several directions might be investigated in the future.

1. Eliminating the stepped interface shape of 3D RVEs due to the brick elements and remeshing the interfaces. The grain and phase boundaries in 3D RVEs are stepped shape due to brick elements. The artificial interfacial shapes should be eliminated in the future. One possible solution is to use the open-source software *neper* [123, 124] to reconstruct the 3D RVEs.
2. Using the cohesive zone model to investigate decohesion along ferrite/martensite phase boundaries. It has been shown that most crack initiate

and/or propagate along the ferrite/martensite phase boundaries [24, 27]. The 3D RVEs will have the capability to predict the failure and fraction behavior of multiphase steels if the stepped interfaces are smoothed.

3. Introducing the austenite-to-martensite transformation mechanism into the crystal-plasticity models and predicting the plastic deformation of TRIP steels. The combination of micropillar compression tests and crystal-plasticity finite element model has been successfully used to predict the overall uniaxial stress-strain curves of fully martensite steel and DP steels. The approach might be extended to predict the mechanical properties of more complex AHSS, for example, TRIP steels.
4. Measuring the strength differential value of lath martensite phase. Designing experiments to test whether the studied lath martensite exhibits the strength differential effect should be done in the future.
5. Investigating the viscoelastic behavior of active biopolymer networks. The reconstructing of the cellular microstructures is facilitated by employing transiently cross-linking proteins. It is yet to be resolved how transiently cross-linking proteins affect the frequency response of cross-linked actin networks in the elasticity dominated intermediated frequency regime [60, 125-128]. Including the binding/unbinding behavior of transient cross-linking protein and using kinetic connect elements in ABAQUS might predict the viscoelastic behavior of the active biopolymer networks.

References

[1] Senuma T. Preface to the Special Issue on "Cutting Edge of Mathematical Models for Predicting Microstructures and Mechanical Properties of Steels". Isij International 2012;52(4):539-539.

[2] Powers WF. Advanced Materials and Processes May 2000:38-41.

[3] Zavattieri PD, Savic V, Hector LG, Fekete JR, Tong W and Xuan Y. Spatio-temporal characteristics of the Portevin-Le Chatelier effect in austenitic steel with twinning induced plasticity. International Journal of Plasticity 2009;25(12):2298-2330.

[4] Mishra SK, Tiwari SM, Kumar AM and Hector LG. Effect of Strain and Strain Path on Texture and Twin Development in Austenitic Steel with Twinning-Induced Plasticity. Metallurgical and Materials Transactions a-Physical Metallurgy and Materials Science 2012;43A(5):1598-1609.

[5] De Moor E, Gibbs PJ, Speer JG and Matlock DK. Strategies for third generation advanced high strength steel development. AIST Trans. 2010;7(3):133 - 144.

[6] Matlock DK, Speer JG, De Moor E and Gibbs PJ. Recent Developments in Advanced High Strength Sheet Steels for Automotive Applications: an overview. JESTECH 2012;15(1):1 - 12.

[7] Consortium U-A (2002) ULSAB-AVC Advanced Vehicle Concepts Overview Report. (http://www.autosteel.org/~/media/Files/Autosteel/Programs/ULSAB-AVC/avc_overview_rpt_complete.pdf).

[8] Mazinani M and Poole WJ. Effect of martensite plasticity on the deformation behavior of a low-carbon dual-phase steel. Metallurgical and Materials Transactions a-Physical Metallurgy and Materials Science 2007;38A(2):328-339.

[9] Sun X, Choi KS, Liu WN and Khaleel MA. Predicting failure modes and ductility of dual phase steels using plastic strain localization. International Journal of Plasticity 2009;25(10):1888-1909.

[10] Krauss G. Martensite in steel: strength and structure. Materials Science and Engineering a-Structural Materials Properties Microstructure and Processing 1999;273:40-57.

[11] Krauss G and Marder AR. MORPHOLOGY OF MARTENSITE IN IRON ALLOYS. Metallurgical Transactions 1971;2(9):2343-&.

[12] Das SK and Thomas G. ON MORPHOLOGY AND SUBSTRUCTURE OF MARTENSITE. Metallurgical Transactions 1970;1(1):325-&.

[13] Iwashita K, Murata Y, Tsukada Y and Koyama T. Formation mechanism of the hierarchic structure in the lath martensite phase in steels. Philosophical Magazine 2011;91(35):4495-4513.

[14] Morito S, Yoshida H, Maki T and Huang X. Effect of block size on the strength of lath martensite in low carbon steels. Materials Science and Engineering a-Structural Materials Properties Microstructure and Processing 2006;438:237-240.

[15] Ghassemi-Armaki H, Chen P, Bhat S, Sadagopan S, Kumar S and Bower A. Microscale-calibrated modeling of the deformation response of low-carbon martensite. Acta Materialia 2013;61(10):3640-3652.
[16] Morito S, Tanaka H, Konishi R, Furuhara T and Maki T. The morphology and crystallography of lath martensite in Fe-C alloys. Acta Materialia 2003;51(6):1789-1799.
[17] Choi KS, Liu WN, Sun X and Khaleel MA. Influence of Martensite Mechanical Properties on Failure Mode and Ductility of Dual-Phase Steels. Metallurgical and Materials Transactions a-Physical Metallurgy and Materials Science 2009;40A(4):796-809.
[18] Asgari SA, Hodgson PD, Yang C and Rolfe BF. Modeling of Advanced High Strength Steels with the realistic microstructure-strength relationships. Computational Materials Science 2009;45(4):860-866.
[19] Ramazani A, Mukherjee K, Quade H, Prahl U and Bleck W. Correlation between 2D and 3D flow curve modelling of DP steels using a microstructure-based RVE approach. Materials Science and Engineering: A 2013;560(0):129-139.
[20] Bouquerel J, Verbeken K and de Cooman BC. Microstructure-based model for the static mechanical behaviour of multiphase steels. Acta Materialia 2006;54(6):1443-1456.
[21] Estrin Y and Mecking H. A unified phenomenological description of work hardening and creep based on one-parameter models. Acta Metallurgica 1984;32(1):57-70.
[22] Mecking H and Kocks UF. Kinetics of flow and strain-hardening. Acta Metallurgica 1981;29(11):1865-1875.
[23] Gladman T, Mclvor ID and Pickering FB. Some aspects of the structure-property relationships in hihg-carbon ferrite-pearlite steels. J. Iron Steel Inst 1972;210(12):916-930.
[24] Kadkhodapour J, Butz A, Ziaei-Rad S and Schmauder S. A micro mechanical study on failure initiation of dual phase steels under tension using single crystal plasticity model. International Journal of Plasticity 2011;27(7):1103-1125.
[25] Kim JH, Kim D, Barlat F and Lee MG. Crystal plasticity approach for predicting the Bauschinger effect in dual-phase steels. Materials Science and Engineering a-Structural Materials Properties Microstructure and Processing 2012;539:259-270.
[26] Woo W, Em VT, Kim EY, Han SH, Han YS and Choi SH. Stress-strain relationship between ferrite and martensite in a dual-phase steel studied by in situ neutron diffraction and crystal plasticity theories. Acta Materialia 2012;60(20):6972-6981.
[27] Choi SH, Kim EY, Woo W, Han SH and Kwak JH. The effect of crystallographic orientation on the micromechanical deformation and failure behaviors of DP980 steel during uniaxial tension. International Journal of Plasticity 2013;45:85-102.
[28] Hatem TM and Zikry MA. Dynamic shear-strain localization and inclusion effects in lath martensitic steels subjected to high pressure loads. Journal of the Mechanics and Physics of Solids 2010;58(8):1057-1072.
[29] Hatem TM and Zikry MA. Shear pipe effects and dynamic shear-strain localization in martensitic steels. Acta Materialia 2009;57(15):4558-4567.

[30] Kim JH, Lee MG, Kim D, Matlock DK and Wagoner RH. Hole-expansion formability of dual-phase steels using representative volume element approach with boundary-smoothing technique. Materials Science and Engineering: A 2010;527(27–28):7353-7363.

[31] Uthaisangsuk V, Prahl U and Bleck W. Stretch-flangeability characterisation of multiphase steel using a microstructure based failure modelling. Computational Materials Science 2009;45(3):617-623.

[32] Choi KS, Liu WN, Sun X and Khaleel MA. Micro structure-based constitutive modeling of TRIP steel: Prediction of ductility and failure modes under different loading conditions. Acta Materialia 2009;57(8):2592-2604.

[33] Kadkhodapour J, Butz A and Rad SZ. Mechanisms of void formation during tensile testing in a commercial, dual-phase steel. Acta Materialia 2011;59(7):2575-2588.

[34] Shanthraj P and Zikry MA. Dislocation-density mechanisms for void interactions in crystalline materials. International Journal of Plasticity 2012;34:154-163.

[35] Shi J, Turteltaub S and Van der Giessen E. Analysis of grain size effects on transformation-induced plasticity based on a discrete dislocation-transformation model. Journal of the Mechanics and Physics of Solids 2010;58(11):1863-1878.

[36] Morito S, Huang X, Furuhara T, Maki T and Hansen N. The morphology and crystallography of lath martensite in alloy steels. Acta Materialia 2006;54(19):5323-5331.

[37] Tsipouridis P, Koll L, Krempaszky C and Werner E. On the strength of grain and phase boundaries in ferritic-martensitic dual-phase steels. International Journal of Materials Research 2011;102(6):674-686.

[38] Filippone R, Root J, Jacques P and Yue S. The influence of martensite on line broadening in neutron diffraction spectra of a DP steel. Isij International 2002;42(3):304-309.

[39] Cong ZH, Jia N, Sun X, Ren Y, Almer J and Wang YD. Stress and Strain Partitioning of Ferrite and Martensite during Deformation. Metallurgical and Materials Transactions a-Physical Metallurgy and Materials Science 2009;40A(6):1383-1387.

[40] Jia N, Cong ZH, Sun X, Cheng S, Nie ZH, Ren Y, Liaw PK and Wang YD. An in situ high-energy X-ray diffraction study of micromechanical behavior of multiple phases in advanced high-strength steels. Acta Materialia 2009;57(13):3965-3977.

[41] Nix WD and Gao H. Indentation size effects in crystalline materials: A law for strain gradient plasticity. Journal of the Mechanics and Physics of Solids 1998;46(3):411-425.

[42] Stewart JL, Jiang L, Williams JJ and Chawla N. Prediction of bulk tensile behavior of dual phase stainless steels using constituent behavior from micropillar compression experiments. Materials Science and Engineering a-Structural Materials Properties Microstructure and Processing 2012;534:220-227.

[43] Chen P, Ghassemi-Armaki H, Kumar KS, Bower AF, Bhat S and Sadagopan S. Microscale-calibrated modeling of the deformation response of dual-phase steels. (In preparation) 2013.

[44] Saylor DM, Fridy J, El-Dasher BS, Jung KY and Rollett AD. Statistically representative three-dimensional microstructures based on orthogonal observation

sections. Metallurgical and Materials Transactions a-Physical Metallurgy and Materials Science 2004;35A(7):1969-1979.

[45] Bassani JL and Racherla V. From non-planar dislocation cores to non-associated plasticity and strain bursts. Progress in Materials Science 2011;56(6).

[46] Racherla V (2007) Non-associated plastic flow and effects on macroscopic failure mechanisms. Phd Dissertation (University of Pennsylvania).

[47] Kim DH, Kim SJ, Kim SH, Rollett AD, Oh KH and Han HN. Microtexture development during equibiaxial tensile deformation in monolithic and dual phase steels. Acta Materialia 2011;59(14):5462-5471.

[48] Kadkhodapour J, Schmauder S, Raabe D, Ziaei-Rad S, Weber U and Calcagnotto M. Experimental and numerical study on geometrically necessary dislocations and non-homogeneous mechanical properties of the ferrite phase in dual phase steels. Acta Materialia 2011;59(11):4387-4394.

[49] Dillien S, Seefeldt M, Allain S, Bouaziz O and Van Houtte P. EBSD study of the substructure development with cold deformation of dual phase steel. Materials Science and Engineering a-Structural Materials Properties Microstructure and Processing 2010;527(4-5):947-953.

[50] Howard J (2001) *Mechanics of Motor Proteins and the Cytoskeleton* (Sinauer Associates, Inc., Sunderland, Massachusetts, USA).

[51] Fletcher DA and Mullins D. Cell mechanics and the cytoskeleton. Nature 2010;463(7280):485-492.

[52] Gardel ML, Nakamura F, Hartwig JH, Crocker JC, Stossel TP and Weitz DA. Prestressed F-actin networks cross-linked by hinged filamins replicate mechanical properties of cells. Proceedings of the National Academy of Sciences of the United States of America 2006;103(6):1762-1767.

[53] Mizuno D, Tardin C, Schmidt CF and MacKintosh FC. Nonequilibrium mechanics of active cytoskeletal networks. Science 2007;315(5810):370-373.

[54] Huisman EM, van Dillen T, Onck PR and Van der Giessen E. Three-dimensional cross-linked F-actin networks: Relation between network architecture and mechanical behavior. Physical Review Letters 2007;99(20).

[55] Onck PR, Koeman T, van Dillen T and van der Giessen E. Alternative explanation of stiffening in cross-linked semiflexible networks. Physical Review Letters 2005;95(17).

[56] Broedersz CP, Storm C and MacKintosh FC. Nonlinear elasticity of composite networks of stiff biopolymers with flexible linkers. Physical Review Letters 2008;101(11).

[57] Broedersz CP, Storm C and MacKintosh FC. Effective-medium approach for stiff polymer networks with flexible cross-links. Physical Review E 2009;79(6).

[58] Kasza KE, Koenderink GH, Lin YC, Broedersz CP, Messner W, Nakamura F, Stossel TP, MacKintosh FC and Weitz DA. Nonlinear elasticity of stiff biopolymers connected by flexible linkers. Physical Review E 2009;79(4).

[59] Koenderink GH, Dogic Z, Nakamura F, Bendix PM, MacKintosh FC, Hartwig JH, Stossel TP and Weitz DA. An active biopolymer network controlled by molecular motors. Proceedings of the National Academy of Sciences of the United States of America 2009;106(36):15192-15197.

[60] Lieleg O, Claessens M and Bausch AR. Structure and dynamics of cross-linked actin networks. Soft Matter 2010;6(2):218-225.
[61] Lin DC, Douglas JF and Horkay F. Development of minimal models of the elastic properties of flexible and stiff polymer networks with permanent and thermoreversible cross-links. Soft Matter 2010;6(15):3548-3561.
[62] WorldAutoSteel. The Advanced High-Strength Steel Applications Guidlines Version 4.1. 2009.
[63] Krauss G. Deformation and fracture in martensitic carbon steels tempered at low temperatures. Metallurgical and Materials Transactions a-Physical Metallurgy and Materials Science 2001;32(4):861-877.
[64] Krauss G and Matlock DK. Effects of strain hardening and fine structure on strength and toughness of tempered martensite in carbon steels. Journal De Physique Iv 1995;5(C8):51-60.
[65] Furuhara T, Morito S and Maki T. Morphology, substructure and crystallography of lath martensite in Fe-C alloys. Journal De Physique Iv 2003;112:255-258.
[66] Jang JI, Shim S, Komazaki S and Honda T. A nanoindentation study on grain-boundary contributions to strengthening and aging degradation mechanisms in advanced 12 Cr ferritic steel. Journal of Materials Research 2007;22(1):175-185.
[67] Zhang CY, Wang QF, Ren JX, Li RX, Wang MZ, Zhang FC and Sun KM. Effect of martensitic morphology on mechanical properties of an as-quenched and tempered 25CrMo48V steel. Materials Science and Engineering a-Structural Materials Properties Microstructure and Processing 2012;534:339-346.
[68] Moon J, Kim SJ and Lee C. Effect of thermo-mechanical cycling on the microstructure and strength of lath martensite in the weld CGHAZ of HSLA steel. Materials Science and Engineering a-Structural Materials Properties Microstructure and Processing 2011;528(25-26):7658-7662.
[69] Yu XH, Caron JL, Babu SS, Lippold JC, Isheim D and Seidman DN. Characterization of microstructural strengthening in the heat-affected zone of a blast-resistant naval steel. Acta Materialia 2010;58(17):5596-5609.
[70] Shibata A, Nagoshi T, Sone M, Morito S and Higo Y. Evaluation of the block boundary and sub-block boundary strengths of ferrous lath martensite using a micro-bending test. Materials Science and Engineering a-Structural Materials Properties Microstructure and Processing 2010;527(29-30):7538-7544.
[71] Ohmura T, Tsuzaki K and Matsuoka S. Nanohardness measurement of high-purity Fe-C martensite. Scripta Materialia 2001;45(8):889-894.
[72] Ohmura T, Tsuzaki K and Matsuoka S. Evaluation of the matrix strength of Fe-0.4 wt% C tempered martensite using nanoindentation techniques. Philosophical Magazine a-Physics of Condensed Matter Structure Defects and Mechanical Properties 2002;82(10):1903-1910.
[73] Ohmura T, Hara T and Tsuzaki K. Relationship between nanohardness and microstructures in high-purity Fe-C as-quenched and quench-tempered martensite. Journal of Materials Research 2003;18(6):1465-1470.
[74] Ohmura T, Minor AM, Stach EA and Morris JW. Dislocation-grain boundary interactions in martensitic steel observed through in situ nanoindentation in a transmission electron microscope. Journal of Materials Research 2004;19(12):3626-3632.

[75] Hirth JP and Cohen M. ON STRENGTH-DIFFERENTIAL PHENOMENON IN HARDENED STEEL. Metallurgical Transactions 1970;1(1):3-&.
[76] Rauch GC and Leslie WC. EXTENT AND NATURE OF STRENGTH-DIFFERENTIAL EFFECT IN STEELS. Metallurgical Transactions 1972;3(2):373-&.
[77] Rauch GC, Daga RL, Radcliffe SV, Sober RJ and Leslie WC. VOLUME EXPANSION, PRESSURE EFFECTS, AND STRENGTH DIFFERENTIAL IN AS-QUENCHED IRON-CARBON MARTENSITE. Metallurgical Transactions a-Physical Metallurgy and Materials Science 1975;6(12):2279-2287.
[78] Chait R. FACTORS INFLUENCING STRENGTH DIFFERENTIAL OF HIGH-STRENGTH STEELS. Metallurgical Transactions 1972;3(2):365-&.
[79] Spitzig WA, Sober RJ and Richmond O. PRESSURE-DEPENDENCE OF YIELDING AND ASSOCIATED VOLUME EXPANSION IN TEMPERED MARTENSITE. Acta Metallurgica 1975;23(7):885-893.
[80] Spitzig WA, Sober RJ and Richmond O. EFFECT OF HYDROSTATIC-PRESSURE ON DEFORMATION-BEHAVIOR OF MARAGING AND HY-80 STEELS AND ITS IMPLICATIONS FOR PLASTICITY THEORY. Metallurgical Transactions a-Physical Metallurgy and Materials Science 1976;7(11):1703-1710.
[81] Spitzig WA and Richmond O. THE EFFECT OF PRESSURE ON THE FLOW-STRESS OF METALS. Acta Metallurgica 1984;32(3):457-463.
[82] Balliger NK and Gladman T. WORK-HARDENING OF DUAL-PHASE STEELS. Metal Science 1981;15(3):95-108.
[83] Davies RG. INFLUENCE OF MARTENSITE COMPOSITION AND CONTENT ON PROPERTIES OF DUAL PHASE STEELS. Metallurgical Transactions a-Physical Metallurgy and Materials Science 1978;9(5):671-679.
[84] Marder AR. DEFORMATION CHARACTERISTICS OF DUAL-PHASE STEELS. Metallurgical Transactions a-Physical Metallurgy and Materials Science 1982;13(1):85-92.
[85] Su YL and Gurland J. STRAIN PARTITION, UNIFORM ELONGATION AND FRACTURE STRAIN IN DUAL-PHASE STEELS. Materials Science and Engineering 1987;95:151-165.
[86] Rashid MS and Cprek ER (1978) Relationship between microstructure and formability in two high-strength low-alloy steels. in *Formability topics - metallic materials*, eds Niemeier BA, Schmieder AK, & Newby JR (American Society for Testing and Materials, Philadelphia, PA), pp 174-190.
[87] Kunz A, Pathak S and Greer JR. Size effects in Al nanopillars: Single crystalline vs. bicrystalline. Acta Materialia 2011;59(11):4416-4424.
[88] Ng KS and Ngan AHW. Deformation of micron-sized aluminium bi-crystal pillars. Philosophical Magazine 2009;89(33):3013-3026.
[89] Lee G, Kim JY, Budiman AS, Tamura N, Kunz M, Chen K, Burek MJ, Greer JR and Tsui TY. Fabrication, structure and mechanical properties of indium nanopillars. Acta Materialia 2010;58(4):1361-1368.
[90] Uchic MD, Shade PA and Dimiduk DM. Plasticity of Micrometer-Scale Single Crystals in Compression. Annual Review of Materials Research 2009;39:361-386.

[91] Uchic MD, Dimiduk DM, Florando JN and Nix WD. Sample dimensions influence strength and crystal plasticity. Science 2004;305(5686):986-989.
[92] Nix WD, Greer JR, Feng G and Lilleodden ET. Deformation at the nanometer and micrometer length scales: Effects of strain gradients and dislocation starvation. Thin Solid Films 2007;515(6):3152-3157.
[93] Greer JR and Nix WD. Nanoscale gold pillars strengthened through dislocation starvation. Physical Review B 2006;73(24).
[94] Greer JR and De Hosson JTM. Plasticity in small-sized metallic systems: Intrinsic versus extrinsic size effect. Progress in Materials Science 2011;56(6):654-724.
[95] Greer JR, Oliver WC and Nix WD. Size dependence of mechanical properties of gold at the micron scale in the absence of strain gradients. Acta Materialia 2005;53(6):1821-1830.
[96] Hatem TM and Zikry MA. Dislocation density crystalline plasticity modeling of lath martensitic microstructures in steel alloys. Philosophical Magazine 2009;89(33):3087-3109.
[97] Lee DT. 2-DIMENSIONAL VORONOI DIAGRAMS IN THE LP-METRIC. Journal of the Acm 1980;27(4):604-618.
[98] Kitahara H, Ueji R, Tsuji N and Minamino Y. Crystallographic features of lath martensite in low-carbon steel. Acta Materialia 2006;54(5):1279-1288.
[99] McVeigh C, Vernerey F, Liu WK, Moran B and Olson G. An interactive micro-void shear localization mechanism in high strength steels. Journal of the Mechanics and Physics of Solids 2007;55(2):225-244.
[100] Grujicic M and Dang P. COMPUTER-SIMULATION OF MARTENSITIC-TRANSFORMATION IN FE-NI FACE-CENTERED-CUBIC ALLOYS. Materials Science and Engineering a-Structural Materials Properties Microstructure and Processing 1995;201(1-2):194-204.
[101] Suzuki T, Shimono M, Ren X, Otsuka K and Onodera H. Study of martensitic transformation by use of Monte-Carlo method and molecular dynamics. Materials Science and Engineering a-Structural Materials Properties Microstructure and Processing 2006;438:95-98.
[102] Marian J, Wirth BD, Schaublin R, Odette GR and Perlado JM. MD modeling of defects in Fe and their interactions. Journal of Nuclear Materials 2003;323(2-3):181-191.
[103] Lee MG, Lim H, Adams BL, Hirth JP and Wagoner RH. A dislocation density-based single crystal constitutive equation. International Journal of Plasticity 2010;26(7):925-938.
[104] Schastlivtsev VM, Rodionov DP, Khlebnikova YV and Yakovleva IL. Peculiarity of structure and crystallography of plastic deformation of lath martensite in structural steels. Materials Science and Engineering a-Structural Materials Properties Microstructure and Processing 1999;273:437-442.
[105] Peirce D, Shih CF and Needleman A. A TANGENT MODULUS METHOD FOR RATE DEPENDENT SOLIDS. Computers & Structures 1984;18(5):875-887.
[106] J.W. K. User Material Subroutine for Single Crystal Plasticity. http://www.columbia.edu/~jk2079/Kysar_Research_Laboratory/Single_Crystal_UMAT.html 1997.

[107] Lagarias JC, Reeds JA, Wright MH and Wright PE. Convergence properties of the Nelder-Mead simplex method in low dimensions. Siam Journal on Optimization 1998;9(1):112-147.
[108] Morito S, Nishikawa J and Maki T. Dislocation density within lath martensite in Fe-C and Fe-Ni alloys. Isij International 2003;43(9):1475-1477.
[109] Leslie WC (1981) *The Physical Metallurgy of Steels* (Hemisphere Publishing Corporation).
[110] Groeger R, Racherla V, Bassani JL and Vitek V. Multiscale modeling of plastic deformation of molybdenum and tungsten: II. Yield criterion for single crystals based on atomistic studies of glide of 1/2 < 111 > screw dislocations. Acta Materialia 2008;56(19).
[111] Koester A, Ma AX and Hartmaier A. Atomistically informed crystal plasticity model for body-centered cubic iron. Acta Materialia 2012;60(9):3894-3901.
[112] Weinberger CR, Battaile CC, Buchheit TE and Holm EA. Incorporating atomistic data of lattice friction into BCC crystal plasticity models. International Journal of Plasticity 2012;37:16-30.
[113] Caillard D. An in situ study of hardening and softening of iron by carbon interstitials. Acta Materialia 2011;59(12):4974-4989.
[114] Caillard D. Kinetics of dislocations in pure Fe. Part I. In situ straining experiments at room temperature. Acta Materialia 2010;58(9).
[115] Caillard D. Kinetics of dislocations in pure Fe. Part II. In situ straining experiments at low temperature. Acta Materialia 2010;58(9).
[116] Gustafsson B, Kreiss H and J. O (1996) *Time Dependent Problems and Difference Methods* (Wiley-Interscience) First Edition Ed.
[117] Hosford WF (1993) *The mechanics of crystals and textured polycrystals* (Oxford University Press, Inc., New York).
[118] Asaro RJ and Needleman A. OVERVIEW .42. TEXTURE DEVELOPMENT AND STRAIN-HARDENING IN RATE DEPENDENT POLYCRYSTALS. Acta Metallurgica 1985;33(6):923-953.
[119] Wilhelm J and Frey E. Elasticity of stiff polymer networks. Physical Review Letters 2003;91(10).
[120] Marko JF and Siggia ED. BENDING AND TWISTING ELASTICITY OF DNA. Macromolecules 1994;27(4):981-988.
[121] Kaya M and Higuchi H. Nonlinear Elasticity and an 8-nm Working Stroke of Single Myosin Molecules in Myofilaments. Science 2010;329(5992):686-689.
[122] Svitkina TM, Verkhovsky AB and Borisy GG. Improved procedures for electron microscopic visualization of the cytoskeleton of cultured cells. Journal of Structural Biology 1995;115(3):290-303.
[123] Quey R (2012) Neper: a 3D random polycrystal generator for the finite element method (version 1.10).
[124] Quey R, Dawson PR and Barbe F. Large-scale 3D random polycrystals for the finite element method: Generation, meshing and remeshing. Computer Methods in Applied Mechanics and Engineering 2011;200(17-20):1729-1745.
[125] Lieleg O, Claessens M, Luan Y and Bausch AR. Transient binding and dissipation in cross-linked actin networks. Physical Review Letters 2008;101(10).

[126] Lieleg O, Kayser J, Brambilla G, Cipelletti L and Bausch AR. Slow dynamics and internal stress relaxation in bundled cytoskeletal networks. Nature Materials 2011;10(3):236-242.
[127] Lieleg O, Schmoller KM, Claessens M and Bausch AR. Cytoskeletal Polymer Networks: Viscoelastic Properties are Determined by the Microscopic Interaction Potential of Cross-links. Biophysical Journal 2009;96(11):4725-4732.
[128] Schmoller KM, Lieleg O and Bausch AR. Structural and Viscoelastic Properties of Actin/Filamin Networks: Cross-Linked versus Bundled Networks. Biophysical Journal 2009;97(1):83-89.

Appendix A

```
C-----------------------------------------------------------------------
      SUBROUTINE GSLPINIT_MART (GSLIP0, NSLIP, NSLPTL, NSET, PROP, SLPNOR, SLPDIR)

C-----  This subroutine calculates the initial value of current
C     strength for each slip system in a rate-dependent single crystal.
C     One set of initial values, proposed by Lee

C-----  These initial values may be different for all slip systems
C-----  Use single precision on cray
C
      IMPLICIT REAL*8 (A-H,O-Z)
      DIMENSION GSLIP0(NSLPTL), NSLIP(NSET), PROP(16,NSET),
     2          SLPNOR(3, NSLPTL), SLPDIR(3, NSLPTL),
     3          SLPLINE(3, NSLPTL)

C-----  Variables:
C
C     GSLIP0 -- initial value of current strength (OUTPUT)
C
C     NSLIP  -- number of slip systems in each set (INPUT)
C     NSLPTL -- total number of slip systems in all the sets (INPUT)
C     NSET   -- number of sets of slip systems (INPUT)
C     SLPNOR -- normal of slip plane (INPUT)
C     SLPDIR -- slip direction (INPUT)
C     SLPLINE-- edge dislocation line direction
C
C     PROP   -- material constants characterizing the initial value of
C               current strength (INPUT)
C
C               For Lee's law
C               PROP(1,i) -- shear modulus G in the ith set of
C                            slip systems
C               PROP(2,i) -- magnitude of burgers verctor b
C                            in the ith set of slip systems
C               PROP(3,i) -- ka
C               PROP(4,i) -- kb
C               PROP(5,i) -- initial dislocation density \rho_0
C               PROP(6,i) -- static yield stress
C
C

C     include all active slip systems, including different slip system sets

C     calculate the edge dislocation line direction for each slip system
      call VectorCrossProduct(NSLPTL, SLPNOR, SLPDIR, SLPLINE)
      id = 0
      do i=1, NSET
        Gshear = PROP(1,i)
        burg = PROP(2,i)
```

```
      sigma0 = PROP(6,i)

      do j=1, NSLIP(i)
        id = id + 1

        jd = 0
        Term0 = 0.d0
        do ii=1, NSET
          rho0 = PROP(5, ii)
          do jj=1, NSLIP(ii)
            jd = jd + 1

            Hij = 0.d0
            do k=1, 3
              Hij = Hij + SLPNOR(k, id)*SLPLINE(k, jd)
            end do
            IF (Hij .GT. 1.d0 .and. Hij .LT. 1.1) THEN
              Hij = 1.d0
            else if (Hij .GT. 1.1) then
              WRITE (6,*)'***CPENG ERROR: Hij is bigger than 1.0'
              write (6,*)'SLPNOR are', (SLPNOR(kk,id),kk=1,3)
              write (6,*)'SLPLINE are', (SLPLINE(kk,jd),kk=1,3)
              write (6,*)'Hij is', Hij
              STOP
            END IF
            Term0 = Term0 + ABS(Hij)*rho0
          end do
        end do
        GSLIP0(id) = sigma0 + Gshear*burg*SQRT(Term0)
      end do
    end do

    RETURN
    END
C-----------------------------------------------------------------------
    SUBROUTINE DislocationHarden(rho, NSLIP, NSLPTL, NSET,
    2                        H, PROP, ND, SLPNOR, SLPDIR)

C     NSLIP  -- number of slip systems in each set (INPUT)
C     NSLPTL -- total number of slip systems in all the sets (INPUT)
C     NSET   -- number of sets of slip systems (INPUT)
C
C     H      -- current value of self- and latent-hardening moduli
C               (OUTPUT)
C               H(i,i) -- self-hardening modulus of the ith slip system
C                         (no sum over i)
C               H(i,j) -- latent-hardening molulus of the ith slip
C                         system due to a slip in the jth slip system
C                         (i not equal j)
C
C     PROP   -- material constants characterizing the self- and latent-
C               hardening law (INPUT)
C
C               For Lee's hardening law
C               PROP(1,i) -- shear modulus G in the ith set of
C                            slip systems
```

```
C             PROP(2,i) -- magnitude of burgers verctor b
C                     in the ith set of slip systems
C             PROP(3,i) -- k_a
C             PROP(4,i) -- k_b
C             PROP(5,i) -- initial dislocation density
C                     rho_0 in the ith set of slip systems
C
C     ND     -- leading dimension of arrays defined in subroutine UMAT
C             (INPUT)

C-----  Use single precision on cray
C
      IMPLICIT REAL*8 (A-H,O-Z)

      DIMENSION rho(NSLPTL), NSLIP(NSET),
     2         PROP(16,NSET), H(ND,NSLPTL),
     3         SLPNOR(3,NSLPTL), SLPDIR(3,NSLPTL), SLPLINE(3,NSLPTL)


C     calculate the edge dislocation line direction for each slip system
      call VectorCrossProduct(NSLPTL, SLPNOR, SLPDIR, SLPLINE)

      ISELF=0
      DO I=1,NSET
        DO J=1,NSLIP(I)
          ISELF=ISELF+1

          Gshear = PROP(1, I)
          ak = PROP(3, I)
          bk = PROP(4, I)

          DO LATENT=1,NSLPTL
            Hij = 0.d0
            do k=1, 3
              Hij = Hij + SLPNOR(k, ISELF)*SLPLINE(k, LATENT)
            end do
            Hij = ABS(Hij)
            IF (Hij .GT. 1.d0 .and. Hij .LT. 1.1) THEN
              Hij = 1.d0
            else if (Hij .GT. 1.1) then
              WRITE (6,*)'***CPENG ERROR: Hij is bigger than 1.0'
              write (6,*)'SLPNOR are', (SLPNOR(kk,ISELF),kk=1,3)
              write (6,*)'SLPLINE are', (SLPLINE(kk,LATENT),kk=1,3)
              write (6,*)'Hij is', Hij
              STOP
            END IF

            rhoSum = 0.d0
            hRhoSum = 0.d0
            do k=1, NSLPTL
              Hik = 0.d0
              do ii=1, 3
                Hik = Hik + SLPNOR(ii, ISELF)*SLPLINE(ii, k)
              end do
              Hik = ABS(Hik)
              IF (Hik .GT. 1.d0 .and. Hik .LT. 1.1d0) THEN
```

```
              Hik = 1.d0
            else if (Hik .GT. 1.1) then
              WRITE (6,*)'***CPENG ERROR: Hik is bigger than 1.0'
              write (6,*)'SLPNOR are', (SLPNOR(kk,ISELF),kk=1,3)
              write (6,*)'SLPLINE are', (SLPLINE(kk,k),kk=1,3)
              write (6,*)'Hik is', Hik
              STOP
            END IF

            rhoSum = rhoSum + rho(k)
            hRhoSum = hRhoSum + Hik*rho(k)
          end do
          if (hRhoSum .lt. 0.0) then
            write(6,*)'***CPENG ERROR: hRhoSum is less than 0.0'
            write(6,*)'hRhoSum is', hRhoSum
            stop
          end if

          H(LATENT, ISELF) = 0.5d0*Gshear*Hij*(SQRT(rhoSum)/ak -
     2                    bk*rho(LATENT))/SQRT(hRhoSum)
        END DO

      END DO
    END DO

    RETURN
    END

C-----------------------------------------------------------------------
    Subroutine DislocationEvol(rho,
    2                NSLIP, NSLPTL, NSET, DGAMMA, DRho,
    3                PROP, ND)
C
C    Dislocaiton density evolution equation
C    Output the increment of dislocaiton densities
C
    IMPLICIT REAL*8 (A-H,O-Z)

    DIMENSION rho(NSLPTL), NSLIP(NSET),
    2        PROP(16,NSET), DGAMMA(NSLPTL), DRho(NSLPTL)

    id=0
    DO i=1,NSET
      DO j=1,NSLIP(I)
        id=id+1

        burg = PROP(2, i)
        burgInv = 1.d0/burg
        ak = PROP(3, i)
        bk = PROP(4, i)

        rhoSum = 0.d0
        do k=1, NSLPTL
          rhoSum = rhoSum + rho(k)
        end do
        if (rhoSum .le. PROP(5,1)) then
```

```
            write(6,*)'***CPENG ERROR: rhoSum is less than rho_0'
            write(6,*)'rhoSum is', rhoSum
            stop
          end if

          DRho(id) = burgInv*(rhoSum/ak - bk*rho(id))*ABS(DGAMMA(id))
        END DO
      END DO

      RETURN
      END
C-----------------------------------------------------------------------
```

Appendix B

```
      SUBROUTINE NonSchmidInit (SLPDIR, SLPNOR, SLPNOR1, SLPCRS1,
     2                  SLPCRS2, ROTATE, NSLPTL, NSLIP, NSET)

C-----  Use single precision on cray
C
      IMPLICIT REAL*8 (A-H,O-Z)
      DIMENSION SLPDIR(3,24), SLPNOR(3,24), SLPNOR1(3,24),
     *        SLPCRS1(3,24), SLPCRS2(3,24),NSLIP(NSET),
     *        ROTATE(3,3), TERM(3)

      SLPDIR(1,1) = 1.;   SLPDIR(2,1) = 1.;   SLPDIR(3,1) = 1.
      SLPNOR(1,1) = 0.;   SLPNOR(2,1) = 1.;   SLPNOR(3,1) =-1.
      SLPNOR1(1,1)=-1.;   SLPNOR1(2,1)= 1.;   SLPNOR1(3,1)= 0.

      SLPDIR(1,2) = 1.;   SLPDIR(2,2) = 1.;   SLPDIR(3,2) = 1.
      SLPNOR(1,2) =-1.;   SLPNOR(2,2) = 0.;   SLPNOR(3,2) = 1.
      SLPNOR1(1,2)= 0.;   SLPNOR1(2,2)=-1.;   SLPNOR1(3,2)= 1.

      SLPDIR(1,3) = 1.;   SLPDIR(2,3) = 1.;   SLPDIR(3,3) = 1.
      SLPNOR(1,3) = 1.;   SLPNOR(2,3) =-1.;   SLPNOR(3,3) = 0.
      SLPNOR1(1,3)= 1.;   SLPNOR1(2,3)= 0.;   SLPNOR1(3,3)=-1.

      SLPDIR(1,4) =-1.;   SLPDIR(2,4) = 1.;   SLPDIR(3,4) = 1.
      SLPNOR(1,4) =-1.;   SLPNOR(2,4) = 0.;   SLPNOR(3,4) =-1.
      SLPNOR1(1,4)=-1.;   SLPNOR1(2,4)=-1.;   SLPNOR1(3,4)= 0.

      SLPDIR(1,5) =-1.;   SLPDIR(2,5) = 1.;   SLPDIR(3,5) = 1.
      SLPNOR(1,5) = 0.;   SLPNOR(2,5) =-1.;   SLPNOR(3,5) = 1.
      SLPNOR1(1,5)= 1.;   SLPNOR1(2,5)= 0.;   SLPNOR1(3,5)= 1.

      SLPDIR(1,6) =-1.;   SLPDIR(2,6) = 1.;   SLPDIR(3,6) = 1.
      SLPNOR(1,6) = 1.;   SLPNOR(2,6) = 1.;   SLPNOR(3,6) = 0.
      SLPNOR1(1,6)= 0.;   SLPNOR1(2,6)= 1.;   SLPNOR1(3,6)=-1.

      SLPDIR(1,7) =-1.;   SLPDIR(2,7) =-1.;   SLPDIR(3,7) = 1.
      SLPNOR(1,7) = 0.;   SLPNOR(2,7) =-1.;   SLPNOR(3,7) =-1.
      SLPNOR1(1,7)= 1.;   SLPNOR1(2,7)=-1.;   SLPNOR1(3,7)= 0.

      SLPDIR(1,8) =-1.;   SLPDIR(2,8) =-1.;   SLPDIR(3,8) = 1.
      SLPNOR(1,8) = 1.;   SLPNOR(2,8) = 0.;   SLPNOR(3,8) = 1.
      SLPNOR1(1,8)= 0.;   SLPNOR1(2,8)= 1.;   SLPNOR1(3,8)= 1.

      SLPDIR(1,9) =-1.;   SLPDIR(2,9) =-1.;   SLPDIR(3,9) = 1.
      SLPNOR(1,9) =-1.;   SLPNOR(2,9) = 1.;   SLPNOR(3,9) = 0.
      SLPNOR1(1,9)=-1.;   SLPNOR1(2,9)= 0.;   SLPNOR1(3,9)=-1.

      SLPDIR(1,10) = 1.;   SLPDIR(2,10) =-1.;   SLPDIR(3,10) = 1.
      SLPNOR(1,10) = 1.;   SLPNOR(2,10) = 0.;   SLPNOR(3,10) =-1.
      SLPNOR1(1,10)= 1.;   SLPNOR1(2,10)= 1.;   SLPNOR1(3,10)= 0.
```

SLPDIR(1,11) = 1.; SLPDIR(2,11) =-1.; SLPDIR(3,11) = 1.
SLPNOR(1,11) = 0.; SLPNOR(2,11) = 1.; SLPNOR(3,11) = 1.
SLPNOR1(1,11)=-1.; SLPNOR1(2,11)= 0.; SLPNOR1(3,11)= 1.

SLPDIR(1,12) = 1.; SLPDIR(2,12) =-1.; SLPDIR(3,12) = 1.
SLPNOR(1,12) =-1.; SLPNOR(2,12) =-1.; SLPNOR(3,12) = 0.
SLPNOR1(1,12)= 0.; SLPNOR1(2,12)=-1.; SLPNOR1(3,12)=-1.

SLPDIR(1,13) =-1.; SLPDIR(2,13) =-1.; SLPDIR(3,13) =-1.
SLPNOR(1,13) = 0.; SLPNOR(2,13) = 1.; SLPNOR(3,13) =-1.
SLPNOR1(1,13)= 1.; SLPNOR1(2,13)= 0.; SLPNOR1(3,13)=-1.

SLPDIR(1,14) =-1.; SLPDIR(2,14) =-1.; SLPDIR(3,14) =-1.
SLPNOR(1,14) =-1.; SLPNOR(2,14) = 0.; SLPNOR(3,14) = 1.
SLPNOR1(1,14)=-1.; SLPNOR1(2,14)= 1.; SLPNOR1(3,14)= 0.

SLPDIR(1,15) =-1.; SLPDIR(2,15) =-1.; SLPDIR(3,15) =-1.
SLPNOR(1,15) = 1.; SLPNOR(2,15) =-1.; SLPNOR(3,15) = 0.
SLPNOR1(1,15)= 0.; SLPNOR1(2,15)=-1.; SLPNOR1(3,15)= 1.

SLPDIR(1,16) = 1.; SLPDIR(2,16) =-1.; SLPDIR(3,16) =-1.
SLPNOR(1,16) =-1.; SLPNOR(2,16) = 0.; SLPNOR(3,16) =-1.
SLPNOR1(1,16)= 0.; SLPNOR1(2,16)= 1.; SLPNOR1(3,16)=-1.

SLPDIR(1,17) = 1.; SLPDIR(2,17) =-1.; SLPDIR(3,17) =-1.
SLPNOR(1,17) = 0.; SLPNOR(2,17) =-1.; SLPNOR(3,17) = 1.
SLPNOR1(1,17)=-1.; SLPNOR1(2,17)=-1.; SLPNOR1(3,17)= 0.

SLPDIR(1,18) = 1.; SLPDIR(2,18) =-1.; SLPDIR(3,18) =-1.
SLPNOR(1,18) = 1.; SLPNOR(2,18) = 1.; SLPNOR(3,18) = 0.
SLPNOR1(1,18)= 1.; SLPNOR1(2,18)= 0.; SLPNOR1(3,18)= 1.

SLPDIR(1,19) = 1.; SLPDIR(2,19) = 1.; SLPDIR(3,19) =-1.
SLPNOR(1,19) = 0.; SLPNOR(2,19) =-1.; SLPNOR(3,19) =-1.
SLPNOR1(1,19)=-1.; SLPNOR1(2,19)= 0.; SLPNOR1(3,19)=-1.

SLPDIR(1,20) = 1.; SLPDIR(2,20) = 1.; SLPDIR(3,20) =-1.
SLPNOR(1,20) = 1.; SLPNOR(2,20) = 0.; SLPNOR(3,20) = 1.
SLPNOR1(1,20)= 1.; SLPNOR1(2,20)=-1.; SLPNOR1(3,20)= 0.

SLPDIR(1,21) = 1.; SLPDIR(2,21) = 1.; SLPDIR(3,21) =-1.
SLPNOR(1,21) =-1.; SLPNOR(2,21) = 1.; SLPNOR(3,21) = 0.
SLPNOR1(1,21)= 0.; SLPNOR1(2,21)= 1.; SLPNOR1(3,21)= 1.

SLPDIR(1,22) =-1.; SLPDIR(2,22) = 1.; SLPDIR(3,22) =-1.
SLPNOR(1,22) = 1.; SLPNOR(2,22) = 0.; SLPNOR(3,22) =-1.
SLPNOR1(1,22)= 0.; SLPNOR1(2,22)=-1.; SLPNOR1(3,22)=-1.

SLPDIR(1,23) =-1.; SLPDIR(2,23) = 1.; SLPDIR(3,23) =-1.
SLPNOR(1,23) = 0.; SLPNOR(2,23) = 1.; SLPNOR(3,23) = 1.
SLPNOR1(1,23)= 1.; SLPNOR1(2,23)= 1.; SLPNOR1(3,23)= 0.

SLPDIR(1,24) =-1.; SLPDIR(2,24) = 1.; SLPDIR(3,24) =-1.
SLPNOR(1,24) =-1.; SLPNOR(2,24) =-1.; SLPNOR(3,24) = 0.
SLPNOR1(1,24)=-1.; SLPNOR1(2,24)= 0.; SLPNOR1(3,24)= 1.

```
      NSLPTL = 24
      NSLIP(1) = 24

C     WRITE(6,*) '          '
C     WRITE(6,*) ' #     Slip Direction     Slip Plane     Slip Plane2'
C     DO J=1,NSLIP(1)
C       WRITE (6,11) J,
C    2            (INT(SLPDIR(K,J)),K=1,3), (INT(SLPNOR(K,J)),K=1,3),
C    3            (INT(SLPNOR1(K,J)),K=1,3)
C     END DO
C11   FORMAT(1X,I2,5X,'[',3(1X,I2),1X,']',5X,'(',3(1X,I2),1X,')',
C    2      5X,'(',3(1X,I2),1X,')')
C-----calculate the the second and third unit vectors
C    SLPCRS1 and SLPCRS2
C-----SLPCRS1
      call VectorCrossProduct(NSLIP(1), SLPNOR, SLPDIR, SLPCRS1)
C-----SLPCRS2
      call VectorCrossProduct(NSLIP(1), SLPNOR1, SLPDIR, SLPCRS2)

C     WRITE(6,*) '          '
C     WRITE(6,*) ' #          Slip Cross1          Slip Cross2'
C     DO J=1,NSLIP(1)
C       WRITE (6,12) J,
C    2            (SLPCRS1(K,J),K=1,3), (SLPCRS2(K,J),K=1,3)
C     END DO
C12   FORMAT(1X,I2,3X,'(',3(1X,F5.2),1X,')',3X,'(',3(1X,F5.2),1X,')')

C----- Normalize the vectors
      DO I=1, NSLIP(1)
        TERM1 = 0.
        TERM2 = 0.
        TERM3 = 0.
        TERM4 = 0.
        TERM5 = 0.
        DO J=1, 3
          TERM1 = TERM1 + SLPDIR(J,I)**2
          TERM2 = TERM2 + SLPNOR(J,I)**2
          TERM3 = TERM3 + SLPNOR1(J,I)**2
          TERM4 = TERM4 + SLPCRS1(J,I)**2
          TERM5 = TERM5 + SLPCRS2(J,I)**2
        END DO

        TERM1SqrtInv = 1./SQRT(TERM1)
        TERM2SqrtInv = 1./SQRT(TERM2)
        TERM3SqrtInv = 1./SQRT(TERM3)
        TERM4SqrtInv = 1./SQRT(TERM4)
        TERM5SqrtInv = 1./SQRT(TERM5)

        DO J=1, 3
          SLPDIR(J,I) = SLPDIR(J,I)*TERM1SqrtInv
          SLPNOR(J,I) = SLPNOR(J,I)*TERM2SqrtInv
          SLPNOR1(J,I) = SLPNOR1(J,I)*TERM3SqrtInv
          SLPCRS1(J,I) = SLPCRS1(J,I)*TERM4SqrtInv
          SLPCRS2(J,I) = SLPCRS2(J,I)*TERM5SqrtInv
        END DO
      END DO
```

```
C-----Unit vectors in slip directions: SLPDIR, and unit normals to
C     slip planes: SLPNOR, and unit normals: SLPNOR1, and
C     unit cross-product: SLPCRS1, and unit cross-product: SLPCRS2
C     in global system
C
            DO J=1,NSLIP(1)
              DO I=1,3
                      TERM(I)=0.
                      DO K=1,3
                              TERM(I)=TERM(I)+ROTATE(I,K)*SLPDIR(K,J)
                      END DO
                    END DO
                    Term0 = 0.
                    do i=1, 3
                      Term0 = Term0 + TERM(i)**2
                    end do
                    Term0SqrtInv = 1./SQRT(Term0)
                    DO I=1,3
                      SLPDIR(I,J)=TERM(I)*Term0SqrtInv
                    END DO

                    DO I=1,3
                      TERM(I)=0.
                      DO K=1,3
                              TERM(I)=TERM(I)+ROTATE(I,K)*SLPNOR(K,J)
                      END DO
                    END DO
                    Term0 = 0.
                    do i=1, 3
                      Term0 = Term0 + TERM(i)**2
                    end do
                    Term0SqrtInv = 1./SQRT(Term0)
                    DO I=1,3
                      SLPNOR(I,J)=TERM(I)*Term0SqrtInv
                    END DO

                    DO I=1,3
                      TERM(I)=0.
                      DO K=1,3
                              TERM(I)=TERM(I)+ROTATE(I,K)*SLPNOR1(K,J)
                      END DO
                    END DO
                    Term0 = 0.
                    do i=1, 3
                      Term0 = Term0 + TERM(i)**2
                    end do
                    Term0SqrtInv = 1./SQRT(Term0)
                    DO I=1,3
                      SLPNOR1(I,J)=TERM(I)*Term0SqrtInv
                    END DO

                    DO I=1,3
                      TERM(I)=0.
                      DO K=1,3
                              TERM(I)=TERM(I)+ROTATE(I,K)*SLPCRS1(K,J)
```

```
                    END DO
                  END DO
                  Term0 = 0.
                  do i=1, 3
                    Term0 = Term0 + TERM(i)**2
                  end do
                  Term0SqrtInv = 1./SQRT(Term0)
                  DO I=1,3
                    SLPCRS1(I,J)=TERM(I)*Term0SqrtInv
                  END DO

                  DO I=1,3
                    TERM(I)=0.
                    DO K=1,3
                          TERM(I)=TERM(I)+ROTATE(I,K)*SLPCRS2(K,J)
                    END DO
                  END DO
                  Term0 = 0.
                  do i=1, 3
                    Term0 = Term0 + TERM(i)**2
                  end do
                  Term0SqrtInv = 1./SQRT(Term0)
                  DO I=1,3
                    SLPCRS2(I,J)=TERM(I)*Term0SqrtInv
                  END DO
            END DO

    RETURN
    END
C-----------------------------------------------------------------------
C-----------------------------------------------------------------------
    SUBROUTINE VectorCrossProduct (N, A, B, CRS)

C-----  Cross Product of Two Unit Vectors CRS = A X B

C-----  Use single precision on cray
C
    IMPLICIT REAL*8 (A-H,O-Z)
    DIMENSION A(3,N), B(3,N), CRS(3,N)


    DO I=1, N
      CRS(1,I) = A(2,I)*B(3,I) - A(3,I)*B(2,I)
      CRS(2,I) = A(3,I)*B(1,I) - A(1,I)*B(3,I)
      CRS(3,I) = A(1,I)*B(2,I) - A(2,I)*B(1,I)

      TERM = SQRT(CRS(1,I)**2 + CRS(2,I)**2 + CRS(3,I)**2)
      CRS(1,I) = CRS(1,I)/TERM
      CRS(2,I) = CRS(2,I)/TERM
      CRS(3,I) = CRS(3,I)/TERM
    END DO

    RETURN
    END
C-----------------------------------------------------------------------
```